21st Annual

Alberta Biomedical Engineering Conference

Program and Proceedings

October 23, 2020

21st Annual Alberta Biomedical Engineering Conference

October 23, 2020

PROGRAM COMMITTEE

CONFERENCE ORGANIZERS		
Co-Chairs	University of Calgary	Roman Krawetz Michael S. Kallos
	University of Alberta	Dan Romanyk
Student Co-Chairs	University of Calgary	Tiffany Dang Thomas Lijnse

ABSTRACT REVIEWERS

University of Calgary	University of Saskatchewan	University of Alberta
Steven Boyd	James Johnston	Hossein Rouhani
Elizabeth Condliffe		Lindsey Westover
Brent Edwards		
Reed Ferber		
Michael Kallos		
Roman Krawetz		
Sarah Manske		

KEYNOTE SPEAKER	
Ian Buchanan	**Vice President Technical Services, Exergy Solutions**

INDUSTRY SPEAKERS	
Sam Wadsworth	**Chief Scientific Officer, Aspect Biosystems**
Estee Lee	**Core MR Development, Circle Cardiovascular Imaging Inc.**

STUDENT TRAINEES		
University of Calgary	Tiffany Dang Thomas Lijnse	BMEG VP Conference Student Leaders
	Brett Abraham James Colter Tiffany Dang Alanna Devolin Thomas Lijnse Conrad Mielczarek Jenny Shin Katrin Smith Catherine Swytink-Binnema	Session Chairs

A BIG THANK YOU TO JULIANA CYR AND ALL OF OUR VOLUNTEERS WHO HELPED WITH THE ORGANIZATION AND PLANNING OF OUR CONFERENCE THIS YEAR!

A SPECIAL THANK YOU TO LISA MAYER FOR HER ONGOING SUPPORT OF OUR ANNUAL ALBERTA BME CONFERENCE

UNIVERSITY OF CALGARY
Biomedical Engineering

UNIVERSITY OF CALGARY
FACULTY OF KINESIOLOGY

PROGRAM

FRIDAY			
1:00 pm – 1:10 pm		**Welcoming Remarks – Dr. Kallos/Dr. Krawetz**	
Click here to join the Zoom meeting Meeting ID: 916 1997 0381 Passcode: 850737			
		Keynote Speaker	
1:10 pm – 1:40 pm		Chair: Michael Kallos	
1:10 – 1:15 pm		Opening remarks	
1:15 – 1:35 pm		**Ian Buchanan** Vice President Technical Solutions, Exergy Solutions	
1:35 – 1:40 pm		Discussion and questions	
Regenerative Medicine – Frontiers in BME			
1:45 – 3:11 pm		Session Chairs: Brett Abraham, Tiffany Dang	
Click here to join the Zoom meeting Meeting ID: 943 5205 4475 Passcode: 073480			
		Industry Speaker	
1:45 – 2:00 pm		**Sam Wadsworth** Chief Scientific Officer, Aspect Biosystems	
		Student Presentations	
Olsen, Alexandra	01	Enhanced fracture repair in p21-/- mice is mediated through increased callus mineralization	8 minutes
Jahromi, Mohammad	02	Finding uniform acoustic pressure for adhesive cell sonoporation	3 minutes
Upenieks, Alex	03	Development and Characterization of a Perfusion Bioreactor for the Fabrication of Bioengineered Intervertebral Disc Components	8 minutes
Colter, James	04	The future of induced pluripotent stem cell bioprocessing - Integrating large multi-dimensional datasets within models, predictive analytics, and advanced control strategies to control phenotype	3 minutes
Tholl, Emma	05	Effects of Exercise on Cardiovascular Health	8 minutes
Khan, Sonia	06	Determining Stable Cavitation Threshold for Safe BBB Disruption	8 minutes
Shah, Sophia	07	The role of epidural fat stem cells in the growth and maintenance of dural tissue	3 minutes
Kumar, Hitendra	08	Gelatin methacryloyl bioinks tailored for rapid visible light stereolithography bioprinting	8 minutes
Figueredo, Carlos Alberto	09	Faxitron DXA in analysis of bones of DSPP knockout mice	3 minutes

Oliveira Masson, Anand	10	Enhancing Articular Cartilage Regeneration by Modulating the Cell Cycle Within Mesenchymal Progenitors	8 minutes
Taberna, Thristan Paulo	11	Upstream Bioprocessing Strategies for the Large-Scale Production of Extracellular Vesicles from Human Mesenchymal Stem Cells	3 minutes
Cenaiko, Stirling	12	OpenFOAM Multiphysics Simulation Comparison to Commercial Software for Electrokinetic Fluid Flow of Conductive Biofluids in Microchannels	8 minutes
		Imaging - Medical	
1:45 – 3:11 pm		Session Chairs: Jenny Shin, Thomas Lijnse	
		Click here to join the Zoom meeting Meeting ID: 990 8603 1165 Passcode: 072686	
		Industry Speaker	
1:45 – 2:00 pm		**Estee Lee**, Core MR Development, Circle Cardiovascular Imaging Inc.	
		Student Presentations	
Pedenko, Kassondra	13	Evaluating the role of white matter development in literacy and mental health.	8 minutes
Hesselink, Jake	14	Identifying auditory artifacts in small rodent focused ultrasound neuromodulation	3 minutes
Chung, Kevin	15	Deep Learning to Improve the Diagnostic Potential of Low-dose CT	8 minutes
Sharleen, Patricia	16	Monitoring Breast Treatment with Microwaves: Consistency of Scans of the Healthy Breast	3 minutes
Siddiqui, Maryam	17	Localized Mild Hyperthermia Using MRI Guided High Intensity Focused Ultrasound in Tumour-Bearing Mice for Potential Cancer Therapies	8 minutes
Smith, Katrin	18	Microwave Imaging for Radiation Treatment Monitoring: Strategies for Incorporating Clinical Data	8 minutes
Rai, Shefali	19	Precision Mapping of Functional Brain Networks in Children	3 minutes
Remesz, Ross	20	3-Dimensional Geometric Trends of Coronal Sutures	8 minutes
Shrestha, Shirshak	21	Estimating thickness and speed of sound of layered material using a low-frequency imaging linear-array	3 minutes
Pearce, Sabrina	22	Use of Functional Near-Infrared Spectroscopy (fNIRS) Coherence to Analyse the Effect of Task Execution in the Frontal and Motor Cortices	8 minutes
Li, Siyun	23	Breast Tissue Mimicking Phantoms for Combined Microwave and Ultrasound Imaging	3 minutes
Hosseinpour, Zahra	24	Validating image texture analysis by assessing fresh postmortem MRIs from patients with multiple sclerosis	8 minutes

3:15 – 3:45 pm		**Question & Answer Session** Regenerative Medicine – Frontiers in BME Imaging - Medical	
Join the conversation on SpatialChat			
Biomechanics			
3:45 – 4:56 pm		Session Chairs: James Colter, Alanna Devolin	
Click here to join the Zoom meeting Meeting ID: 917 9972 5618 Passcode: 594624			
Salem, Mohammad	25	Development of Micro Numerical Model of Distal Radius Fractures	8 minutes
Der, Jason	26	A Computer Vision Method for Dynamic Compliance Measurement in Ex Vivo Lung Perfusion	3 minutes
Ihsan Ali, Safia	27	Pressure and Energy Loss Analysis in Atrial Septal Defect	8 minutes
Heydati, Nassim	28	Investigating White Line Separation as a Potential Precursor to Toe Tip Necrosis	3 minutes
Beltran Martinez, Karla	29	Analysis of muscle activity and muscle fatigue during a material handling tasks	8 minutes
Gadzella, Timothy	30	Design of an Ex Vivo Mechanical Test Apparatus to Study Atraumatic Tooth Extraction	8 minutes
Santosuosso, Emma	31	Frontlimb and hindlimb kinematics in horses during swimming	3 minutes
Palichuk, Bryce	32	Optimization of pulsatile flowmeter for use in ex-vivo heart perfusion device	8 minutes
Pan, Boyu	33	Effect of Upper Arch Expansion by Invisalign on Nasal Airway Volume in Children	3 minutes
Kim, Hansuk	34	Left Ventricular Flow Analysis in Atrial Fibrillation	8 minutes
Bessa, Guilherme	35	Optimization of ex-vivo heart perfusion (EVHP) systems and the effect of compliance properties on the flow	3 minutes
Ramrattan, Darius	36	Chondrocyte Morphological Response during Cyclic Dynamic Loading	8 minutes
Imaging - MSK			
3:45 – 4:56 pm		Session Chairs: Catherine Swytink-Binnema, Conrad Mielczarek	
Click here to join the Zoom meeting Meeting ID: 971 0151 1103 Passcode: 513062			
Besler, Bryce	37	Bone Morphometry from Level Set Embeddings	8 minutes
Sacher, Alexander	38	Regional depth-specific subchondral bone density measures in osteoarthritic and normal distal femora: in vivo precision and links with pain	3 minutes
Mohamed, Nada	39	Surface Topography for Evaluation of Schroth Exercise in Adolescents with Idiopathic Scoliosis: A randomized Controlled Trial (RCT)	8 minutes

Klassen, Rachel	40	Assessment of Bone Quality using HR-pQCT in Females with Celiac Disease, Inflammatory Bowel Disease and Systemic Lupus Erythematosus	3 minutes
Smith, Ainsley	41	Validation of phantom-less calibration for CT muscle analysis	8 minutes
Egeonu, Imanma Tiffany	42	Automating Depth-Specific Density Analyses of the Patella	3 minutes
DiMaio, Rachel	43	Do hip fracture patients experience asymmetrical bone loss after fracture?	8 minutes
Wang, Kendra	44	Design and Construction of a Passive Motion Device for Dynamic CT Scans of the Trapeziometacarpal Joint	3 minutes
Wong, Murray	45	4DCT Shows Improved Syndesmotic Motion after Flexible Fixation Compared to Rigid Fixation	8 minutes
Kemp, Tannis	46	Modeling Participant-Specific Bone Atrophy During Spaceflight	8 minutes
Abid, Aleena	47	Validating Periosteal and Endosteal Localization in the Femur of Clinical Computed Tomography Datasets	3 minutes
Kuczynski, Michael	48	Reproducibility of Trapeziometacarpal Joint Angle Measurements Using Dynamic Computed Tomography	8 minutes
Rehabilitation, Wearables & Health Monitoring			
3:45 – 4:56 pm		Session Chairs: Katrin Smith, Thomas Lijnse, Tiffany Dang	
Click here to join the Zoom meeting Meeting ID: 986 4882 0427 Passcode: 649401			
Khandan, Aminreza	49	Ice-Skating Temporal Events Detection Using Inertial Sensors Data	8 minutes
Lu, Sophia	50	Negative Pressure Ventilation in the Shortfall of COVID-19 Ventilators: A Review	3 minutes
Khan, Alhamd	51	IMU based finger band remote controller-A preliminary method towards developing assistive data gloves for stroke rehabilitation	8 minutes
Lamb, Alec	52	Development of a multifunctional electrical cuff for peripheral nerve monitoring and regeneration.	3 minutes
Islam, Md Manirul	53	Selection of an IoT Data Analytics Platform for a Wireless Sensor Technology for Tele-Rehabilitation Assessments of Remote Wheelchair Users	8 minutes
Moscoso, Graciela	54	Comparing 2D and 3D AC Electrothermal Device Models	8 minutes
Gardner, James	55	Computer Algorithm for Automated Detection of Ventilatory Thresholds from Cardiopulmonary Exercise Testing Data	3 minutes
Yip, Tyler	56	Benefits of Cyclist Green Waves Using Wearables	8 minutes
Russell, Monica	57	Effect of Axillary Crutch Length on Latissimus Dorsi Activation During Swing-Through Gait	3 minutes

Farooq, Ayesha	58	Stroke Patient Body Position Analysis Using Pressure Sensor Array Data	8 minutes
Potvin, Sacha	59	Adjustable Balance Board for Rehabilitation	3 minutes
van de Panne, Lisa	60	Assessing Microelectrode Simulation Techniques	8 minutes
5:00 – 5:30 pm		**Question & Answer Session** Biomechanics Imaging – MSK Rehabilitation, Wearables & Health Monitoring	
Join the conversation on SpatialChat			
5:30 pm – 5:40 pm		**Closing Remarks – Dr. Kallos/Dr. Krawetz**	
Click here to join the Zoom meeting Meeting ID: 925 6400 2090 Passcode: 176284			

UNIVERSITY OF CALGARY
Biomedical Engineering Graduate Program

The Biomedical Engineering Graduate Program at the University of Calgary offers a unique opportunity to work with leading researchers across campus to advance knowledge and find solutions to improve human animal health and wellness. Collaborate with world-leading researchers in Engineering, Kinesiology, Medicine, Nursing, Science and Veterinary Medicine to make new discoveries, to expand the field of biomedical engineering and make a difference in the lives of people around the globe.

The Biomedical Engineering Graduate Program is a key component of The University of Calgary's Eyes High vision and supports both the university's academic and research plans, particularly the strategic research theme

Engineering Solutions for Health: Biomedical Engineering. It is an established program supporting a diverse research community with a strong focus on student success.

Priority Research Themes

Integrated approaches to enable prevention of injury and disease and support healthy aging

Goal: To invent and implement technologies that will keep people healthy and minimize complications from diseases, while also helping predict injury and illness.

Engineering methodologies can increase our fundamental understanding of human and animal health and disease across the lifespan. Based on this understanding, new integrated biomedical engineering technologies and solutions will be created for monitoring health and promoting prevention. Imagine a family member recovering from a heart attack – biomedical technologies will allow us to assess their disease type, limit disease progression and prevent loss of quality of life, while also identifying whether younger family members are at risk for heart disease.

Technologies for improved diagnostics

Goal: To develop more accurate imaging and diagnostics to detect disease earlier, provide biomarkers for evaluating new therapies, and enable personalized treatments optimized for the individual patient.

Early and accurate detection is crucial to precisely identify and treat the correct disease or dysfunction. Biomedical engineering offers ways to develop new instrumentation, data handling systems, and technologies that assess organ and body function, dysfunction, and disease at earlier stages, with higher sensitivity, and with more high quality information. Having an earlier and more accurate diagnosis greatly improves the chances of successful treatment leading to better outcomes following injury or disease.

Engineered novel therapeutics

Goal: To develop high-quality, long-lasting treatments for injury and disease, based on stem cells, targeted drugs and novel devices.

Developing novel therapeutic devices and molecular medicines and harnessing the power of stem cells to exploit the body's inherent repair mechanisms will be advanced by biomedical engineering technologies. With a focus on developing new personalized treatments to repair, regenerate or replace dysfunctional cells and tissues, these integrated therapies are designed to work with the body's natural healing processes. By using the body's own cells, the need for donors is eliminated, the chance of infection is reduced, and the overall outcome is a solution that functions more closely to the native cells or tissue.

Emerging theme: Optimized health care system performance

Goal: To deliver research built on our emerging strengths, using engineering tools and approaches to improve patient flow through the health care system.

Engineering tools and approaches are ideally suited to improving the flow of patients, data and resources through the healthcare system. Research within this theme will investigate new tools for evaluating healthcare system performance and technology assessment. Operational modelling technologies at the University of Calgary will ensure that all patients are able to access the care they need by optimizing the system for delivery of care – this will maximize the chances of a full recovery from a medical event.

FOR MORE INFORMATION about applying into our Biomedical Engineering Graduate Program, University of Calgary, please contact:

Biomedical Engineering Graduate Program Office, CCIT012
Schulich School of Engineering Building, Main Campus
2500 University Drive NW, Calgary, Alberta, T2N 1N4
EMAIL: bmegrad@ucalgary.ca
https://www.ucalgary.ca/bme/graduate

Biomedical Engineering

Ready to make a difference

Located in the engineering capital of Canada, the University of Calgary's Biomedical Engineering program is advancing knowledge and solving problems in animal and human biology, medicine and health-care by educating the next generation of leaders.

Ready to contribute

Our undergraduate students have the strengths of a traditional engineering degree at the Schulich School of engineering, advanced knowledge of biomedical engineering and valuable hands-on work experience.

Multi-disciplinary teamwork

Our graduate students participate in teams with researchers in engineering, kinesiology, medicine, nursing, science and veterinary medicine at an institution committed to investing significantly in biomedical research.

Partners in Research

Researchers work towards making an impact through scientific discoveries, innovative and market-driven technologies, and solutions to enhance the wellness and well-being of all throughout the lifespan. We look for opportunities to link with industry and international entities to provide market-ready graduates and R&D solutions.

collaborative, skilled and experienced – the University of Calgary's biomedical engineers are ready to help your team make a difference today.

ucalgary.ca/bme

graduate email **bmegrad@ucalgary.ca**

undergraduate email **bioengineering@ucalgary.ca**

research email **bme@ucalgary.ca**

UNIVERSITY OF CALGARY

UNIVERSITY OF CALGARY
FACULTY OF KINESIOLOGY

Our graduates work as kinesiologists and in related careers such as health and fitness, biomechanics, exercise physiology, rehabilitation, research, nutrition, coaching, sport performance, injury prevention and more.

"I am so happy I chose this program. We have so much fun in Kinesiology, we have such a good family here and all our professors are amazing – they really want us to succeed."

- Conné Lategan, BSc in kinesiology, honours program

Kinesiology is the study of human movement and function.

Our undergraduate programs

The faculty offers a Bachelor of Kinesiology, Bachelor of Science in Kinesiology as well as a combined Bachelor of Kinesiology for a variety of majors.

BKin | BScKin

Our graduate programs

We offer a course-based Master of Kinesiology as well as a research-based Master of Science and a Doctor of Philosophy with a number of specializations.

MKin | MSc | PhD

The faculty is home to the successful Dinos varsity teams, the Olympic Oval with the fastest ice in the world, the Sport Medicine Centre, the largest Outdoor Centre in North America, more than 75 sport and recreation activities, an aquatic centre, racquet centre (racquetball, squash and tennis), fitness centre, gymnastic centre, three gyms and climbing walls.
Student memberships are included in your fees.

Kinesiology graduates lead the way to healthy, active living in our communities.

By the numbers

Our students

1100+ undergraduates

116 graduate students

28 indigenous students

57 international students

26 undergraduate honours students

30 academic staff

450+ Dinos varsity student athletes

120+ undergraduate practicum positions to gain work experience

32 undergraduates working on research projects

37 graduate students awarded prestigious scholarships

In 2018, the Faculty of Kinesiology was ranked the No. 1 sport science school in North America and No. 7 globally (ShanghaiRanking 2018).

Our university

#6 top research university in Canada for sponsored research funding

Since 1976, Dinos student-athletes have brought home **more than a dozen Olympic medals**

Top 5 in Canada for Academic All-Canadian student-athletes

Beautiful 200 hectare campus is only a **40 minute drive to the Rocky Mountains**

180,000 Alumni
Graduates include Olympians like Hayley Wickenheiser and Erica Wiebe

Our city

#1 most liveable city in North America - #4 worldwide

4th largest and fastest -growing city in Canada

Fastest-growing tech talent in Canada

Largest urban pathway network in North America

More than 8,000 hectares of **parkland and natural areas**

Sunniest city in Canada – more than 333 days a year

Ready to learn more?

Contact a kinesiology advisor at knesinfo@ucalgary.ca or visit kinesiology.ucalgary.ca.

UNIVERSITY OF CALGARY

Enhanced fracture repair in p21$^{-/-}$ mice is mediated through increased callus mineralization

Alexandra Olsen[1,2], Priyatha Premnath[3], Scott Brunet[1,2], Neil Duncan[1,2], Derrick Rancourt[1,2], Roman Krawetz[1,2]
[1]Biomedical Engineering Graduate Program, UCalgary, [2]McCaig Institute for Bone and Joint Health, [3]University of Wisconsin, College of Engineering and Applied Science.

Introduction: During fracture healing, there are two primary osteogenic pathways: intramembranous ossification and endochondral ossification, with the latter being the most common healing pathway in long bone fractures. Marcucio *et al* (2015) developed a non-critical unstabilized transverse tibial fracture model (Figure 1) that promotes endochondral ossification. This model has been utilized to assess differences in bone regeneration potential [1]. p21 is a cell cycle regulator and has recently been implicated in the chondrogenic and osteogenic differentiation of mesenchymal stem cells (MSCs) [2]. Our lab has reported that p21 knockout (p21$^{-/-}$) mice demonstrate enhanced bone regeneration following burr hole injury [3]. While it is known that p21$^{-/-}$ mice demonstrate increased intramembranous ossification (burr hole model), it remains unknown if p21$^{-/-}$ mice also demonstrate increased endochondral ossification repair mechanism. Therefore, the purpose of this study was to utilize a multi-modal approach: biomechanics, *in vivo* imaging and histology to asses if p21$^{-/-}$ mice have enhanced bone regeneration following a transverse-tibial fracture.

Methods: Two mouse strains were used for this project, C57BL/6 (wild-type control) and p21$^{-/-}$ both carrying a *Prx1*$^{CreERT2\text{-}GFP}$; ^{R26RTdTomato} transgenes to lineage trace endogenous MSCs. Fractures were generated in the mid-diaphysis (Figure 1). Mice were scanned at 2 (n=6 per strain) and 4 (n=4 per strain) weeks post fracture using *in vivo* micro-CT. Total volume (TV), bone volume (BV), and bone mineral density (BMD) were calculated post segmentation. Three-point bending tests (n=2) were conducted to determine the ultimate strength and toughness of the healed tibiae.

Results: Biomechanical testing demonstrated the mean strength of the fracture callus in C57BL/6 fracture callus was 13.6N vs. 15.8 N in p21$^{-/-}$ mice. Mean toughness of the callus was 2.4 N-mm in C57BL/6 mice vs. 7.2 N-mm in p21$^{-/-}$ mice. The mean callus BMD at 4 week in C57BL/6 mice was 134.9 mg HA/ccm vs 165.9 mg HA/ccm in p21$^{-/-}$. The mean average BMD in C57BL/6 mice was 309.6 mg HA/ccm vs 321.1 mg HA/ccm in p21$^{-/-}$. The mean BV/TV in C57BL/6 was 0.27 vs 0.43 in p21$^{-/-}$. Callus BMD, average BMD, and callus BV/TV were signfigant at week 2 and 4.

Conclusions: The micro-CT data suggests that during fracture repair (Figure 2.), the callus of a p21$^{-/-}$ has increased mineralization at 2- and 4- weeks post-injury. I am unable to draw conclusions regarding the biomechanical testing until the sample size is increased. Going forward, I will examine if endogenous MSCs play a role in the observed findings.

References: [**1**] Bahney, C. S., *et al*., The multifaceted role of the vasculature in endochondral fracture repair. *Front. Endocrinol. (Lausanne).* **6**, 1–10 (2015). [**2**] Yew, TL, *et al*., Knockdown of p21(Cip1/Waf1) enhances proliferation, the expression of stemness markers, and osteogenic potential in human mesenchymal stem cells. *Aging Cell* **10**, 349–361 (2011). [**3**] Premnath, P. *et al.,* P21-/- mice exhibit enhanced bone regeneration after injury. *BMC Musculoskelet. Disord.* **18**, 1–10 (2017).

Figures:

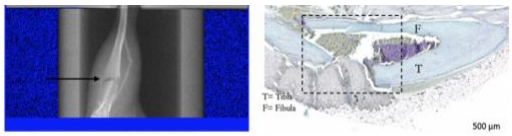

Figure 1. (Left)Static X-ray, the arrow indicates the fracture. (Right) Fast green andSafranin-O staining of the fracture at time point zero. The box represents the fracture site.

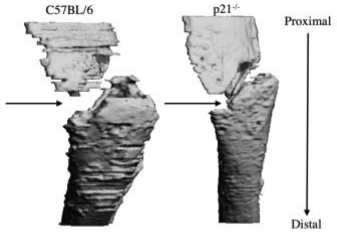

Figure 2. Week 4 fracture site. Image created via micro CT.

Finding uniform acoustic pressure for adhesive cell sonoporation

Mohammad Jahromi[1], Laura Curiel[1]
[1]University of Calgary, 2500 University Drive NW, Calgary, AB, T2N1N4
E-mail: mohammad.jahromi@ucalgary.ca, laura.curiel@ucalgary.ca

Introduction

Ultrasound has been used as a therapeutic tool in physiotherapy and non-invasive surgery by thermal ablation of tissues. More recent works propose the use of ultrasound for drug delivery and gene delivery. Cell permeabilization using microbubbles and ultrasound is the mechanism proposed for these applications. The collapsing bubbles undergo cavitation under ultrasound exposure, and generate mechanical effects that cause transient cell permeability, referred to as sonoporation [1]. When conducting such studies, it is essential to control the pressure to which the cells are exposed, which determines their response.
It is important when designing sonoporation studies to ensure the pressure is uniform. The objective of this work was to determine a metric to evaluate pressure uniformity when using a planar transducer and build a device for cell sonoporation in adherent cells.

Methods

The acoustic field of a 30-mm planar disc piezoelectric transducer at three different frequencies (330 kHz, 500 kHz and 1 MHz) was simulated using the k-wave toolbox [2] and used to determine metrics for uniformity within a 24-well cell plate for cell culture placed at different distances from the transducer surface.

Transducers were then built, and their acoustic field measured using a needle hydrophone to confirm a uniform area could be obtained.

The deviation from the mean pressure value within the well was selected as the primary metric for uniformity. Additional metrics were analyzed, including standard deviation and percentage between the maximum and minimum pressure within the well.

Results

Figure A shows the final measured pressure at the depth where the highest uniformity was obtained. This distance depended on the frequency (47 mm at 1MHz, 74 mm 500 kHz and 48 mm at 330 kHz). We achieved an area where 80% (at 1MHz), 89% (at 500 kHz), and 99% (at 330 kHz) of the region within the well was within the average or a maximum deviation of 25% from this value.

A final prototype device was built with six transducers to achieve exposure of the 24-well plate.

Conclusion

A uniform region for cell exposure to ultrasound in adherent cells was defined and allowed the design of a device for sonoporation. Future work will evaluate the bio-effects of ultrasound exposure on cells using the designed prototype.

References

[1] Y. Watanabe *et al.*, “Low-intensity ultrasound and microbubbles enhance the antitumor effect of cisplatin,” *Cancer Sci.*, vol. 99, no. 12, pp. 2525–2531, 2008.

[2] B. E. Treeby and B. T. Cox, “k-Wave: MATLAB toolbox for the simulation and reconstruction of photoacoustic wave fields,” *J. Biomed. Opt.*, vol. 15, no. 2, p. 021314, 2010.

Figures

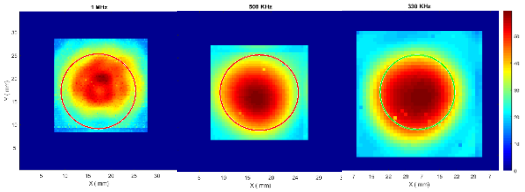

(A)

Development and Characterization of a Perfusion Bioreactor for the Fabrication of Bioengineered Intervertebral Disc Components

Alex Upenieks[1], Dr. J. Paul Santerre[1,3], Dr. Rita A. Kandel[1,2]
[1]Biomedical Engineering and [2]Laboratory Medicine and Pathobiology, [3]Ted Rogers Centre for Heart Research and Faculty of Dentistry, University of Toronto
164 College St Room 407, Toronto, ON

Introduction

The intervertebral disc is the soft tissue that anchors adjacent vertebral bodies in the spine and is composed of a centrally located nucleus pulposus (NP) surrounded by a multi-lamellated annulus fibrosus (AF). Degeneration of the intervertebral disc (IVD) contributes to disability globally. Current treatments consist of physical therapy, pharmacotherapy, discectomy, lumbar fusion, or simple exercise, however these solutions do not restore full disc function, and can cause further complications [1]. One therapeutic approach to treating degeneration would be to substitute the damaged disc with a live-tissue engineered construct. Such discs could be generated in perfusion bioreactor culture systems, which have been shown to improve nutrient delivery and provide beneficial shear forces for the maintenance of large 3D constructs[2]. To date, our lab has generated such constructs in stirred bioreactors[3], but these are limited in size due to diffusion limitations and dimensional constraints. The hypothesis of this study is that a perfusion bioreactor will yield culture conditions superior to static culture and spinner bioreactor culture systems for tissue engineered NP and AF tissues. Superiority will be based on ECM content, ECM quantification, rate of tissue growth, and tissue distribution.

Methods

AF and NP tissues are harvested from bovine caudal discs. Outer AF cells are isolated and seeded on multilamellar angle-ply nanofibrous/degradable polyurethane scaffolds in spinning bioreactors to enable AF cell adhesion and early tissue generation over one week *in vitro*. AF cells are then then transferred to a perfusion reactor and cultured another week. Isolated NP cells are seeded onto a calcium polyphosphate bone substitute and grown for one week in static culture, then inserted into the AF construct and cultured for one week under perfusion conditions. Tissues are evaluated histologically and immunostained for extracellular matrix components, ECM quantifications, rate of tissue growth, and assessment of tissue distribution.

Results

A custom perfusion bioreactor has been successfully designed, fabricated and characterized. It has been used to culture bioengineered IVD components. The perfusion reactor was designed to reduce/eliminate leaking, contamination, or air bubbles, and provide a compatible growth environment for intervertebral disc tissues (data not shown). To date the perfusion bioreactor has successfully produced the AF portion of the IVD, and early NP cell cultures were shown to form tissue rich in proteoglycans

Conclusions

These studies demonstrate that perfusion culture supports the formation of two critical tissues present in the IVD, the AF and NP. Early experiments demonstrate that perfusion conditions yield AF tissues superior to static conditions, and tissues comparable to spinner reactor conditions. Further characterization of NP and AF tissues is ongoing and will be reported on.

References

1. Brox, J. I. et al. Ann. Rheum. Dis. 69, 1643–1648 (2010).
2. Pfannkuche, J.-J., et al., Connective Tissue Research. 61, 1–18 (2018)
3. Iu, J.,Santerre, J. P., & Kandel, R. A. (2017). Tissue Engineering. Part A, 23(17–18), 1001–1010.

Acknowledgements: CIHR Project Grant #MOP142325

The future of induced pluripotent stem cell bioprocessing - Integrating large multi-dimensional datasets within models, predictive analytics, and advanced control strategies to control phenotype

James Colter[1,2,7], Breanna Borys[1,7], Tania So[1], Ian Lewis[3,6], Kartikeya Murari[4,7] Michael Kallos[1,5,7]

[1]Pharmaceutical Production Research Facility, [2]Integrated Circuits and Optical Imaging Laboratory, [3]Calgary Metabolomics Research Facility, [4]Department of Electrical and Computer Engineering, [5]Department of Chemical and Petroleum Engineering, [6]Department of Biology, [7]Biomedical Engineering Graduate Program, Schulich School of Engineering, University of Calgary, 2500 University Drive NW, Calgary, AB, Canada T2N 1N4

Insights into intracellular regulation of pluripotent phenotype and response to environmental stimuli have revealed complex interaction networks consolidating the nexus of gene expression, epigenetic regulation, metabolic pathway activity, cell cycle dynamics, and structural organization. The subtleties of this network are further complicated by activity introduced through induction of pluripotency from somatic phenotypes, including increased population heterogeneity, age-related genetic aberrations, abnormal epigenetic marks, changes to regulation of cell cycle, and metabolic differences. The environmental niche plays a critical role in regulating the cell population. Mechanical forces, growth factors, inhibitors, and nutrients within the niche heavily influence regulation of phenotype. Within the context of the bioprocess, inadequate control over the intersection of these dynamics within a batch and over successive passages translates to abnormal and heterogeneous phenotypes, clonal dominance activity, immunogenic potential, tumorigenic advantage, and altered functional characteristics in the downstream therapeutic cell product. Recent studies by our group have elucidated unique metabolic pathway activity of human iPSCs cultured in dynamic suspension under varied oxygenation conditions. The results show distinct metabolic trajectories between conditions, coupled with significant differences in proliferation, aggregate morphology, and nutrient consumption. Our investigation of metabolism shows important interplay between cell activity, cell state, and the process environment. Our datasets provide compelling evidence to suggest manipulation of pluripotent phenotype through alteration of process conditions. Integration of additional omics platforms and the application of computational methods to model interactions between and within the environment and the cell will allow us to describe the interplay between modulation of process conditions and cellular response, guiding advanced process control and intervention.

Effects of Exercise on Cardiovascular Health

Emma Tholl, Georgios Mitsis and Marc Poulin
Schulich School of Engineering, University of Calgary, Calgary Alberta
Department of Bioengineering, McGill University, Montreal Quebec
Department of Physiology & Pharmacology, Cumming School of Medicine, University of Calgary, Calgary Alberta

Introduction

It is now well established that physical activity is one of the best approaches for a healthy body and mind. As medical technology continues to evolve, and the human life expectancy increases, it is important to ensure that the quality of life remains intact. The goal of Brain in Motion (BIM) is to learn more about the mechanisms by which improvements in cardiorespiratory fitness enhances cognitive performance.

Methods

The BIM study focuses on investigating the effects of exercise on older adults (men and women) aged 55-80+ years. Participants undergo a longitudinal study where data is collected at multiple phases over time, including a six-month-long supervised aerobic exercise intervention. The data collected include various cardiovascular parameters such as cerebral blood flow and VO_2max that were recorded under different conditions (rest, submaximal exercise, hypercapnia). At the beginning and end of the study, participants also performed a Montreal Cognitive Assessment (MoCA), which is a screening test to assess those with mild cognitive impairment and dementia. Previous students have been analyzing this data using programming languages (i.e., MATLAB), to produce graphs and other visual displays. From here, I was able to build upon previous work by looking deeper into parameter relationships and integrating the changes observed in MoCA scores. I mainly focused on the use of MATLAB and Excel to relate datasets and explore relationships using figures.

Results

One approach to explore middle cerebral blood flow velocity (VP; an index of cerebral blood flow) was to separate the participants based on sex (males, females) and then look at who had the most positive and negative changes in VP from the beginning to the end of the study. The participants who had a negative change from the end of the exercise intervention to the end of the study were considered the "bottom" and seemed to have all had a positive increase in VP during the intervention. Another interesting finding involved the relationship between a participant's VO_2max and MoCA scores. For this graph, participants were separated based on their sex and had their VO_2max at each phase plotted against their age at the beginning of the study. From here, participants who had a significant change in MoCA score during the study were highlighted. This showed a pattern where the highlighted participants tended to have a lower VO_2max across all phases in comparison to the overall sample.

Conclusions

Moving forward, there are opportunities to continue exploring these extensive datasets to discover new relationships. One field of interest that could be beneficial is machine learning. Machine learning could allow for the creation of computer algorithms to predict the participants future outcomes and detect (or predict) oncoming health problems.

References

Laboratory of Human Cerebrovascular Physiology: https://cumming.ucalgary.ca/labs/human-cerebrovascular-phys/human-cerebrovascular-phys

Determining Stable Cavitation Threshold for Safe BBB Disruption

Sonia Khan[1], Laura Curiel[1], Mike Smith[1]
[1]University of Calgary, 2500 University Drive NW, Calgary, AB, T2N1N4
e-mail: sonia.khan1@ucalgary.ca, laura.curiel@ucalgary.ca, smithmr@ucalgary.ca

Introduction

Blood-brain barrier (BBB) is a major hinderance for tumour-specific therapies and drug delivery to the central nervous system. Recent studies show focused ultrasound (FUS) combined with microbubbles as a promising technology for safe and reversible BBB disruption. Cavitation, which is a mechanical effect of FUS, maybe the key principle for BBB disruption, where oscillating microbubbles force apart tight cell junctions by exerting pressure on the endothelium.

Methods

The objective is to drive the ultrasound transducer at a pressure that sustains stable cavitation for all sonications while avoiding inertial cavitation which causes shock waves leading to permanent damage of the BBB. Stable cavitation is manifested by presence of subharmonics and ultra-harmonics of the fundamental frequency of the driving signal on analyzing data captured by a hydrophone [1]. The current metric to detect stable cavitation threshold is evaluating area under the curve (AUC) in a 300Hz bandwidth around the subharmonic frequency of original spectrum. We first acquired a series of open loop responses on an animal BBB system (RK50, FUS Instruments) where we varied the pressure from 0.1 MPa to 0.99 MPa and observed cavitation response. The received acoustic signal is processed by MATLAB by windowing and zero padding before being transformed into the time domain. The processed spectrum is then compared to the original spectrum acquired from the system to determine the best metric that can be used as a threshold for stable cavitation detection (Fig. A).

Results

Windowing the data reduces Gibbs' ringing artefacts, making the subharmonic more dominant above the noise. The spectrum now shows that the subharmonic's actual bandwidth is approximately 1 kHz, making the current 300 Hz bandwidth too small and likely to underestimate the AUC. Zero padding in the time domain interpolates the time domain signal providing a better chance to use AUC with a suitable bandwidth as a metric to detect and sustain stable cavitation.

Conclusions

The proposed analysis is promising to determine better metrics, besides AUC, to detect stable cavitation and may facilitate the designing of a controller to sustain stable cavitation for safe and reversible BBB disruption using FUS. Future work includes adjusting the bandwidth to make a better estimation of AUC and we will integrate the new metrics into the current RK50 system for BBB animal experimentation.

References

[1] M. O'Reilly and K. Hynynen, "Feedback-controlled Focused Ultrasound Disruption by Using an Acoustic Emissions – based Controller," Radiology, vol. 263, no. 1, pp. 96–106, 2012.

Figure

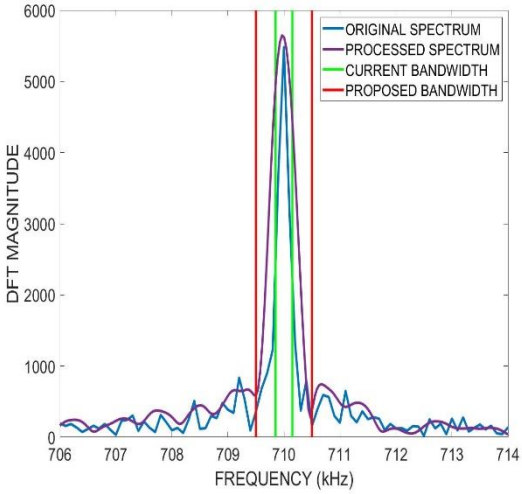

Fig. A: Plot showing original spectrum with current 300Hz bandwidth and processed spectrum with proposed 1kHz bandwidth.

The role of epidural fat stem cells in the growth and maintenance of dural tissue

Sophia Shah, Sathvika Mudigonda, Paul Salo, Alim Mitha and Roman Krawetz
University of Calgary, 3280 Hospital Dr NW, Calgary, AB T2N 4Z6

Introduction: Mesenchymal stem cells (MSCs) are multipotent adult cells known to play several physiological roles *in vivo* including tissue maintenance and repair[1]. MSCs are present in many adult connective tissues but for yet unknown reasons, typically display greater proliferative and differentiation capacity when derived from adipose tissue[2]. Our group has recently identified MSC populations within epidural fat (EF) and the adjacent dura mater- the outermost protective membrane surrounding the spinal cord[3]. Clinically, EF is frequently considered an inert, space-filling tissue; therefore, it is commonplace for clinicians to remove and discard it during spine surgery to increase their operational field of view. As the development and cellular origins of both EF and the dura are unclear, I hypothesized that EF-MSCs contribute to the maintenance of dural integrity throughout growth. Moreover, if EF-MSCs are responsible for maintenance of the dura, then these cells should also have the potential to respond to dural injury.

Methods: To test this hypothesis, (1) EF-MSCs were identified and lineage traced *in vivo* during growth and in a skeletally mature model using a *Prx1* reporter mouse (*Prx1*^{CreERT2GFP};R26R^{TdTomato}). (2) EF-MSCs were ablated by crossing these mice to an R26R^{DTA} mouse (diphtheria toxin A), and subsequent effects were observed in the spinal cord/dura via α-smooth muscle actin (α-SMA) staining, an isoform of actin. (3) A dural injury was generated in the *Prx1* reporter mice to determine if EF-MSCs can contribute to dural injury repair.

Results: (1) *Prx1* positive MSC migration was observed from the epidural fat to the dura during normal growth (8 through 12 weeks of age). Accumulation of Prx*1* positive MSCs was observed over time, with the dura enriched for these cells by 4-weeks post tamoxifen induction. In contrast, at skeletal maturity (4 months of age), single *Prx1* positive MSCs were interspersed throughout the dura. (2) The α-SMA staining pattern, which is normally continuous throughout the dura, was punctate throughout the dura mater when *Prx1* positive MSCs were ablated. (3) Two weeks post-injury, *Prx1* positive MSCs were found within the injury region of the dura.

Conclusions: This study demonstrates that EF-MSCs are involved in growth, maintenance and repair of dural tissue. Dural integrity is essential to contain the cerebrospinal fluid and protect the spinal cord from mechanical injury and infection[4]; untreated dural ruptures can lead to severe complications. Our findings that EF-MSCs contribute to dural repair indicate that the common practice of discarding EF during surgery should be re-visited. This conclusion is strengthened by our data that shows a loss of dural integrity in an otherwise normal animal when EF-MSCs are ablated (**Fig. 1**). This project refutes the prevalent notion of EF as biologically insignificant.

References: (1) A.M. DiMarino, et al., "Mesenchymal stem cells in tissue repair," *Frontiers in Immunology*. 2013, doi:10.3389/fimmu.2013.00201. (2) L. Frese, et al., "Adipose tissue-derived stem cells in regenerative medicine," *Transfusion Medicine and Hemotherapy*. 2016, doi: 10.1159/000448180. (3) N. Al-Jezani, et al.,"Isolation and characterization of an adult stem cell population from human epidural fat," *Stem Cells Int.*, vol. 2019, 2019, doi: 10.1155/2019/2175273. (4) G. Schütze, "Epiduroscopic Diagnostics," in *Epiduroscopy spinal endoscopy*, Heidelberg: Springer, 2008, pp. 10–16.

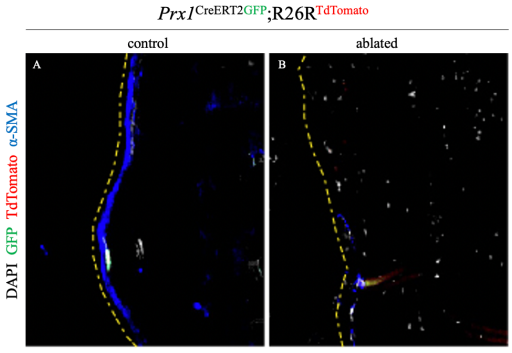

Figure 1. The α-SMA staining pattern which is continuous throughout the dura (A) becomes discontinuous when *Prx1* positive MSCs were ablated (B).

Gelatin methacryloyl bioinks tailored for rapid visible light stereolithography bioprinting

H. Kumar[1, 3], K. Sakthivel[1], E. Boras[2], S. R. Shin[4] and K. Kim[1, 3, *]

[1]School of Engineering, The University of British Columbia, Kelowna, BC, V1V 1V7, Canada

[2]Department of Mechanical Engineering, The University of British Columbia, Vancouver, V6T 1Z4, Canada

[3]Department of Mechanical and Manufacturing Engineering, University of Calgary, Calgary, Alberta, T2N 1N4, Canada

[4]Division of Engineering in Medicine, Department of Medicine, Harvard Medical School, Brigham and Women's Hospital, Cambridge, MA 02139, USA.

Introduction

Design and selection of suitable bioink is an indispensable requirement for the bioprinting method as well as deciding the macro and microscale properties of the scaffolds. This work focuses on visible light photo-polymerizable bioinks derived from gelatin for stereolithography (SLA) bioprinting. Ideal bioink for STL bioprinting should have low gelation temperature and fast photo-crosslinking to achieve high resolution. Three synthesis factors were investigated to tune physical properties and photo-crosslinking behavior of bioinks and the biocompatibility was assessed by fabricating scaffolds with astrocytes.

Methods

Gelatin methacrylate (GelMA) was synthesized by methacrylate substitution on gelatin using glycidyl methacrylate (GMA). The reaction was done in dimethyl sulfoxide (DMSO), phosphate buffered saline (PBS) or bi-carbonate buffer (CB) solvents for duration of 3 or 12 hours at initial high pH (9) or low pH (3.5). Next, the solution was dialyzed against deionized water and lyophilization to obtain GelMA foam. The degree of substitution (DS) of GelMA was characterized using ^{1}HNMR spectroscopy. The bioink was prepared with 10% GelMA macromer and Eosin-Y photoinitiator system. Hydrogel samples were formed by crosslinking using a visible light DLP bioprinting system. Compressive modulus and photo-crosslinking kinetics were measured using a micro-mechanical testing machine. Bioprinting was performed using an SLA bioprinter. U118 astrocytes were encapsulated in the scaffold. Printed samples were cultured in cell culturing media (90% DMEM, 10% FBS, 1% penicillin-streptomycin). The cell morphology was observed on day 30 by staining nuclei with DAPI and cytoskeleton with Phalloidin.

Results

The synthesized bioinks were found to have gelation point lower than room temperature. Presence of an organic base in DMSO resulted in high DS. CB and PBS solvents also exhibited high DS for 12-hour synthesis for all pH conditions (A). However, high pH for 12 hours also extensively hydrolyzed gelatin and prevented hydrogel formation (PBS-12h-H & CB-12h-H). Hydrolysis in high pH also resulted in low modulus (B). Further, CB with 3-hour reaction at low pH caused less hydrolysis and moderate substitution of large GMA moiety, resulting in higher modulus. The mass uptake capacity exhibited inverse behavior as modulus (C). Change in reaction parameters also resulted in bioinks with diverse photo-crosslinking behavior (D). CB-3h-L was found suitable for SLA bioprinting with high strength and rapid photo crosslinking. Bioprinting experiments show the capability to rapidly (~60-90s) fabricate high resolution features (E(i)). The astrocytes in printed scaffold show elongation and integration with the hydrogel matrix.

Conclusions

A combination of solvent, pH and reaction duration were shown to tune the properties of the bioink. Low gelation point and high resolution bioprinting makes the bioinks ideal for SLA bioprinting. Growth of cells within the hydrogel scaffolds highlights the applicability of these bioinks in regenerative medicine. Along with the bioink synthesis, this investigation also presents insights into designing the bioink for targeted tissue types and bioprinting processes

References

Kumar et. al. "Tailoring gelatin methacryloyl (GelMA) bioinks for visible light stereolithographic 3D bioprinting", Macromol. Biosci. (in revision).

Figures

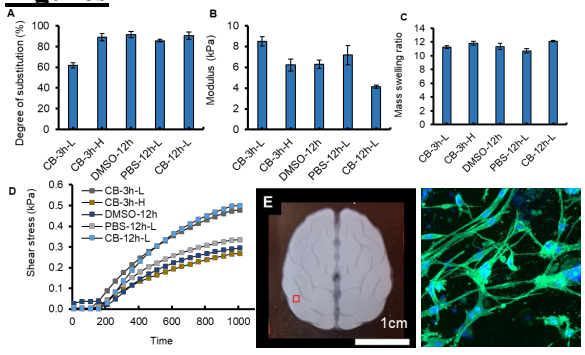

Faxitron DXA in analysis of bones of DSPP knockout mice

C. Figueredo, M. Gibson
School of Dentistry, Faculty of Medicine & Dentistry
5-508 Edmonton Clinic Health Academy (ECHA)
11405 - 87th ave | University of Alberta | Edmonton, Alberta | Canada T6G 1C9

Introduction

Dentin sialophosphoprotein (DSPP) is a non-collagenous protein that is vital in the formation of the dentin in teeth. Mutations of DSPP in human teeth are associated with dentinogenesis imperfecta, an autosomal dominant inherited disease characterized by severe dentin hypomineralization that usually results in early tooth loss. [1] It was previously known that DSPP only affects the teeth, with both mice and humans demonstrating dentin hypomineralization phenotypes when DSPP mutations are present. Recent interest in DSPP has led to more research, finding that the expression of this protein is also present in long bones, craniofacial tissues, and a noticeable prominence in the mandibular condyle cartilage (MCC), an important mandibular developmental region. [2] This aim of the present study is to better analyze the effects of DSPP deletion in mandibular condyle development.

Methods

To analyze the effects of DSPP in mandibular development, we are comparing mice with the DSPP gene deleted (DSPP-KO) and Wild Type (WT) mice at 1, 3 and 6 months of age. The animal protocol has been approved by the Animal Care and Use Committee at the University of Alberta.

Faxtiron Dual energy x-ray absorptiometry (DXA) system was used to generate high resolution x-rays for morphology analyzes and to measure bone mineral density (BMD) in regions of interest of the mandible. Two regions of interest were selected: molars, as a control region where we expected lesser mineralization in accordance with published literature, [2] and MCC.

Results

Faxitron yielded high resolution x-ray and bone mineral density values.

In WT molars, for 1, 3 and 6 months, the BMD mean results were 89.35(±1.34), 94.9(±1.64), and 98.8(±5.88), respectively. In KO molars, for 1, 3 and 6 months of age, the BMD mean results were 60.98(±8.05), 72.07(±6.27), and 78.58(±4.30). In WT MCC, results for BMD means at 1, 3 and 6 months of age were 39.06(±3.32), 70.32(±2.58), and 74.13(±3.76), respectively. In KO MCC, results for BMD means at 1, 3 and 6 months of age were 42.42(±3.50), 59.64(±5.35), and 69.26(±6.16), respectively.

Conclusions

Results show that DSPP-KO mandibular condylar cartilages are less mineralized at 6 months of age compared to WT, indicating that DSPP has an active role during mandibular condylar development.

References

[1] S. Xiao, C. Yu, X. Chou, W. Yuan, Y. Wang, L. Bu, G. Fu, M. Qian, J. Yang,Y. Shi, L. Hu, B. Han, Z. Wang, W. Huang, J. Liu, Z. Chen, G. Zhao, and X.Kong, "Dentinogenesis imperfecta 1 with or without progressive hearing loss is associated with distinct mutations in DSPP,"Nature Genetics, vol. 27, no. 2,pp. 201–204, 2001,issn: 1061-4036.doi: 10 . 1038 / 84848. [Online]. Available:http://dx.doi.org/10.1038/84848.

[2] C Qin, J. C. Brunn, E Cadena, A Ridall, H Tsujigiwa, H Nagatsuka, N Nagai,and W. T. Butler, "The Expression of Dentin Sialophosphoprotein Gene in Bone,"Journal of Dental Research, vol. 81, no. 6, pp. 392–394, 2002,issn:0022-0345.doi: 10.1177/154405910208100607. [Online]. Available: http://dx.doi.org/10.1177/154405910208100607.

Enhancing Articular Cartilage Regeneration by Modulating the Cell Cycle Within Mesenchymal Progenitors

A.O. Masson[1], B.A Besler[1], D. Young[1], A. Dufour[1], W.B. Edwards[1], T.M. Underhill[2], R.J. Krawetz[1]
[1]University of Calgary, Calgary/AB, Alberta, [2]University of British Columbia, Vancouver/BC, Canada

Introduction: Most adult tissues contain stem/progenitor cells known to contribute to tissue maintenance and repair. While tissue-resident mesenchymal progenitor cells (MPCs) have been identified in multiple niches in the adult knee joint, articular cartilage (AC) shows poor healing capacity following injury. Previously, it has been demonstrated that the constitutive deletion of the p21 gene, a cell cycle regulator, promotes cartilage regeneration. However, the underlying mechanisms of this regenerative phenotype remain largely unknown. We hypothesized that activation of the cell cycle solely in endogenous adult MPCs would enhance cartilage regeneration *in vivo* post-injury.

Methods: To test this, we targeted the p21 downstream effector E2F1, and overexpressed it in quiescent MPCs. We developed a conditionally overexpressing $E2F1^{EGFP}$ mouse that was bred to a $Hic1^{CreERT2}$:$Rosa26^{LSL\text{-}TdTomato}$ MPC reporter mouse to generate the $Hic1^{CreERT2}$; $Rosa26^{LSL\text{-}TdTomato}$; $E2F1^{EGFP}$ offspring. TdTomato reporter gene expression and E2F1 expression was induced in MPCs following tamoxifen injections. Subsequently, all mice were subjected to full-thickness cartilage defects in the femoral groove. Knee joints were harvested at 1-, 2-, 4- and 8-weeks post-injury. Histology (2D structure/composition), high-resolution 3D X-ray microscopy (XRM imaging), immunofluorescence (lineage tracking), quantitative proteomics and biomechanics outcome measures were employed to assay for cartilage regeneration.

Results: Overexpression of E2F1 in $Hic1^{+ve}$ MPCs resulted in enhanced AC regeneration compared to controls. The defect site in control mice lacked proteoglycan staining, surface regularity, and was filled with fibrocartilage-like tissue, while articular cartilage-like tissue was observed in the E2F1 mice by 4-weeks post-injury. These differences were reflected in the histological score with significant differences between the groups by 4- and 8-weeks post-injury, which was corroborated by the high-resolution 3D imaging of the femurs, indicating an enhanced cartilage repair within E2F1 mice. Proteomic analysis demonstrated that extracellular matrix production and secretion was dysregulated between $Hic1^{+ve}$ MPCs derived from the synovium and bone marrow in E2F1 mice, with increased production of matrix proteins observed in synovium-derived MPCs. E2F1 mice demonstrated altered stiffness distribution within the repaired tissue area, with lower stiffness values compared to uninjured controls. Interestingly, while *Hic1*-lineage cells ($TdTomato^{+ve}$) were seen within the injury site in both strains, by 4-weeks after injury, few to no cells were present.

Conclusions: These findings suggest that activation of cell cycle pathways in MPCs promotes AC regeneration. Furthermore, while activated MPCs migrated to the injury site, few to no cells were seen within the newly formed fibro or hyaline-like cartilage tissues in control vs. E2F1, respectively. Therefore, while these MPCs are necessary for AC regeneration they are not responsible for new tissue formation. Hence, future studies will help elucidate the role of E2F1 overexpression and the downstream effects on bone and cartilage tissues after injury.

Upstream Bioprocessing Strategies for the Large-Scale Production of Extracellular Vesicles from Human Mesenchymal Stem Cells

Thristan Paulo Taberna[1], Jolene Phelps[2], Sara Hassanpour-Tamrin[2], and Arindom Sen[1,2]
[1]Schulich School of Engineering, [2]Biomedical Engineering Graduate Program,
University of Calgary, 2500 University Drive NW, Calgary, Alberta T2N 1N4

Introduction

Mesenchymal stem cells (MSCs) are unspecialized cells that can be isolated from various tissue such as bone marrow and fat. Due to their ability to upregulate the regeneration of damaged tissues following implantation, they are viewed as a promising therapeutic tool with broad-ranging clinical applications. It has been proposed that MSCs home to sites of injury, engraft, and differentiate into functional cells that contribute to tissue repair [1]. However, recent studies have shown that many of the observed therapeutic benefits of MSCs may actually be due to the products they secrete [2].

MSCs naturally release extracellular vesicles (EVs), heterogenous populations of spherical membrane-bound nanoparticles that contain bioactive factors. There is evidence to suggest that MSC-derived EVs (MSC-EVs) exert positive therapeutic benefits by mediating intercellular communication for processes such as proliferation, differentiation, angiogenesis, and immunomodulation [3].

Despite their great potential as therapeutics, there are key technological challenges for the large-scale production of MSC-EVs that must be addressed to advance their use towards various clinical applications.

Cell Source and Culture Medium

MSC populations sourced from different individuals vary due to factors such as age, gender, metabolic state, and presence of diseases [2]. Similarly, MSCs can further vary depending on the tissue source [2]. Using a well-characterized cell bank for production can maximize therapeutic benefits of MSC-EVs on a chosen disease state.

Using culture medium devoid of ill-defined components can reduce batch-to-batch variabilities and guarantee that observed therapeutic effects are not confounded with other factors. Further, cell culture media must also be favorable from biological, regulatory, and manufacturing perspectives.

Manufacturing Process

Traditional methods to expand MSCs use flat two-dimensional tissue culture flasks. Biologically, this method fails to accurately model the *in vivo* state, and pragmatically, this method is time-consuming and labor-intensive. Thus, manufacturing protocols that ensure scalable, controlled, and reproducible production of MSC-EVs are needed.

Bioreactors, such as stirred suspension and hollow fiber bioreactors, are scalable platforms capable of providing a well-controlled environment for MSCs to produce EVs. Conditions within such bioreactors can be adjusted to match the *in vivo* microenvironment and optimize production. However, there is currently a huge gap in knowledge regarding how different culture parameters impact the secretion profile of MSCs. For example, the effects of large-scale production using microcarrier or spheroid culture on production rates and therapeutic efficiency of MSC-EVs are mostly unknown.

Preconditioning Strategies

Preconditioning strategies such as refining critical process parameters (temperature, pH, and dissolved oxygen levels) and using biochemical/physical cues can cause MSCs to secrete greater numbers of EVs with increased potency [2]. Further standardization is required between MSC-EV studies to reconcile observed deviations in trends and to increase reproducibility between studies.

Conclusions

A significant amount of work still remains in determining how to optimize the reproducible generation of clinically relevant quantities of MSC-EVs with defined functional attributes. Robust process development for large-scale manufacturing of high-quality therapeutic MSC-EVs will catalyze advancements of these products toward clinical applications.

References [1] Pittenger, M. F. et al., *npj Regen. Med.* **4**, 22. (2019). [2] Phelps, J. et al., *Stem Cells Int.* **2018**, 9415367 (2018). [3] Katsuda, T. et al., *Proteomics* **13**, 1637-1653 (2013).

OpenFOAM Multiphysics Simulation Comparison to Commercial Software for Electrokinetic Fluid Flow of Conductive Biofluids in Microchannels

S. Cenaiko[1,2], T. Lijnse[3], C. Dalton[3,4]
[1]Chemical and Petroleum Engineering Department, [2]Centre for Bioengineering Research and Education, [3]Biomedical Engineering Graduate Program, [4]Electrical and Computer Engineering Department, University of Calgary

Introduction

Point-of-care (POC) medicine has the ability to reduce response times, and lower the sample sizes, amounts of reagents and power required to run lab tests. The current mechanical micropumps used in these devices can be difficult to miniaturize and risk damage to particulates in certain biofluids. The AC electrothermal (ACET) technique is well suited for manipulating high conductivity fluids (>0.1S/m), including biofluids such as blood, urine, and tears, without the use of moving parts. Using low voltages ($<10V_{peak}$) to mitigate the risk of damage to biofluids, the ACET approach involves generating microvortices through convection to induce fluid pumping and/or mixing [1]. Simulations provide an effective way of optimizing and testing new ideas without spending the resources (time, money, materials, etc.) to make and test a device. This research explores methods to simulate ACET using OpenFOAM, an open-access software coded in C++, which allows users complete control over solution methods. Results are then compared to a commercial multiphysics software package (COMSOL Inc. MA, USA), which comes with embedded algorithms to solve a computer-generated set of equations. Recently, OpenFOAM has been used to simulate ACET in a few papers to test various geometries, but these results have not been experimentally verified [2]. The aim of this work is to determine the feasibility of a more cost effective and transparent method of simulating ACET.

Methods

A standard 2D geometry for a rectangular ACET microchannel was developed in OpenFOAM, with one array of microelectrodes along the bottom of the channel and a layer of substrate forming the top of the channel. The microelectrode geometry comprised a repeating unit of a large electrode at ground potential and small electrode at 7V to create a non-uniform electric field in the fluid. A solver was developed in OpenFOAM from adapting the pre-existing solver; equations for the electric field, joule heating, and ACET force were then added to the solver.

Results

Temperature profiles in OpenFOAM and COMSOL demonstrate a high semblance, with maximum temperatures reaching 313.67K and 313.59K, respectively. However, as shown in Figure 1, flow profiles show significant discrepancies, with the outlet flow rate being 34% lower in OpenFOAM than in COMSOL. COMSOL simulations of ACET have been reported extensively in the literature and experimentally verified [1]. The initial work presented here indicates more investigation and validation is required before OpenFOAM can be reliably used for ACET simulations.

Conclusions

Preliminary results demonstrate the limitations of this free software for simulating ACET flow. Issues were also found with generating an accurate geometry, slow or diverging solutions, and inconsistent results.

References

[1] Salari, A. et al., *Micromachines*, 2019.[2] Shojaei, A. et al., *Int. J. Mechanical Sci.*, 2019.

Figures

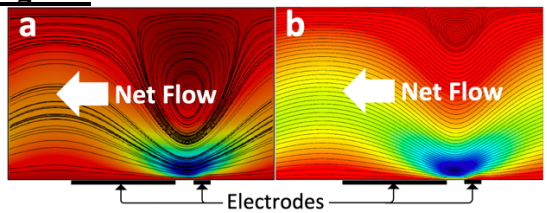

Figure 1: Flow profiles generated by a) OpenFOAM and b) COMSOL simulations for identical geometries. Figures are shown with similar colour scales, allowing for a direct comparison of results.

Evaluating the role of white matter development in literacy and mental health.

Kassondra Pedenko, Bryce Geeraert, Catherine Lebel.

Introduction

A growing body of literature has suggested that children with literacy problems are at an elevated risk for mental health disorders[1-3]. No study to date has investigated differences in white matter microstructure as a potential explanation for why we see this comorbidity. By virtue of the geographic placement and structural connectivity of the extreme capsule (EmC) and the uncinate fasciculus (UF), these tracts have the potential to play a prominent role in the language network and in aspects of mental health. This study will determine if baseline features of the bilateral EmC and bilateral UF predict later reading skills and/or internalizing behaviours in a typically developing population using diffusion tensor imaging (DTI). We hypothesize that alterations in white matter microstructure will be correlated with reading measures in a typically developing adolescent population and that these alterations will be indicative of mental health symptoms, such that better reading scores will be predictive of better internalizing behaviour scores longitudinally.

Methods

52 typically developing children and adolescents (10.30±2.35y, 27M/25F) were scanned using a GE 3 T Discovery MR750w (GE, Milwaukee, WI) system at the Alberta Children's Hospital. 33 (12.76±2.38y, 17M/16F) have returned for 2-year longitudinal scanning and assessment, and 10 (14.67±1.78y, 4M/6F) have returned for 4-year longitudinal scanning and assessment. DTI images were imported into ExploreDTI[4] for standard pre-processing. DTI-based probabilistic tractography of the bilateral EmC and the bilateral UF was performed using inclusion and exclusion masks based on coordinates from prior anatomical studies[5-10]. Measures of white matter microstructure, including fractional anisotropy (FA), and mean diffusivity (MD), were calculated for each subject using the Descriptive Statistics tool in ExploreDTI[4]. Internalizing mental health symptoms were assessed using the Behavioral Assessment System for Children, 2nd Edition Parent Rating Scale (BASC-2-PRS)[11]. Children's reading comprehension and fluency was assessed using the Wechsler Individual Achievement Test 3rd Edition (WIAT-III)[12]. Statistical analysis will be conducted in R version 3.4.1[13]. Measure means will be computed for the bilateral EmC and bilateral UF, and change scores will be computed between time points for each participant. Structural change scores will be correlated with age using Pearson correlations. If either tract has a significant correlation, partial least squares regression will be used to elaborate this relationship.

Results

Analysis is currently ongoing. We anticipate that alterations in white matter microstructure in the EmC and the UF will be correlated with WIAT-III measures in a typically developing population, revealing higher FA and lower MD in children and adolescents with better reading comprehension and fluency scores. Additionally, alterations in white matter integrity that correlate with WIAT-III scores will be predictive of mental health symptoms, such that better reading scores yield lower mental health scores on the BASC-2-PRS.

Conclusions

Understanding the trajectory of typical white matter microstructure development in the EmC and UF will elucidate the roles of these tracts, providing a foundation for future studies of white matter development in both typical and atypical populations.

References

1. Boyes et al. *Dyslexia*, 2016. 22(3); 263-66. **2.** Carroll et al. *J Child Psychol Psychiatry,* 2005. 46; 524-32. **3.** Maughan et al. *Curr Opin Psychiatry,* 2006. 19; 350-55. **4.** Leemans et al. *Proc Intl Soc Mag Reson Med,* 2009. **5.** Ariëns-Kappers et al. The comparative anatomy of the nervous system of vertebrates including man, MacMillan, 1936. **6.** Crosby et al. Comparative correlative neuroanatomy of the vertebrate telencephalon, MacMillan, 1982. **7.** Frey et al. *J Neurosci*, 2008. 28(45): 11435-44. **8.** Makris et al. *Ann Neurol,* 1997. 42(6): 951-62. **9.** Makris et al. *Brain Struct Funct,* 2009. 213: 343-58. **10.** Mars et al. *Brain Struct Funct,* 2016. 221; 4059-71. **11.** Reynolds et al. Encyclopedia of clinical neuropsychology, Springer, 2011. **12.** Vaughan-Jensen et al. *J Psychoeduc Assess*, 2011. 29(3): 286-91. **13.** Urbanek et al. *R Foundation,* 2017.

Identifying auditory artifacts in small rodent focused ultrasound neuromodulation

Jake Hesselink, Chris Krasnichuk, Amine Benaceur, Zelma Kiss, Samuel Pichardo

Introduction

Neuromodulation has proven a powerful technique in the treatment of various neurological disorders. However, current methods suffer from certain drawbacks. Deep brain stimulation involves invasive surgery, while transcranial magnetic stimulation offers little ability to target deep-brain areas accurately. Focused ultrasound (FUS) neuromodulation offers a spatially specific, non-invasive neurostimulation technique. Current studies in mice often record motor response to FUS neurostimulation. The fidelity of such motor responses was called into question by a study that found FUS caused widespread auditory activation within the cortex that may underly the motor responses[1]. Here, we hypothesize that FUS stimulation causes vibrations in the skull within the audible range of the animal and, accordingly, motor activity will be seen in response to FUS stimulation of both the motor and visual cortices.

Methods

To test this, 477 kHz ultrasound, with a pulse repetition frequency (PRF) of 1.5 kHz and a spatial-peak temporal average intensity of 4.2 W/cm^2, was sent to visual cortex or motor cortex targets of C57BL/6 mice, using a stereotactic-guided ultrasound device from FUS Instruments [RK-50]. Motor responses to each stimulation were recorded with video and with electromyography (EMG), while vibrations in the skull were recorded using a small contact microphone.

Results

As hypothesized, distinct motor responses to both targets were captured on EMG and video, with no significant difference in response rate between them. Clear audio signals containing 1.5, 3.0, and 4.5 kHz frequencies were seen in 9 of 15 animals, though the presence of this signal had no effect on response rates.

Conclusions

This auditory artifact provides evidence for a possible mechanism of indirect auditory activation. Though motor responses were seen, their inconsistency calls for further investigation into the mechanism underlying FUS motor stimulation.

References

Sato T., Shapiro M. G., Tsao D. Y. (2018). Ultrasound neuromodulation causes widespread cortical activation via an indirect auditory mechanism. *Neuron*. 98: 1031-1041.

Deep Learning to Improve the Diagnostic Potential of Low-dose CT

Kevin J. Chung,[1,2] Roberto Souza,[3,4] Richard Frayne,[3,4] Ting-Yim Lee[1,2]
[1]Department of Medical Biophysics, University of Western Ontario, London, Ontario
[2]Lawson Health Research Institute and Robarts Research Institute, London, Ontario
[3]Department of Radiology and Clinical Neuroscience, University of Calgary, Calgary, Alberta
[4]Seaman Family MR Research Centre, Foothills Medical Centre, Calgary, Alberta

Introduction

Radiation dose reduction in CT is highly desirable to reduce carcinogenic risks associated with diagnostic examinations. Low-dose CT can be achieved by reducing x-ray tube voltage or current-exposure time product but results in noisy images with poor diagnostic image quality. Deep learning has demonstrated exceptional performance in reducing low-dose CT noise when trained with sufficient high-quality data [1]. Here, we propose a low-dose CT image denoising strategy that uses convolutional neural networks (CNNs) to filter noise in the spatial frequency domain and in the image domain. We hypothesize that these denoised images will be visually and quantitatively comparable to corresponding routine-dose CT images.

Methods

Images were from the AAPM Low-dose CT Grand Challenge [2], which comprised of paired sets of quarter- and routine-dose contrast-enhanced CT images of the abdomen from 10 patients. Five patients were reserved for training (4,748 images), two for validation (1,193 images), and the remaining three for testing (2,373 images). A CNN called the U-net [3] was used to process the 2D Fourier Transform of a low-dose CT image, which filters the image's spatial frequency spectrum. This output was then transformed back to the image domain by a 2D inverse Fourier Transform before being additionally processed by another U-net to produce the final denoised image. The network was trained over 30 epochs with a batch size of 4 and real-time data augmentation to simulate additional training data from existing training images to reduce model overfitting. The loss function was a weighted sum of mean absolute error and multi-scale structural similarity, which is an index of the perceptual resemblance between the processed low-dose and routine-dose CT images.

Results

The proposed deep learning network was able to substantially reduce noise and improve the contrast-to-noise ratio of low-dose CT images. Contrast-enhanced blood vessels in the liver were clearly distinguishable from surrounding tissue in the processed low-dose images whereas noise impeded their visibility in the unprocessed images. Compared to the unprocessed images, the denoised images had improved mean ± standard deviation peak signal-to-noise ratio and structural similarity to corresponding routine-dose images: 38.6±3.1 dB versus 43.4±2.7 dB and 0.90±0.05 versus 0.96±0.02, respectively.

Conclusions

Low-dose CT images processed by our proposed network demonstrated substantial improvement in qualitative and quantitative fidelity over unprocessed images when compared to the routine-dose reference. Important anatomical features for diagnostic accuracy were preserved albeit with some additional smoothing, which resulted in changes to noise texture in the processed images. Further validation of our proposed technique is warranted by comparing diagnoses made on the denoised low-dose images with their corresponding routine-dose references in a large dataset of patients.

References

[1] Wang et al. *IEEE Trans. Med. Imaging.* 2018; 37(6): 1289–1296.
[2] McCollough et al. *Med Phys.* 2017; 44(10): e339–e352
[3] Ronneberger et al. *Springer LNCS.* 2015; 9351: 234–241.

Monitoring Breast Treatment with Microwaves: Consistency of Scans of the Healthy Breast

P. Sharleen (1), K. Smith (2), M. Lesiuk (3), S. Quirk (4), M. Roumeliotis (4), P. Grendarova (3), E. Fear (1)
(1)Electrical and Computer Engineering, (2) Biomedical Engineering Graduate Program, University of Calgary, (3) Radiation Oncology, Alberta Health Services (4)Medical Physics, Tom Baker Cancer Centre Authors

Introduction

Introduction There is a potential for microwave imaging to provide feedback on the progress of cancer treatment since the images can show tissue changes over time. Compared to clinical imaging, microwave images map the dielectric permittivity of tissues which is attributed to tissue water content. For instance, fatty tissue has lower permittivity than higher water content tissues such as gland and tumour. The purpose of this study was to evaluate the effectiveness of our microwave imaging prototype in processing real patient signal data.

Methods

16 Participants were recruited from those enrolled in the ACCEL (Accelerated Partial Breast Irradiation) clinical trial. Breast scans were taken before radiotherapy and at 6-week and 1-year follow-up for both the treated and healthy breasts. This study was approved by the Health Research Ethics Board of Alberta (HREBA.CC-17-0322). The inclusion criteria included being a female, aged 50 and older at diagnosis of invasive or in-situ ductal carcinoma with primary tumour diameter of 3 cm or less and having been treated with breast conserving surgery. Scan signals were collected in the frequency range of 100MHz to 10 GHz using a transmission system consisting 2 arrays of 5 UWB (ultrawideband) antennas each [1]. The data are then transformed to the time domain, and a time delay spectroscopy technique is used to estimate permittivity between each sensor pair. Then, the average permittivities are mapped to form a 2D image.

Results

There exists striking consistency between the scans taken at different time points for the healthy breast of most patients. Figure 1 shows the images generated for Baseline, 6-week and 1-year healthy breast scans for one patient as an example with mean relative permittivity values 12.25, 11.26, and 10.80 respectively. This consistency can be demonstrated with 4 other patients.

Conclusions

The percent difference calculated for 5 patients stayed in the range of 0.5 % to 11%. These differences between Baseline and follow-up images might be due to breast placements not being identical between scans.

Preliminary results were promising because they demonstrate consistency of the transmission system over a 1-year timeframe. This expected consistency in images for the untreated (healthy) breast gives an encouraging outlook for the next step of this study, which is analyzing the treated breast data.

References

[1] J. Bourqui and E. C. Fear, "System for Bulk Dielectric Permittivity Estimation of Breast Tissues at Microwave Frequencies," in *IEEE Transactions on Microwave Theory and Techniques*, vol. 64, no. 9, pp. 3001-3009, Sept. 2016, doi: 10.1109/TMTT.2016.2586486.

Figures

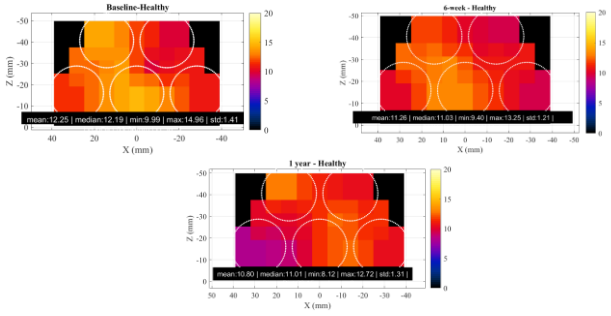

Figure 1: Comparison of plotted images of Healthy Breast for patient A.

Localized Mild Hyperthermia Using MRI Guided High Intensity Focused Ultrasound in Tumour-Bearing Mice for Potential Cancer Therapies

M. Siddiqui[1], D. Senger[1], N. Dang[1], J. King[1], J. Rahn[1], T. Foniok[1], D. Rushforth[1], S. Robbins[1], W. Foltz[2], K. Piorkowska[3], M. Dunne[4], A. C. Waspe[3], C. Allen[4], S. Pichardo[1]
[1] University of Calgary, Calgary, Alberta, CANADA, [2] Princess Margaret Cancer Centre, Toronto, Ontario, CANADA [3] The Hospital for Sick Children, Toronto, Ontario, CANADA, [4] University of Toronto, Toronto, Ontario, CANADA

Introduction

Alveolar soft part sarcoma (ASPS) is a rare type of soft tissue sarcoma[1]. MRI guided Focused Ultrasound (MR-FUS) concentrates mechanical energy in a small volume of tissue and can induce localized hyperthermia (temperature is raised to about 42-43°C for a prolonged period)[2]. MRI allows monitoring of temperature changes non-invasively and in real-time[2]. Doxorubicin is a cancer drug and its temperature-sensitive liposome-encapsulated form, (ThermoDXR), only releases its contents at temperatures greater than 41.5°C. Combining the induction of MR-FUS-based localized hyperthermia with the administration of ThermoDXR can enhance targeted drug delivery to ASPS tumours as drug is only released at the tumour site, and healthy tissue are protected from drug toxicity.

Methods

We conducted a study in tumour-bearing mice (CB17 SCID), injected with ASPS cells from a human cell line (SM3762), subcutaneously in the flank. Mice were divided into one of four groups: hyperthermia + encapsulated drug, hyperthermia + free drug, free drug alone, and encapsulated drug alone. We induced hyperthermia in the tumour (42.5°C for 10 minutes) using a small-animal MR-FUS device (IGT, Bordeaux, France) with a transducer operating at 2.5MHz. Treatment planning and thermal therapy were conducted in our in-house software, Proteus. We collected FLASH images throughout the procedure plus 3 minutes post-heating and T2 weighted images pre and post-treatment to check for damage. When the temperature stabilized at 42.5°C, we infused drug (dose: 5mg/kg) through the tail vein. Post-treatment, we euthanized the mice, performed blood perfusion and resected the tumour and major organs and froze them at —80°C. Drug was extracted from tissue by tissue homogenization in acidified ethanol followed by centrifugation. Concentration was calculated by measuring doxorubicin fluorescence in the supernatant using a benchtop fluorometer with 480nm excitation and 590nm emission filters and relative fluorescence intensities were scaled to doxorubicin concentrations using a standard doxorubicin calibration curve.

Results

9 out of 12 mice had controlled heating in the focal region and 5 out of 12 mice were heated with no damage. Drug concentration was highest in the hyperthermia + encapsulated drug group (1.7, 1.4 and 2.9 times higher than the hyperthermia + free drug, free drug alone, and encapsulated drug alone groups, respectively).

Conclusions

Hyperthermia can be established in precise locations in the body using MR-FUS in a non-invasive manner, however, tumour position must be carefully planned to avoid damage. Coupling localized hyperthermia with chemotherapy using temperature-sensitive drug-carriers improves drug delivery to ASPS tumours in mice.

References

[1] Stein-Wexler R. Pediatric soft tissue sarcomas. *Semin Ultrasound, CT MRI*. 2011. doi:10.1053/j.sult.2011.03.006
[2] Chung AH, Jolesz FA, Hynynen K. Thermal dosimetry of a focused ultrasound beam in vivo by magnetic resonance imaging. *Med Phys.* 1999. doi:10.1118/1.598707

Microwave Imaging for Radiation Treatment Monitoring: Strategies for Incorporating Clinical Data

K. Smith[1], J. Bourqui[2], M. Lesuik[3], S. Quirk[3], M. Roumeliotis[3,] and E. Fear[2]
[1]Biomedical Engineering Graduate Program, University of Calgary, [2]Department of Electrical and Computer Engineering, University of Calgary, [3]Department of Oncology, University of Calgary

Introduction

Breast tissue responds to radiation treatment with varying side effects depending on the patient, the radiation dosage, and the treated volume. To better understand these side effects, microwave imaging is proposed for monitoring changes in the breast. However, how features in microwave images relate to changes in the breast due to treatment has not been established. In this study, strategies for using clinical data to complement our interpretation of microwave images, and the challenges of doing so, are explored. In this study design abstract, we propose an image registration approach between CT scans mammograms, and microwave images to approximate the location of the treated volume in our microwave images, known as MITS images [1].

Methods

MITS images from 16 patients before and after radiation therapy have been collected along with the nipple location with respect to each image (HREBA.CC-17-0322). For each patient we have also accessed mammograms and CT scans showing the tumour location and the treated volume respectively. We will estimate the treated volume in the MITS images using two steps. The first step is aligning MITS images with mammogram images. The registration algorithm will be developed using breast phantoms of known geometry. The MITS and mammogram phantom images will be aligned using a variety of landmarks starting from the entire breast outline, to only the nipple location. The finished algorithm will be applied to the patient images using the nipple location for alignment. The second step is estimating the treated volume shown in a 3D CT scan taken while the patient is laying on her back, onto the 2D mammogram, taken while the patient is upright. This will be done projecting the volume onto the 2D plane of the mammogram. Then, the location of the treated area can be approximated over the tumour location in the mammogram.

Expect Results

The expected visual result of our two-step registration is illustrated in Figure 1. However, the reliability of this registration is limited by the small number of landmarks available in MITs images, and the approximation between varying orientations in the CT and mammogram. Our phantom scans will help infer the expected accuracy. Dependent on this accuracy, we expect to see larger responses in MITS images which contain a larger area of the treated volume.

Conclusion

This abstract proposes a registration strategy to incorporate mammogram and CT images with microwave images, for the application of radiation treatment monitoring.

References

[1] J. Bourqui and E. C. Fear, "System for Bulk Dielectric Permittivity Estimation of Breast Tissues at Microwave Frequencies," *IEEE Transactions on Microwave Theory and Techniques,* vol. 64, no. 9, pp. 3001-3009, 2016

Figure

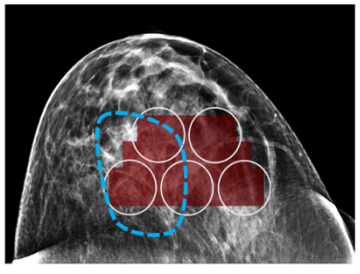

Figure 1: The registration of a MITS image (red) and treated volume (blue) onto the patient mammogram

Precision Mapping of Functional Brain Networks in Children

Shefali Rai, Kirk Graff, Ryann Tansey, Kate Godfrey, Dr. Carly McMorris, Dr. Ashley Harris, Dr. Signe Bray
University of Calgary, Cumming School of Medicine

Introduction

fMRI studies provide information on functional brain organization[1]. Recent work has shown individualistic brain network features that are different from the group-level functional networks typically shown in fMRI studies. Averaging group-level brain network tendencies conceals unique patterns in individual brains[2]. Hence, focusing on individual-centric fMRI studies, researchers have found that idiosyncratic brain network features in adults are stable and may be related to differences in behavior[3]. However, most of these novel individual-centric studies concentrate on adult populations. Given that the brain changes rapidly across childhood and that child brains greatly differ in organization and connectivity from adult brains[4], precisely mapping child functional brain networks is an unexplored yet critical area of research.

Methods

This study will recruit 30 typically developing children (15 males and 15 females) aged 7 years old, with no history of mental health conditions, brain injuries, and/or chronic health conditions. Each participant will undergo an fMRI scan at the same time each week for four weeks. Each scan will be comprised of three 6-minute passive-viewing fMRI scans totally 18 minutes, for a total scan time of 72 minutes of fMRI data per child. It has been shown that longer scan times are needed to robustly provide precise measurements of functional networks[5]. Therefore, with 72 minutes of data per child, this study can truly tease apart network variations in individual child brains.

Results

Preliminary results conducted on a young adult during a passive viewing fMRI scan reveals that a robust measurement of brain networks can be achieved with longer scan times (Preliminary Figure 1). At roughly 27 minutes of scan duration, functional connectomes stabilize and approach a test-retest of r=0.85.

Conclusions

For this study, densely sampling individual children with repeated neuroimaging scans will show individually unique and stable network features. Currently the field has been hindered by our inability to precisely track changes in brain networks as children develop. This study will be an exciting first step towards understanding the functional relevance of network individualization in children.

References

1.Power, J. D., Cohen, A. L., Nelson, S. M., Wig, G. S., Barnes, K. A., Church, J. A., et al. (2011). Functional network organization of the human brain. Neuron, 72(4), 665– 678.
2.Gordon, E. M., Laumann, T. O., Gilmore, A. W., Newbold, D. J., Greene, D. J., Berg, J. J., et al. (2017). Precision Functional Mapping of Individual Human Brains. Neuron, 95(4), 791-807.e7.
3. Seitzman, B. A., Gratton, G., Laumann, T.O., et al. (2019). Trait-like variants in human functional brain networks. PNAS, 116(45), 22851-22861.
4.Supekar, K., Musen, M., & Menon, V. (2009). Development of large-scale functional brain networks in children. PLoS Biology, 7(7), e1000157.
5. Laumann, T. O., Gordon, E. M., Adeyemo, B., et al. (2015). Functional System and Areal Organization of a Highly Sample Individual Human Brain. Neuron, 87(3):657-70.

Figures

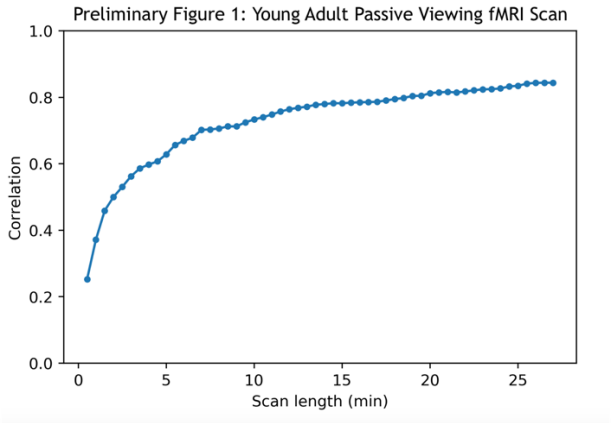

3-Dimensional Geometric Trends of Coronal Sutures

Ross Remesz[1], Tsolmonbaatar Khurelbaatar[1], Michael R Doschak[2,3], Dan L Romanyk[1,3],
[1]Department of Mechanical Engineering; [2]Faculty of Pharmacy and Pharmaceutical Sciences; [3]School of Dentistry, University of Alberta

Introduction

Cranial sutures are the soft connective tissue that join skull bones and allow for cranial growth and development. Cranial sutures are primarily a complex network of collagen fibers, extracellular matrix, and vasculature [1], and are geometrically serpentine in nature [2]. Linear interdigitation index (LII) is defined as the path length of a suture divided by the linear length between the two endpoints of interest. LII is a parameter that is commonly used to link geometric characteristics of sutures to mechanical performance [3]. This method takes a single 2D planar slice of suture and uses it to characterize the suture geometry. Analyzing LII through the skull thickness gives a better understanding of suture geometry in 3D and challenges the method of 2D suture characterization. The focus of this research was to show the 3D geometric trends of cranial sutures. The trends found will aid in modeling an accurate geometric representation of cranial sutures in future mechanical simulations.

Methods

Two swine cranial suture samples were obtained from collaborators at the University of Washington. All procedures concerning animal ethics were approved by University of Washington Animal Care and Use Committee (Protocol# 2331-21). Samples were scanned with micro-CT at 8.9 μm resolution utilizing a Skyscan 1076 micro-CT (Bruker-SkyScan, Kontich, Belgium). Eleven evenly spaced slices at 10% increments through the skull thickness were selected for analysis. Micro-CT images were uploaded to MATLAB where processing and segmentation was performed. The segmentation was done manually with measures taken to ensure consistency between slices. The segmented images were run through a MATLAB script that utilized a marching method to navigate through the suture path and obtain the pathlength at each plane through the bone thickness.

Results

The highly interdigitated coronal sutures LII increased significantly near the inner surface of the skull. A visualization of suture path through sample thickness is shown in Fig. 1. The LII was found to range from 1.6 to 4.4 in a single bone sample throughout its thickness.

Conclusions

Findings from this work have shown that the geometry of a highly interdigitated cranial sutures cannot be accurately approximated with a 2D measure. The 3D trends found in this study will be implemented in generating geometries for finite element models in future work studying suture mechanical response to applied loading.

References

[1] Herring SW. *Front Oral Biol*. 2008.
[2] Savoldi F et al. *Sci Reports*. 2018.
[3] Jaslow CR. Journal of Biomechanics. 1990.

Figures

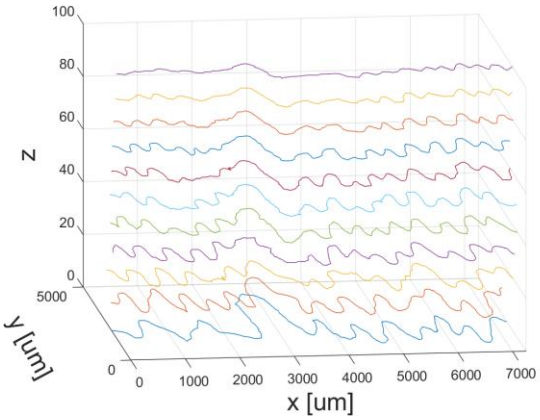

Fig. 1: Center paths of a coronal suture through the thickness of a swine skull sample. The z-axis represents different planes through the thickness of the skull 0% is the inner skull, and 100% the outer skull. the x-axis is the suture direction, and y-axis shows transverse suture movement.

Estimating thickness and speed of sound of layered material using a low-frequency imaging linear-array

Shirshak Shrestha[1], Laura Curiel[2], Samuel Pichardo[3]
[1]Department of Biomedical Engineering, University of Calgary
[2]Department of Electrical Engineering, University of Calgary
[3]Departments of Radiology and Clinical Neurosciences, University of Calgary

Introduction

Low-Intensity Focused (LIFU) involves ultrasonic waves passing through the skull, a secondary medium, resulting in potential defocusing due to the refraction which can be mitigated using computed tomography (CT) and numerical simulations [1], [2]. Here we present a new method to estimate the acoustic properties of human skulls using a low-frequency linear array which will facilitate development of refocusing algorithms to mitigate the problem of defocusing with no radiation exposure and in real-time.

Methods

We applied a variable focusing method [3], [4] to locate the inner edge of the skull where echo signal is at its maximum. The ultrasound time of flight between the two edges, ultrasound focus, and the distance of the skull from the transducer, obtained from the echo signal with focus at the inner edge of the skull, were used to estimate the skull thickness and speed of sound. We implemented this method using a 32-element 1 MHz linear array transducer and a Verasonics vantage system. We performed tests with polycarbonate (PC) and high-density polyethylene (HDPE) and a skull phantom. We also measured the thickness using a caliper and the speed of sound using the time-difference measured with a hydrophone between water-only and the phantom materials.

Results

Estimated thickness of the PC and HDPE was 6.49 mm and 6.38 mm, respectively, compared to 6.4 mm measured with a caliper. The speed of sound was 2260 m/s and 2429 m/s, respectively, compared to 2186 m/s and 2347 m/s measured with a hydrophone. For the skull phantom, the new method estimated a thickness of 10.56 mm and a speed of sound of 2112 m/s, with reference values of 8.8 mm ± 0.625 mm and 2467 m/s, respectively.

Conclusion

The new non-invasive method can estimate individual acoustic properties for aberration correction with no exposure to radiation and in real-time.

References

[1] W. Legon, L. Ai, P. Bansal, and J. K. Mueller, "Neuromodulation with single-element transcranial focused ultrasound in human thalamus," *Hum. Brain Mapp.*, vol. 39, no. 5, pp. 1995–2006, 2018.

[2] S. Almquist, D. L. Parker, and D. A. Christensen, "Rapid full-wave phase aberration correction method for transcranial high-intensity focused ultrasound therapies," *J. Ther. Ultrasound*, vol. 4, no. 1, 2016.

[3] V. Hänel, "Measurement of sound velocity and thickness of thin samples by time-resolved acoustic microscopy," *J. Appl. Phys.*, vol. 84, no. 2, pp. 668–670, 1998.

[4] A. Wydra, E. Malyarenko, K. Shapoori, and R. G. Maev, "Development of a practical ultrasonic approach for simultaneous measurement of the thickness and the sound speed in human skull bones: A laboratory phantom study," *Phys. Med. Biol.*, vol. 58, no. 4, pp. 1083–1102, 2013.

Use of Functional Near-Infrared Spectroscopy (fNIRS) Coherence to Analyse the Effect of Task Execution in the Frontal and Motor Cortices

Sabrina Pearce[1,2], Joel Burma[3], Ibukun Oni[4], Jeff F Dunn[1,4,5]
[1]Neuroscience Graduate Program, University of Calgary, [2]Brain CREATE Neuroscience Program, University of Calgary, [3]Kinesiology Graduate Program, University of Calgary, [4]Biomedical Engineering Program, University of Calgary, [5]Dept. of Radiology, Cumming School of Medicine, University of Calgary

Introduction

Mild traumatic brain injury (mTBI) is a public health problem and is of particular concern in adolescent populations due to its high prevalence and the tendency for this age group to experience more severe outcomes[1]. Currently, no accepted clinical imaging protocol exists to detect or monitor mTBI. Such a protocol would be useful in guiding return-to-activity and for studying the impact of treatments on outcome. Functional near-infrared spectroscopy (fNIRS), which assesses brain activity through measures of oxygenated and deoxygenated hemoglobin, offers a portable and relatively inexpensive solution. Regions that display similar oscillation frequencies in hemoglobin oxygenation are characterized as functionally connected. We quantify this using coherence analysis. Research from our group has shown that fNIRS coherence decreases in mTBI populations[2,3].
The specific task used during coherence measurements may impact the results of an mTBI assessment. In this study we determine if coherence changes with task in a healthy population.

Methods

Community controls, with no mTBI in the last 6 months and no current symptoms were used. fNIRS was measured using the NIRx NIRScout using a 32-channel setup. Participants completed a task paradigm which included a resting state, visual working memory task, a Stroop task, a shifting attention task, 2 back, and motor finger tapping task. Coherence was analysed using in house software in dorsolateral prefrontal and motor cortices. Post processing will compare measures of coherence between resting and task states, to determine which tasks elicit the greatest change in average coherence.

Results

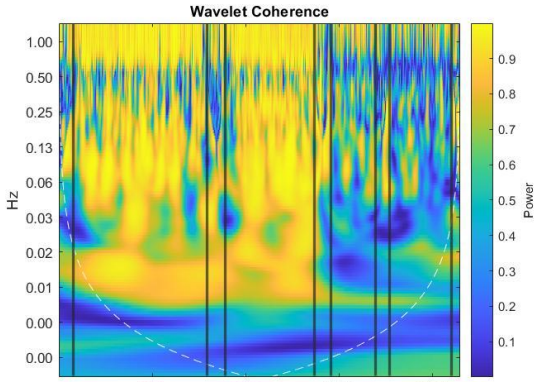

Figure 1: Wavelet coherence model analysing the coherence between the left and right frontal cortices over an fNIRS recording timecourse

A wavelet coherence analysis will occur over 0.04 to 0.1 Hz; commonly associated with neural signals[4], the wavelet model from a participant performing the task paradigm is shown.

Conclusions

fNIRS has the potential to provide a biomarker for predicting mTBI injury outcomes and assessing treatment. The results from this study will provide insight into effective cognitive and motor tasks that may be effective in monitoring functional connectivity in mTBI patients.

References

1. McKinlay et al (2008) *Brain Inj*
2. Urban et al. (2015). *J Neurotrauma*
3. Hocke et al (2018). *J Neurotrauma*
4. Bernjak, A., et al (2012) *World Scientific*

Breast Tissue Mimicking Phantoms for Combined Microwave and Ultrasound Imaging

Siyun Li[1], Elise Fear[1], Laura Curiel[1]
Department of Electrical and Computer Engineering, University of Calgary

Introduction

Microwave and ultrasound imaging have become standard methods for breast cancer diagnosis. Using a combination of those modalities can provide high-resolution images with improved contrast. In this work, we present a multi-layer breast tissue phantom that satisfies both microwave and ultrasound imaging properties for experimental tests.

Methods

Breast tissues include skin, fat, fibroglandular (FGT) and tumor for which we obtained formulations that mimic permittivity, conductivity, ultrasound speed of sound and attenuation. All phantoms were based on agar at different concentrations to which we added varying percentages of glass beads and different materials to modify microwave properties (canola oil, coconut oil, and polyvinylpyrrolidone - PVP). We ran an experiment with oil/PVP, agar and glass beads concentration as the three variables at three different concentrations each. We created 36 phantoms, and measured all properties, with 3 repetitions per phantom.

The microwave properties were measured by a vector network analyzer between 0 and 6 GHz. And the ultrasound properties were measured by a 7.5-MHz signal through the sample and measuring the pressure with a 0.5-mm needle hydrophone. The interactions among variables were evaluated using a 3-way analysis. We obtained the final recipes based on the linear relationship to match the reported values for breast tissues.

Results

Canola oil and agar affected permittivity and attenuation. Coconut oil influenced all properties, but agar only affected the attenuation. PVP modified the permittivity and attenuation, but the agar concentration did not affect these properties. The glass beads affected the attenuation for coconut oil and PVP cases. All variables change the speed of sound.

The final recipe to mimic fat was 75% Canola oil, 2.5% agar and 2% glass beads. 20% Coconut oil with 5.8% agar, 2% glass beads was used to mimic skin. For tumor 7% PVP, 2.5% agar, 9.6% glass beads; for FGT 14.7% PVP, 2.5% agar, 11.2% glass beads was used. The actual properties are shown in Table 1.

Table 1. Actual Properties Values for the Final Recipe

Tissue	*Relative Permittivity ε_r at 5 GHz*	*Effective Conductivity σ at 5 GHz*	*Attenuation (dB/cm·MHz)*	*Speed of Sound (m/s)*
Skin[1]	*30.54 ± 3.51*	*2.74 ± 0.25*	*4.20 ± 0.53*	*1487.5 ± 4.65*
Fat[2]	*7.49 ± 1.33*	*0.42 ± 0.10*	*1.44 ± 0.22*	*1477.4 ± 2.17*
FGT[3]	*52.03 ± 1.35*	*5.27 ± 0.26*	*0.64 ± 0.05*	*1555.4 ± 10.41*
Tumour[4]	*59.33 ± 1.09*	*5.30 ± 0.16*	*0.59 ± 0.18*	*1535.4 ±*

Reported values for skin, ε = 35, σ = 2.5, μ=2.4~4.5 dB/cm·MHz
Reported values for fat, ε = 5, σ = 0.2, μ<1 dB/cm·MHz, v=1420 m/s
Reported values for FGT, ε = 50, σ = 4.8
Reported values for tumor, ε = 55, σ = 5.2,v=1437~1547 m/s [1][2]

Conclusions

The phantoms reported in this abstract provide a method to make breast mimics to satisfy both microwave and ultrasound properties and meet the requirements of simultaneous ultrasound and microwave imaging.

References

[1] F. A. Duck, Physical Properties of Tissue. A Comprehensive Reference Book. 1990.

[2] J. Bourqui and E. C. Fear, "System for Bulk Dielectric Permittivity Estimation of Breast Tissues at Microwave Frequencies," *IEEE Trans. Microw. Theory Tech.*, vol. 64, no. 9, pp. 3001–3009, 2016,

Validating image texture analysis by assessing fresh postmortem MRIs from patients with multiple sclerosis

Zahra Hosseinpour, Olayinka Oladosu, Glen Pridham, Yunyan Zhang
Biomedical Engineering Program, Schulich School of Engineering, Department of Radiology and Clinical Neurosciences, Hotchkiss Brain Institute, University of Calgary

Introduction

Multiple sclerosis (MS) is a chronic immune-mediated disease of the central nervous system characterized by prominent demyelination, remyelination, and axonal injury (1). Magnetic resonance imaging (MRI) is the most widely used measurement method for MS pathology (2). However, subtle structural changes cannot be detected by conventional MRI. Texture analysis measures the distribution patterns of image pixels (3) and has demonstrated promise to define these small changes (4). The purpose of this study was to determine if and how MRI texture analysis is capable of measuring different patterns of tissue changes, including de- and re-myelination in lesions, using post-mortem MS brain samples, and to compare texture measures with 2 advanced MRI techniques: magnetization transfer ratio (MTR) and fractional anisotropy (FA) of diffusion tensor imaging (DTI).

Methods

We used MRI scans from fresh postmortem brains from 15 MS patients and 12 controls. We applied texture analysis for both T2-weighted MRI and DTI. The former used a Grey Level Co-occurrence Matrix (GLCM) method, with measures including angular second moment (ASM), entropy, contrast, correlation, dissimilarity, as well as entropy filter. Diffusion MRI texture calculation employed a new voxel-based approach, where we also enhanced the diffusion directions from 30 to 90 to improve angular resolution. We then used a random forest (RF) machine learning algorithm for tissue classification in brain gray and white matter (GM, WM), with classification accuracy assessed using Kappa statistics. Higher Kappa value represents more reliable accuracy (5). This was followed by recursive feature elimination (RFE) based on the RF to select the most predictive features. Then we applied two-way ANOVA with correction for multiple comparisons to detect tissue difference based on the importance features selected.

Results

In classifying WM tissue types of MS patients, we achieved high to perfect accuracy (kappa=0.76-0.94) based on all MRI features calculated, where T2-dissimilarity and T2-contrast were the most important features. According to ANOVA, T2-texture features were highly significant to differentiate various WM tissue types, and T2-contrast and T2-dissimilarity were the only features that distinguished demyelinated lesions from remyelinated ones. For patient GM tissue types, we had moderate classification accuracy (kappa=0.49-0.56). Feature ranking showed that T2-entropy filter, T2-dissimilarity, and T2-contrast were the most important features. In ANOVA analysis, all the T2- textures were significant in differentiating normal appear GM (NAGM) from GM lesions, and from remyelinated lesions in the GM. In classifying cortical lesions (4 types as per histology), we found moderate accuracy (kappa=0.42-0.6). Feature ranking revealed T2-correlation, T2-ASM, and T2-entropy filter being the most predictive features. In addition, ANOVA analysis showed that entropy and ASM of T2-weighted MRI differentiated the most pairs of GM lesion types. In classifying NAWM from normal WM in control, we had moderate accuracy (kappa=0.67). Feature ranking showed diffusion entropy and diffusion ASM to be the top predictive features. Based on ANOVA, diffusion entropy and diffusion ASM were highly significant to differentiate normal WM from NAWM. Finally, all top selected texture parameters were more significant than MTR and FA.

Conclusions

A number of texture features from both T2-weighted MRI and DTI have shown the potential to differentiate tissue types in GM and WM. Whereas, T2-Contrast and T2-dissimilarity were the only measurements that were significant for discriminating remyelinated from non-remyelinated lesions in WM. Diffusion texture measures were most important to classify normal WM from NAWM. All top selected texture features were more predictive than FA and MTR, indicating the utility of MRI texture analysis to characterize advanced tissue pathology in MS including myelin injury and repair.

References

1. Hemmer B, Nature Clinical Practice Neurology. 2006;2(4):201-11
2. Louapre C. Revue neurologique. 2018;174(6):391-7.
3. Zhang Y. International journal of biomedical imaging. 2012;2012.
4. Verma RK, BioMed research international. 2016;2016.
5. Landis JR, biometrics. 1977:159-74

Development of Micro Numerical Model of Distal Radius Fractures

Phillip Spanswick[1,4], Mohammad Salem[4], Danielle Whittier[1,4], Robert Korley[3], Steven Boyd[1,2,4], Prism Schneider[3,4]
[1]Biomedical Engineering Graduate Program, University of Calgary, Calgary, Canada
[2]Department of Radiology, Cumming School of Medicine, University of Calgary, Calgary, Canada
[3]Department of Surgery, Division of Orthopaedic Trauma, Cumming School of Medicine, University of Calgary, Calgary, Canada
[4]McCaig Institute for Bone and Joint Health, University of Calgary, Calgary, Canada

Introduction

The objective of our study is to develop a numerical model that is capable of accurately predicting the mechanical behaviors of distal radius fractures (DRFs), including the stiffness of the fractured wrist, throughout the fracture healing process. The performance of three finite element (FE) methods, two density based (continuum) methods and a homogeneous micro-FE (µFE) method, was evaluated. High-resolution peripheral quantitative computed tomography (HR-pQCT) images were used to generate continuum and homogeneous µFE models. Stiffness of the fractured wrist was compared to stiffness of the uninjured contralateral wrist to quantify the change in stiffness.

Methods

The three types of µFE models generated included a homogeneous µFE approach and two continuum µFE approaches (Figure 1). The homogeneous µFE models were generated from segmented images through the direct conversion of voxels to 8-node hexahedral elements [1]. A global threshold of 320 mgHA/cm3 was used to segment bone. The resulting bone elements were assigned linear elastic material properties, with a Young's modulus of E = 8748 MPa and a Poisson's ratio of v = 0.3 [2]. The two continuum µFE models were generated from the grey-scale HR-pQCT data using methods developed by Homminga et al. or Shefelbine et al. to define material properties [3, 4]. The Homminga and Shefelbine approaches relate densities to elastic moduli through an exponential and a piecewise linear relationship, respectively. All models were subjected to uniaxial compression and torsional loading. Models were solved using a custom FE solver (Faim v8.0, Numerics88 Solutions Ltd.).

Results

For uniaxial compression, an initial change in stiffness of -10%, -20%, and -54% is predicted by the Homminga, Shefelbine, and homogeneous µFE models, respectively. The results of continuum and homogeneous µFE models demonstrated 1% and 3% of recovery of stiffness per week respectively. The Homminga µFE approach did not capture significant longitudinal changes during the early follow-ups for either loading condition. The Shefelbine approach appears to be more sensitive to stages of fracture healing than the Homminga approach. The homogeneous µFE model illustrated a rapid recovery of stiffness.

Conclusions

Both the Shefelbine and homogeneous µFE approaches captured significant longitudinal changes in fracture stiffness. The homogeneous µFE method produced a rapid recovery of stiffness, suggesting it is more sensitive than continuum µFE approaches; therefore, it may better predict the mechanical characteristics of the injured wrist during fracture healing.

References

[1] J. MacNeil and S. Boyd, 2008, Bone, vol. 42, no. 6, pp. 1203-1213. [2] D. E. Whittier et al., 2018, J. Biomech, vol. 80, pp. 63-71. [3] S. J. Shefelbine et al., 2005, Bone, vol. 36, no. 3, pp. 480-8. [4] J. Homminga et al., 2001, J. Biomech, vol. 34, no. 4, pp. 513-517.

Figures

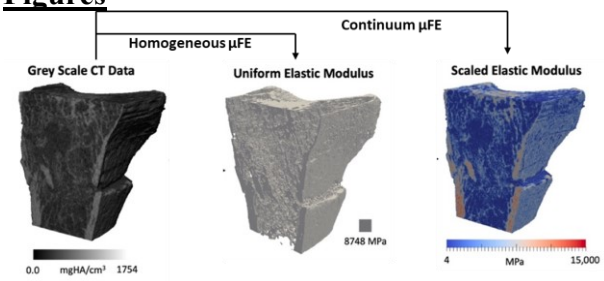

Figure 1. Flow chart illustrating the conversion from grey scale CT data to a homogeneous µFE and a scaled elastic modulus continuum µFE model (Homminga approach).

A Computer Vision Method for Dynamic Compliance Measurement in Ex Vivo Lung Perfusion

Jason Der[1], Katie Cameron[2], Steven Cruz Antunes[2], Calvin Jee[2], Reza Sabbagh[1], David S. Nobes[1]
[1]Department of Mechanical Engineering, University of Alberta, Edmonton, AB
[2]Tevosol, Edmonton, AB

Introduction

From multi-organ donors, only 15% of lungs are used for transplantation [1]. Ex-vivo lung perfusion (EVLP) is a preservation method that can improve the health of procured lungs such that discarded lungs are viable for transplantation [2][3]. A potential risk of EVLP mechanical ventilation is over-inflation of the lungs, which can be identified by measuring the elasticity of the lung as dynamic compliance [4]. Typically, dynamic compliance is calculated from tidal volume, indirectly measured from flow rate sensors. In comparison, structured light plethysmography (SLP) has been proven to obtain direct volume measurements in humans [5]. This paper explores how to adapt SLP for EVLP to monitor for over-inflation.

Methods

EVLP provides an unobstructed view of the lung during ventilation, allowing the use of a commercial stereo-vision camera system (Intel RealSense D435). From this system, 3D points are estimated that represent the surface of the lung. After the data is filtered, a surface mesh is generated, and the lung volume is computed as the space between the mesh and surface below the lung (see Figure1). Dynamic compliance is computed as the tidal volume divided by the change in transpulmonary pressure in negative pressure ventilation [6]. Also, properties can be measured over mesh elements, such as volume change. This workflow processes images from a camera stream, providing real time information to clinicians.

Results

As a benchmark, total volume and volume per mesh element have been calculated from videos of a moving plate, and respirating "lungs" modelled virtually (Rhino3D, Robert McNeel & Associates). Also, a preliminary optimization study, using design of experiments (DOE), was performed for image resolution and frame rate with images of virtually modelled objects. It is expected that this method will be able to measure dynamic compliance during EVLP.

Conclusions

So far, this method shows promise in replacing flow sensors for dynamic compliance estimation in EVLP systems. In the future, data will be collected from an operating EVLP machine, system parameters will be optimized using DOE, and additional computer vision measurements will be developed.

References

[1] M. Cypel *et al.*, *N. Engl. J. Med.*, vol. 364, no. 15, pp. 1431–1440, 2011.
[2] L. J. Lautner *et al.*, *Cryobiology*, vol. 94, no. April, pp. 1–8, 2020.
[3] M. Cypel *et al.*, *Am. J. Transplant.*, vol. 9, no. 10, pp. 2262–2269, 2009.
[4] K. Tsuno *et al.*, *J. Appl. Physiol.*, vol. 69, no. 3, pp. 956–961, 1990.
[5] W. H. De Boer *et al.*, *Br. Mach. Vis. Conf. BMVC 2010 - Proc.*, pp. 1–12, 2010.
[6] D. R. Hess, *Respir. Care*, vol. 59, no. 11, pp. 1773–1794, 2014

Figures

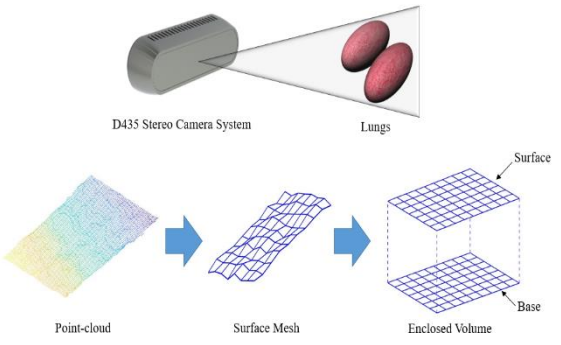

Figure 1 Depiction of D435 active stereo computer-vision system viewing lungs, and the data processing workflow.

Pressure and Energy Loss Analysis in Atrial Septal Defect

Safia Ihsan Ali, Fatemehsadat Jamalidinan, James White, Julio Garcia
Libin Cardiovascular Institute – Stephenson Cardiac Imaging Centre, Departments of Radiology and Cardiac Sciences, University of Calgary, Alberta, T2N 2T9

Introduction

An atrial septal defect (ASD) is a congenital heart defect (CHD) in which when the septum is defective or absent, the oxygen-rich blood can directly flow from the left side of the heart to mix with the oxygen-poor blood in the right side, or vice versa [1]. ASD complex flow patterns are difficult to assess using standard imaging techniques. 4D flow magnetic resonance imaging (MRI) is a novel technique that measures complex 3D blood flow patterns in-vivo and identifies altered cardiovascular hemodynamics [2,3]. This study aims to identify differences between aortic and pulmonary blood flow characteristics in healthy controls and ASD patients via blood flow volume, pressure drop, and energy loss. We hypothesize that pressure and energy loss are associated to altered hemodynamics in ASD patients.

Methods

A total of 20 ASD patients (age = 46.9 ± 16.1, female = 8) and 20 healthy controls (age = 38.0 ± 12.8, female = 10) were enrolled and underwent standard cardiac MRI. The analysis of 4D flow MRI, left ventricle (LV), and right ventricle (RV) volumes and function were measured using cvi42 v5.11 (Circle Cardiovascular Imaging Inc., Calgary, Canada). Pre-processing corrections were applied to reduce noise, correct for eddy currents, and phase unwrapping in the case of velocity aliasing. The workflow is shown in Figure 1. Net flow, peak velocity and regurgitant flow were calculated automatically for the aorta, left pulmonary artery (LPA), and right pulmonary artery (RPA) at each plane. The relative pressure differences were calculated using a multigrid-based solver for Poisson equation [3]. Finally, energy loss was calculated as described by Barker et al [4]. Systolic and diastolic energy loss for the aorta and pulmonary artery (PA) were reported.

Results

Peak velocity of the right ventricular outflow tract (RVOT) was increased in ASD patients as compared with controls (106±49 vs. 77±17 cm/s, $p<0.05$). Regurgitation fraction of the RPA was elevated in ASD patients as compared with controls (5±10 vs. 0±1 %, $p<0.05$). The significant difference of RPA diastolic energy loss between diseased patients and controls was at the borderline (2±3 vs. 1±0 mW, $p=0.057$).

Conclusion

This study unveiled abnormal flow in ASD patients by means of pressure drop and energy loss. Peak velocity of RVOT, regurgitation fraction, and diastolic energy loss of RPA resulted the most relevant parameters for assessing ASD.

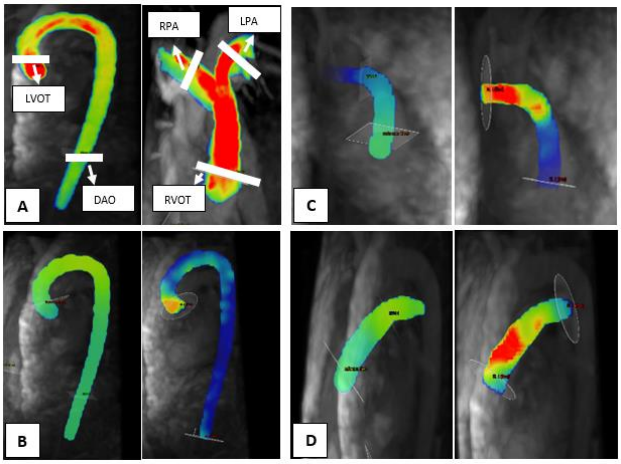

Figure 1. Workflow. **(A)** Segmentation and Analysis of Aorta and PA **(B)** Pressure drop (Left) and Energy Loss (Right) of Aorta **(C)** Pressure drop (Left) and Energy Loss (Right) of LPA **(D)** Pressure drop (Left) and Energy Loss (Right) of RPA. LVOT: left ventricular outflow tract; DAO: descending aorta.

References

[1] Adiele, D., Arodiwe, I., Chinawa, J., Eze, J., Gouthami, V., Murthy, K., … Ujunwa, F. Atrial septal defects: Pattern, clinical profile, surgical techniques and outcome at Innova heart hospital: A 4-year review. *Nigerian Medical Journal 2014;55*(2):126-9.

[2] Ebbers, T., & Farnebäck, G. Improving computation of cardiovascular relative pressure fields from velocity MRI. *Journal of Magnetic Resonance Imaging* 2009; 30(1): 54-61

[3] Barker, A. J., van Ooij, P., Bandi, K., Garcia, J., Albaghdadi, M., McCarthy, P., … Markl, M. Viscous energy loss in the presence of abnormal aortic flow. *Magnetic Resonance in Medicine* 2014; 72(3):620-8.

Investigating White Line Separation as a Potential Precursor to Toe Tip Necrosis

Nassim Hedayati[1], Álvaro Espinosa[1], Murray Jelinski[2], J.D. Johnston[1]
1. Department of Mechanical Engineering, University of Saskatchewan, Saskatoon, Canada,
2. Department of Large Animal Clinical Sciences, University of Saskatchewan, Saskatoon, Canada

Introduction

Toe Tip Necrosis Syndrome (TTNS) is a condition that occurs in the hooves of feedlot cattle, leading to inflammation, bone necrosis and breakdown of the white line [1]. It is believed that cattle damage the white line by dragging their hooves on abrasive surfaces found in feedlots [2]. This may result in small pathways for external materials to enter the hoof, which may initiate TTNS. Also, a dragged claw may be more susceptible to local damage caused by small particles (e.g., small rocks), further increasing potential for pathways to develop. Previously, a dragging-based, *ex-vivo* testing method was developed by our group to simulate potential conditions causing TTNS [3, 4]. Preliminary pilot testing indicated that both dragged claws and claws with TTNS had similar overall stiffness behavior as well as evidence of internal fractures (via high resolution imaging). Such findings support the hypothesis that dragging is involved in TTNS pathogenesis. As this pilot study was underpowered, there is a need to conduct a larger-scale study of this potential finding. To gauge propensity for pathway development, there is also a need to assess local stiffness properties along the white line. Therefore, the objective of this research is to assess whether dragging affects the local stiffness and integrity of the white line, thereby leading to a pathway for infection. This will be accomplished using a combination of mechanical dragging mimicking agitated feedlot cattle, macro-indentation testing and high resolution imaging.

Methods

Specimens will consist of lateral claws from three groups (each with 10 samples): (1) TTNS; (2) healthy; and (3) healthy claws dragged to the level of wear found with TTNS. Dragging will be done by fixing healthy claws in a material testing system simulating aggressive dragging against a standard concrete block (Fig. 1). Testing will consist of 650 cycles of dragging (compressive force: 1.5 KN; shear force: 1.4 KN) [3]. Macro-indentation testing (Biomomentum Mach 1) will be used to assess local stiffness properties of healthy claws, dragged claws and claws with TTNS. Repeated measures ANOVA will be used to compare stiffness between the 3 groups followed by post-hoc pairwise comparisons. To assess tissue integrity, 5mm diameter cores from the white line region will be imaged using desktop micro-CT (Anatomy) or synchrotron radiation micro-CT (Canadian Light Source, CLS).

Anticipated Conclusions & Contributions

We hypothesize that local stiffness properties of healthy claws will be higher than that of TTNS and dragged claws, with similar local stiffness observed between TTNS and dragged claws. Also, imaging studies will indicate minimal damage with healthy claws and similar damage with TTNS and dragged claws. Overall, the results of this study will help determine whether dragging is involved in the pathogenesis of white line degradation and the development of TTNS. This information could help guide farmers in placing less abrasive flooring systems in feedlots.

References

[1] Johnston et al., 2018; [2] Franck et al., 2007; [3] Bouvier et al., 2019; [4] Espinosa et al., 2018.

Fig. 1 [4]: Testing Equipment – Dragging Apparatus (A), Imaging Setup (B): 1. Actuators, 2. Load cells, 3. Potted claw, 4. Floor block, 5. Counterweight, 6. Alignment stage, 7. HQ camera casing

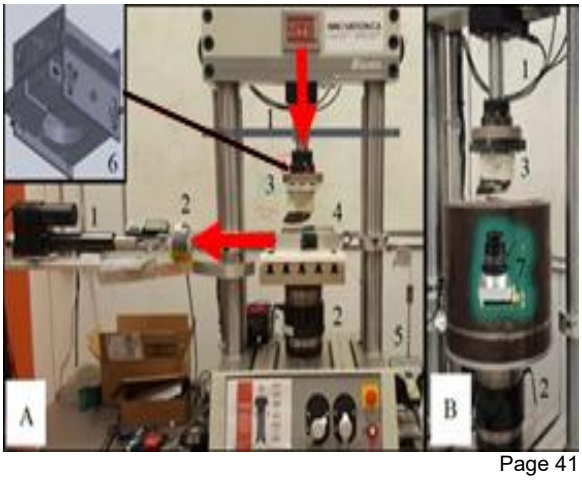

ANALYSIS OF MUSCLE ACTIVITY AND MUSCLE FATIGUE DURING A MATERIAL HANDLING TASKS

Karla Beltran Martinez | Milad Nazarahari | Hossein Rouhani
University of Alberta, Mechanical Engineering

Introduction

The cost of musculoskeletal disorders in Canada is approximately $25.6B [1] per year. Muscle fatigue is one of the main causes of these disorders after prolonged material handling tasks [2]. Therefore, it is of crucial importance to understand which muscles are being fatigued and what are their associated work-related limitations.

Methods

Six study participants performed a material handling task that consisted of moving a 16 lbs. load from table A (15 cm height) to table B (75 cm height) and then back to table A (shown in Figure 1) repeatedly until the participant reached fatigued. The tables were located one in front of the other, and the load was recommended by NIOSH to ensure the safety of all participants. The experimental protocol was approved by the local Research Ethics Board. The muscle activity was recorded using a wireless EMG system (Trigno, Delsys, USA) at 1200 Hz from the following muscles: biceps, carpi radialis, rectus femoris, tibialis anterior, biceps femoris, lateral gastrocnemius, erector spinae, triceps, and trapezius. Also, the participants were asked during the trial to rate their feeling of fatigue from 0 to 10 (where 0 means no fatigue) every two minutes. The signal was filtered with a 4th order Butterworth filter, high-pass with a cutoff frequency of 10 Hz, and low-pass with a cutoff frequency of 500 Hz. Given than the nature of the trial is a dynamic exercise, fatigue was obtained purely by finding the difference in the amplitude of the EMG signal. This amplitude was compared with the first and last 10% of the trial.

Results

All the muscles mentioned above showed to be active, however, each fatigued differently for each participant except for the erector spinae that fatigued for all six subjects with a mean increase in EMG amplitude of 52%. carpis and bicep femoris showed fatigue in 5 participants with an increase in EMG amplitude of 15% and 23%, respectively, and the remaining muscles were fatigued up to three participants. All of these EMG-based observations of fatigue were in line with the participants' feedback.

Conclusions

We identified the muscles that are the most prone to fatigue in a prolonged material handling task. In the future, these results must be further investigated with a larger population. This would allow employers and workers to take the necessary precautions to avoid musculoskeletal disorders.

References

[1] Coyte PC Asche CV The economic cost of musculoskeletal disorders in Canada.
[2] Shair, E.F. Ahmad, S.A. /// EMG processing based measures of fatigue assessment during manual lifting

Figures

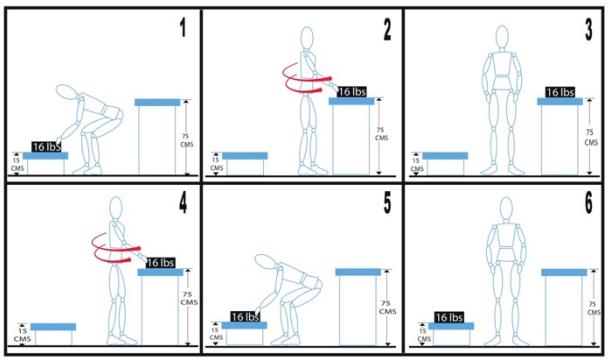

Figure 1: Experimental procedure.

Design of an Ex Vivo Mechanical Test Apparatus to Study Atraumatic Tooth Extraction

Timothy J. Gadzella[1], Dan L. Romanyk[1,2]
1. Department of Mechanical Engineering, University of Alberta, Edmonton AB
2. School of Dentistry, University of Alberta, Edmonton, AB

Introduction: Nearly 100% of Canadian adults are missing teeth for reasons ranging from trauma to tooth decay [1], making exodontia (tooth extraction) one of the most common clinical procedures. Conventional exodontia involves the use of rigid tools which can damage the remaining alveolar bone [2]. New exodontia tools attempt to reduce trauma by directing extraction forces away from the alveolar bone. For example, the Benex device applies extraction force to the tooth through a cable while supported by the nearby teeth (Figure 1) [3]. However, the biomechanics of trauma resulting from exodontia is not well understood and provides little basis to compare techniques. The objective of this study is to develop a laboratory model of Benex device extraction with known directional loading for assessing tissue damage during exodontia.

Methods: Post-mortem swine mandibles are dissected around the 2nd premolar. Samples are then potted in a rectangular mould leaving only the premolar uncovered. The crown of the premolar is planed down and the divergent roots sectioned for individual extraction. Potted samples will be imaged with a µCT scanner before being fixed to a material test frame. Previous studies of tooth extraction have fixed the sample in rigid alignment with the test frame, with orthodontic wires passed through the crown of the tooth [4]. Rigid fixation may induce moments in the tooth root that cannot be easily measured, cause fracture during extraction, and confound boundary conditions for numerical models. In our study, the root is threaded with an insert which interfaces with the loading cable. The test apparatus combines rolling elements with a universal joint, providing four degrees of freedom about which the sample can self-align the root axis to the load (Figure 1). Although the Benex device is typically used to apply step loads in the clinic, quasistatic load rates (0.2-2mm/min, 10-100N/min) were selected for this pilot study to initially assess viscoelastic tissue responses and strengths. Extraction forces and total displacement will be recorded by the test frame. Complete extraction will be marked by a drop in force and subsequent inability of the sample to resist load. Post-extraction µCT images will be obtained of the bone and residual tissue.

Results: This study is ongoing. Preliminary tests with metal substitutes for premolars indicate that the apparatus is successful in aligning the sample axially during preload. Force-displacement curves from post-mortem samples will be assessed for slope discontinuities and differences among load rates characterizing the tissue response. Image processing will be used to determine changes to the bone between CT scans.

Conclusions: The outcome of this study will be a controlled experimental model with qualitative and quantitative metrics of tissue damage. Using a self-aligning test apparatus will establish these criteria with a known load state at the tooth root. Future work will apply this method to step-loading regimes on post-mortem samples and develop a computational model to determine predictive damage criteria.

References

[1] Stephens et al, 1991. *J Canadian Dental Association.* [2] Hupp et al, 2019. Contemporary oral and maxillofacial surgery (7th Ed). [3] "An innovative atraumatic extraction system", 2019. *Br Dent J.* [4] Genna et al, 2014. *J Mech Mater Struct.*

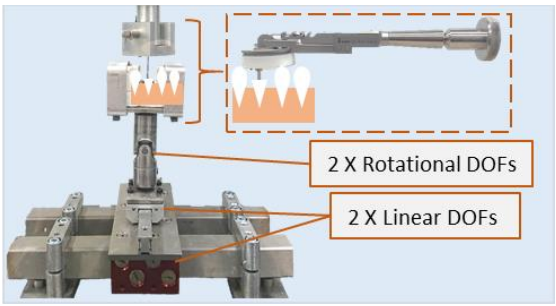

Figure 1: Axial extraction test apparatus with linear and rotational degrees of freedom simulating procedure with a Benex device (upper-right inset).

Frontlimb and hindlimb kinematics in horses during swimming

E. Santosuosso[1]; C. Rolian[1]; P. McCreae[1]; S. Massie[1]; F. David[2]; T. Vinardell[2]; R. Leguillette[1]
[1]:Faculty of Veterinary Medicine, University of Calgary; [2]:Equine Veterinary Medical Center, Al Shaqab, Doha, Qatar

Introduction

Swimming is used empirically for rehabilitation and conditioning of horses. The purpose of our study was to quantify for the first time the motion of horses' limbs during swimming. The specific objectives were to 1) calculate joint angles, angular velocity (AV) and acceleration (AA) 2) compare the AV and AA between joints 3) compare the values obtained for the frontlimbs and the hindlimbs.

Methods

11 endurance horses swam in a long straight equine pool. Waterproof markers were applied on the hooves, fetlocks, tarsus, stifle and great femoral trochanter. Two-dimensional movement was recorded underwater and manually tracked. The obtained coordinates were used to calculate joint angles, velocities and accelerations. ANOVA and Tukey post-hoc tests were used to compare data between joints.

Results

The carpus had the greatest range of motion (ROM) and the smallest AV. The stifle and tarsus had the greatest ROM and the tarsus had the max AV. Greater absolute values of AV were observed during retraction phase for all joints. Within limbs comparison of joints showed that the front fetlock and the stifle had the greatest AV. Between limbs comparison showed that the forefetlock AV is greater than the hindfetlock AV, but the tarsus and stifle AV are greater than the carpus and elbow AV, respectively. The AA of the hindlimb was greater during retraction.

Conclusion

These findings show that swimming of horses should be recommended in rehabilitation programs when an increased ROM and AV of the hindlimb upper joints and of the forelimb carpus are desirable.

Optimization of pulsatile flowmeter for use in ex-vivo heart perfusion device

Bryce Palichuk[1], Katie Cameron[2], Steven Cruz Antunes[2], Calvin Jee[2], Reza Sabbagh[1], David Nobes[1]
[1]Department of Mechanical Engineering, University of Alberta, Edmonton, AB
[2]Tevosol, Edmonton, AB

Introduction

Ex-vivo heart perfusion (EVHP) is the process of continuously pumping blood through a donated heart once it has been procured from the donor. It aims to replace the traditional approach of storing the heart in cold storage prior to transplantation into a recipient. Precise volume flow rate measurements of the pulsatile flow are needed to assess the performance of the heart allowing the surgeon to determine the heart's viability before transplantation. Current technologies for measuring volume flowrate, such as ultrasonic flow meters, are expensive, space consuming and unable to measure the pulsatile flow on the time scale needed for the portable EVHP system. The focus of this investigation is to understand how precise volume flow rate measurements can be achieved with a small, low cost device.

Methods

Computational fluid dynamics (CFD) was utilized via an optimization study in a commercial code (SOLIDWORKS FLOW), as seen in Figure 1, to determine the internal pressures needed to optimize the flowmeter geometry based on the work of [1]. To validate the CFD simulations, experimental prototypes were SLA 3D printed (Form2, FormLabs Inc.) and an experimental flow loop was developed using a left-ventricular assisted device (LVAD) to generate a pulsatile flow. In the experimental setup, differential pressure transducers are attached to the three pressure taps and a data acquisition device (DAQ) that converts the continuous pressure into discrete electrical voltages at a certain sampling frequency is also used. The volume flow rate will then be derived from the differential pressure readings acquired from the DAQ device.

Results

Initial CFD simulations were completed with water as the working fluid and a target value of 3.447 kPa (0.5 psi, 26 mmHg) of pressure drop between the upstream and throat pressure taps. This targeted pressure value was used as starting point to create the optimization workflow and to develop the initial experimental prototypes.

Conclusion

A small, low cost pulsatile flowmeter with the ability to provide precise volume flow rate measurements within an EVHP system is crucial. The CFD simulations undertaken in this investigation used internal pressure values to identify the key geometrical parameters needed for optimization of the flowmeter. Experimental prototypes were then SLA 3D printed based upon the CFD data and will be tested within the experimental flow loop.

References

[1] A. Beaulieu, E. Foucault, P. Braud, P. Micheau, and P. Szeger, "A flowmeter for unsteady liquid flow measurements," *Flow Meas. Instrum.*, vol. 22, no. 2, pp. 131–137, 2011.

Figures

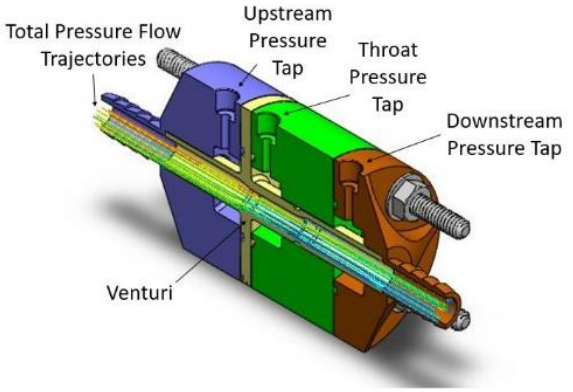

Figure 1: Horizontal section cut of preliminary design with total pressure flow trajectories calculated in CFD

Effect of Upper Arch Expansion by Invisalign on Nasal Airway Volume in Children

Boyu Pan[1], Tarek El-Bialy[2], Lindsey Westover[1]
1 Department of Mechanical Engineering, University of Alberta. 2 Faculty of Medicine and Dentistry, University of Alberta

Introduction

Millions of adults and children around the world are affected by obstructive sleep apnea (OSA). OSA occurs because of obstruction of the airway at different levels including constrictions due to a narrow upper jaw and underdeveloped/backward positioned lower jaw. Treatment options for OSA include continuous positive airway pressure (CPAP), oral appliance therapy, and various surgical treatments [1].

Rapid maxillary expansion has been shown to increase nasal cavity volume and decrease nasal airway resistance [2,3]. Furthermore, slow maxillary expansion has also been shown to increase nasal cavity volume [3]. We hypothesize that upper arch expansion using Invisalign clear aligners may improve the nasal airway in children.

Therefore, the objective of this study is to determine the possible 3D changes in the nasal airway after maxillary arch expansion using Invisalign Child clear aligners.

Methods

Using a retrospective study design, participants (n = 11) between the ages of 8 to 11 years who had been diagnosed with a constricted maxilla and had been treated with Invisalign Child aligners as an expansion treatment were identified from a local orthodontic clinic. The patients identified had cone beam computed tomography (CBCT) scans both before and after their treatment as part of their clinical care. Age and sex matched control subjects (n = 11) who had two CBCTs (approximately 1 year apart) but without treatment were also identified. Approval was obtained by the U of A Health Research Ethics board.

The nasal airway region of interest is isolated and segmented from the CBCTs using MIMICS (Materialise). 3D models of the nasal airway are created and exported as STL files.

The 3D models at time T1 (pre-treatment) and time T2 (post-treatment) are compared using Geomagic Control (3D Systems). The volume and surface area of the models are compared. Additionally, the models are aligned using closest-point-iteration (best-fit alignment function) and a 3D deviation map is created (3D compare function) showing the areas of deviation between the two models.

Paired t-tests are conducted to evaluate differences between pre- and post-treatment for both the test patients and the control group. The segmentation and 3D analysis procedures are completed by three independent observers to determine inter-observer reliability of the approach.

Results

We have successfully developed a protocol for segmentation and construction of 3D models for the nasal airway. Additionally, we have successfully implemented preliminary analysis of pre- and post-treatment 3D models to identify differences associate with maxillary arch expansion using clear aligners.

Conclusions

Future work will aim to apply the developed approach to the full dataset of n = 11 test patients and n = 11 control subjects. This work aims to show the effectiveness of Invisalign Child clear aligners for nasal airway expansion. This would provide the potential to indicate such aligners as a possible treatment for obstructive sleep apnea.

References

[1] Pavwoski and Shelgikar. 2017. Neurol Clin Pract. 7(1): 77-85.
[2] De Felippe et al. 2008. Am J Orthod Dentofacial Orthop. 134(3): 370-382.
[3] Lanteri et al. 2020. Materials. 13, 2239; doi:10.3390/ma13102239

Left Ventricular Flow Analysis in Atrial Fibrillation

Hansuk Kim, Hana Sheitt, Fatemehsadat Jamalidinan, Stephen Wilton, James White, Julio Garcia
Libin Cardiovascular Institute – Stephenson Cardiac Imaging Centre, Departments of Radiology and Cardiac Sciences, University of Calgary, Alberta, T2N 2T9

Introduction

Atrial fibrillation (AF) is a common global disease which 33.5 million individuals. AF is characterized by the irregular beating of the heart which is treated by catheter ablation. Cardiac magnetic resonance (CMR) and 4D flow imaging have been used to study AF patients. Left ventricular (LV) flow component analysis has been used to associate blood flow distribution with heart diseases [1]. In this method, LV blood flow during the heart cycle is divided into four components, and their volumetric proportion is compared to assess heart function. We hypothesize that blood flow distribution is abnormal in AF pre-ablation patients.

Methods

A total of 28 patients with AF (age= 56.4±12.3 years, female=9) and 10 controls (age=50.2±8.8 years, female=2) were studied. All patients and healthy subjects underwent a standardized CMR imaging protocol including whole heart 4D flow MRI. Volumetric and functional parameters were measured from short-axis LV images. 4D flow imaging was analyzed to calculate LV flow components using cvi42 v5.11 (Circle Cardiovascular Imaging Inc., Calgary, Canada). We calculated pathlines of ventricular flow from three-dimensional velocity using the Runge-Kutta method [2]. The trajectories were categorized into four flow components. The proportion of each component was compared with structural and functional biomarkers from CMR. An independent-samples t-test between AF and control groups and a Pearson's correlation between remarkable variables were performed.

Results

The patient and control groups were generally similar in demographics and baseline characteristics, though diastolic blood pressure was higher in AF patients than in controls (70±11 mmHg vs. 58±16 mmHg, P=0.026). When comparing myocardial structure and function parameters, LV stroke volume was significantly different between the two groups (91±22 mL vs. 105±9 mL, P=0.007). From LV flow component analysis, AF patients had a significantly greater portion of delayed ejection and retained inflow (15.5±6.0% vs. 9.7±3.6%, P=0.001) while residual volume reduced (17.9±6.3% vs. 28.1±9.3%, P=0.0004) (Figure 1). Delayed ejection and retained inflow had a strong correlation with LV stroke volume (r=-0.511, P=0.001). On the other hand, residual volume was not dependent on LV stroke volume (r=-0.069, P=0.679).

Conclusions

This study applied LV flow component analysis to AF pre-ablation patients to explore a possible indicator for AF. The residual volume component has shown to be an independent and significant index to distinguish AF from controls.

References

[1] J. Eriksson, C. Carlhäll, P. Dyverfeldt, J. Engvall, A. Bolger, and T. Ebbers, "Semi-automatic quantification of 4D left ventricular blood flow," J. Cardiovasc. Magn. Reson., vol. 12, no. 1, p. 9, Dec. 2010, doi: 10.1186/1532-429X-12-9.

[2] J. Butcher, "Runge-Kutta methods," Scholarpedia, vol. 2, no. 9, p. 3147, 2007, doi: 10.4249/scholarpedia.3147.

Figures

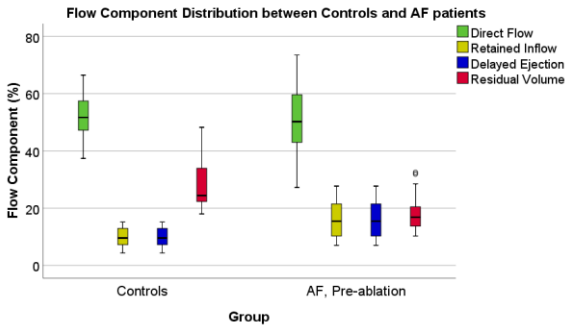

Figure 1: LV Flow Component Distribution

Optimization of ex-vivo heart perfusion (EVHP) systems and the effect of compliance properties on the flow

Guilherme Bessa[1], Jake Hadfield[1], Kaelyn Nicolson[2], Hyun-Joong Chung[2], Reza Sabbagh[1], Darren H. Freed[3], David S. Nobes[1]

1-Department of Mechanical Engineering, University of Alberta, Edmonton, AB, Canada
2-Department of Chemical and Materials Engineering, University of Alberta, Edmonton, AB, Canada
3-Department of Surgery, Physiology & Biomedical Engineering, University of Alberta, Edmonton, AB, Canada

Introduction

Ex-vivo heart perfusion (EVHP) maintains a human donor heart beating outside the body for the time preceding transplantation surgery. In previous work [1], it was shown that the use of a compliant tube instead of standard rigid tubing in the EVHP system's flow loop could alter the flow-pressure relationship of the pulsatile flow, making it more similar to the physiological profile and also reducing the workload in the heart [1]. The present work aims to further investigate the relationship between pulsatile flow and compliance by assessing the effect of tube properties on the downstream pressure and flow fields. To this end, a silicone tube of variable compliance, length, and geometrical shape were developed for this study, in addition to an experimental setup containing a hydraulic circuit analogous to the left flow loop of the EVHP system.

Method

A pulsatile waveform is generated using a computer-controlled mechanical diaphragm pump, also equipped with a tri-leaf exit valve to simulate the physiological working condition of the heart. The flow features downstream of the compliant tube are collected using laser Doppler velocimetry (LDV). The pressure waveforms are acquired using medical pressure transducers installed at relevant flow loop locations, such as just before and right after both the pump and compliant section. A schematic of the experimental setup is shown in Figure 1. The compliant tubes are in-house manufactured using a 3D SLA printer (Form2, FormLabs Inc.) to generate the external molds and the tubular skeletal support structures, as shown in Figure 1, followed by silicone casting (Ecoflex™ 00-50 or Dragon Skin™ 10).

Results

Baseline experiments were carried out using a pure silicone tube made with Ecoflex™ 00-50. Figure 1 shows the pressure waveform and the centerline velocity measured downstream of the compliant section for one pump cycle (1 Hz). Two peaks can be seen both in the pressure waveform and in the axial velocity component curve. The first peak occurs during the pump ejection phase and the second one, which occurs during the pump recovery phase, is due to the reflected pressure wave.

Conclusions

The results of this research will help to achieve a better understanding of how the compliance response affects the pressure and flow fields. Based on the results, the EVHP system can be optimized to improve the efficiency using the selected compliant geometry and material.

References

[1] K. G. Cameron, "Investigation into the effect of compliant response on fluid flow in an ex vivo heart perfusion test system", University of Alberta, 2017.

Figures

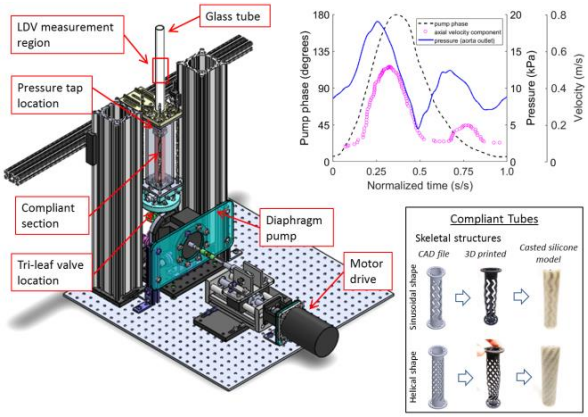

Figure 1: Schematic of the experimental setup with preliminary results and compliant tube models.

Chondrocyte Morphological Response during Cyclic Dynamic Loading

Darius A. Ramrattan [1,3], Baaba S. Otoo[2,3], and Walter Herzog[3]
[1] Department of Biological Sciences, Faculty of Science, University of Calgary (Calgary, Canada)
[2] Schulich School of Engineering, University of Calgary (Calgary, Canada)
[3] Human Performance Lab, University of Calgary (Calgary, Canada)

Introduction

Articular cartilage is an avascular tissue found in joints and contains chondrocytes, the unique cell line tasked with maintaining the extracellular matrix (ECM) [1]. While mechanical loading compresses articular cartilage, little is known about how this compression affects the mechanobiology of individual chondrocytes in a cyclic loading environment, due to limitations in quantifying the mechanics and biology at a high temporal rate required for dynamic loading conditions. Therefore, much of the previous work in this area has focused on static loading due to the challenges associated with tracking and observing individual cells during the process of cyclic dynamic loading (CDL) [2]. It has been shown that static loading *in vivo* results in a big decrease in chondrocyte volume that occurs virtually instantaneously, but then it takes minutes for cells to fully recover their initial volume upon unloading [3]. It has been suggested that patterns of cartilage deformation resulting from static and dynamic loading differ substantially [2] but unequivocal data on this topic are lacking. The aim of this study was to investigate the changes in shape and volume of chondrocytes embedded in their native environment in the three zones of cartilage in response to CDL in real time. Despite the challenges of studying CDL, it represents more accurately loading patterns of day-to-day activities like walking and provides better insight into the cellular physiology of chondrocytes [2].

Methods

Cellular strains were quantified by assessing the volumetric and the three primary axial strains of cells during the unloading phases of a cyclic loading protocol applied to porcine (*Sus scrofa)* femoral cartilage at a frequency of 0.2 Hz and at a loading amplitude of 20% strain for a total of 100 cycles. Strains in three axes were assessed, corresponding to changes in cell height, cell width, and cell depth. The analysis was performed using ImageJ and PyCell analyst software to segment chondrocytes from matrix using two photon laser scanning fluorescence microscopy scans.

Results

Superficial zone cells increased in volume until cycle 100. Middle zone cells also increased in volume until cycle 100. The axial strain corresponding to cellular depth in the deep zone cells increased from early cycles (1-5), peaking during the middle cycles (7-10), then decreased from the middle (7-10) to the late cycles (20-100).

Conclusion

The results of this study led to the conclusions that dynamic loading results in distinctly different chondrocyte shape and volume changes than static loading and that the patterns of shape and volume changes in dynamically loaded cartilage depends crucially on the location (zone) of the cells within the cartilage.

References

[1] Huber et al. Invest Radio 2000
[2] Eckstein et al. J. Biomech 2000
[3] Abusara et al. J. Biomech 2010
[4] Moo and Herzog. J. of Ortho Research 2017

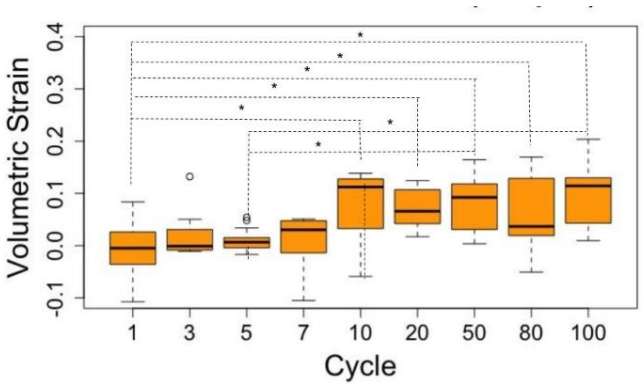

Figure 1: Volumetric strain as a function of loading cycle for n≤14 Middle zone cells. *indicates statistical difference between neighboring cycles shown (p≤ 0.05).

Bone Morphometry from Level Set Embeddings

Bryce A. Besler[1,2], Tannis D. Kemp[2], Nils D. Forkert[3,4], Steven K. Boyd[2,4]
[1]Biomedical Engineering Graduate Program [2]McCaig Institute for Bone and Joint Health
[3]Department of Radiology [4]Hotchkiss Brain Institute, University of Calgary

Introduction

As bone remodels, plates can form holes and rods can disconnect, changing the topology of the surface. Changes in topology are difficult to model computationally. Recently, bone adaptation has been modelled as a curve motion problem by conceptualizing the bone surface as the zero level set of an embedding function [1]. This allows modeling of topological changes that occur as the bone adapts. Towards developing methods of modeling bone adaptation, measuring bone morphometrics from the embedding would centralize analysis, allow for optimization of these measures, and unify theory around adapting surfaces.

In this work, classic measures of bone morphometry are computed using advanced level set methods. A validation study is conducted comparing the proposed method to standard techniques.

Methods

A method is proposed for the measurement of bone volume (BV, [mm^3]), bone surface area (A [mm^2]), total mean curvature ($\overline{H}$, [mm]), and total Gaussian curvature ($\overline{K}$, [-]) from level set embeddings. Connectivity density (Conn.D, [mm^{-3}]), structure model index (SMI, [-]), and trabecular bone pattern factor (TBPf, [mm^{-1}]) are derived quantities.

10 previously imaged bovine tibial trabecular bone cubes were used [2]. Bone cubes were sawed to 10 mm in edge length and imaged at a nominal resolution of 20 μm. Greyscale data were Gaussian filtered (sigma = 0.8, support = 1) to remove noise, cropped to remove cutting artifacts, and binarized via thresholding (250.0 mg HA/cc). Standard algorithms were applied to measured BS, BV, Conn.D, and SMI for each bone cube.

Cubes were embedded by a distance transform and two iterations of min/max curvature flow [3] were applied to remove surface noise. The proposed method was applied directly on the embeddings to measure the outcomes. Linear regression analyses were used to compare the methods.

Results

Regression plots are given in Figure 1. Bone surface area, bone volume, and structure model index agreed very well (R^2 > 99%). Connectivity density agreed less well (R^2 = 53%). This is likely caused by the removal of small particle noise during min/max curvature flow. Small particles greatly decrease the Euler characteristic and thus connectivity density of the surface.

Conclusions

Estimation of surface area, volume, and structure model index but not connectivity density agree between the proposed and standard methods. Future work will use this method to measure the relation of bone adaptation to local surface curvature.

References

[1] Besler *et al* (2018) MICCAI-MSKI
[2] Sandino and Boyd (2013) Computational Biomechanics for Medicine
[3] Malladi and Sethian (1995) PNAS

Figures

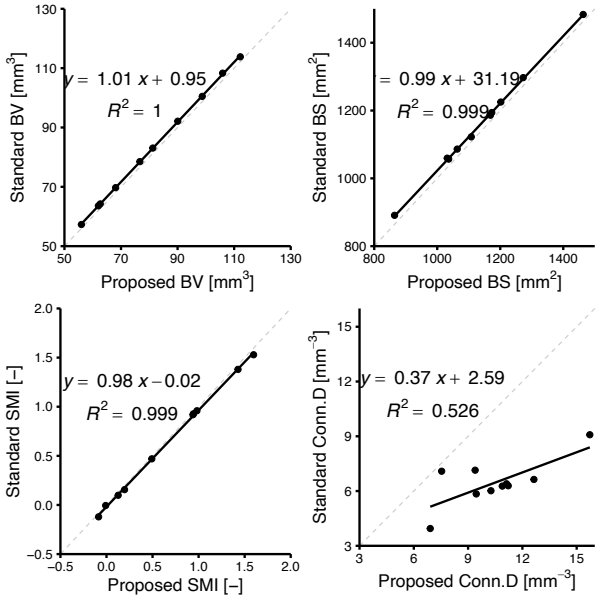

Regional depth-specific subchondral bone density measures in osteoarthritic and normal distal femora: in vivo precision and links with pain

[1] Sacher, AE; [1]Burnett, WD; [2]Wilson DR; [3]Hunter DJ; [1]Kontulainen SA; [1]Johnston JD
[1]University of Saskatchewan, [2]University of British Columbia, [3]University of Sydney

Introduction: Knee osteoarthritis (OA) is a degenerative joint disease marked by pain and altered cartilage and subchondral bone [1]. The exact role of subchondral bone in OA initiation and progression, as well as pain, is not well understood [2]. However, relationships between bone mineral density (BMD) and pain have been shown at the proximal tibia [3, 4] and patella [5]. Currently, no studies have investigated links between pain and BMD at the distal femur.

To address this gap in the literature, the objectives of this research are as follows:

1. Develop an automated image processing algorithm for assessing regional and depth-specific BMD at the distal femur.
2. Determine precision errors of the distal femoral density measures.
3. Examine relationships between clinical symptoms of OA (disease severity, knee pain) and distal femoral density measures.

Methods: *Objective 1:* This research will develop a variation of image processing algorithms written by Johnston et al. [6], Speirs et al. [7] and Wright et al. [8] to analyze regional measures of distal femoral subchondral BMD. Density will be measured at specific depths from the subchondral surface (0-2.5, 2.5-5, 5-10mm) as well as at different regions (medial/lateral, anterior/central/posterior), as per the MOAKS approach [9].

Objective 2: Fourteen participants (2 men and 12 women; mean age 51.4, SD 11.8 years) were scanned using clinical quantitative computed tomography (QCT) three times over two days as part of a previous research study. Participants were categorized as either normal (n = 7) or exhibiting signs of radiographic OA (n = 7). From this data, we will assess precision errors (root mean square coefficients of variation, $CV\%_{RMS}$) of depth-specific, distal femoral BMD measures [10].

Objective 3: The knees of 42 participants (17 men and 12 women; mean age 64, SD 10.1 years) scheduled to undergo knee arthroplasty were previously scanned using QCT. Each participant's knee pain was quantified using the Western Ontario and McMaster Universities Arthritis Index (WOMAC) [11]. Clinical pain symptoms will be related to regional BMD measures using statistical correlation analyses (Pearson, Spearman rank).

Anticipated Contributions: This research will develop a new image processing method for assessing distal femoral BMD as well as attempt to further elucidate the role of bone in OA-related pain. This is important as improving our understanding of OA pain pathogenesis is crucial for developing preventive and therapeutic treatments [12]. Further, as OA affects the entire joint, identifying which structural abnormalities contribute most to pain may allow clinicians to adopt more targeted approaches to address OA [12]. Lastly, our findings may be valuable in guiding future OA studies addressing subchondral bone and pain, particularly in ROI selection.

References: [1] Hunter 2006; [2] Burr, 1997 [3] Burnett et al., 2017; [4] Burnett et al., 2015; [5] Burnett et al., 2016 ; [6] Johnston et al., 2009; [7] Speirs et al., 2013; [8] Wright et al., 2012; [9] Hunter et al., 2011; [10] Gluer et al., 1995; [11] Bellamy et al., 1988 [12] Neogi, 2012;

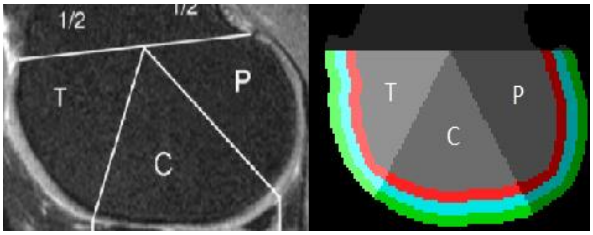

Fig 1. Side-by-side comparison of MOAKS regions [9] and our defined regions and depths

Surface Topography for Evaluation of Schroth Exercise in Adolescents with Idiopathic Scoliosis: A randomized Controlled Trial (RCT)

Nada Mohamed[1], Vivechana Acharya[2], Eric C. Parent[3], Lindsey Westover[1],
[1]Department of Mechanical Engineering, University of Alberta, [2]Department of Civil and Environmental Engineering, University of Alberta, [3]Department of Physical Therapy, University of Alberta

Introduction

Adolescent idiopathic scoliosis (AIS) is a three-dimensional torsional deformity of the spine and trunk[1]. Based on Cobb angle measurements, prescribed treatment can include observation, bracing or surgery. The Schroth exercise program is a physiotherapy scoliosis specific exercise to correct posture and reduce curve progression[2]. Using surface topography analysis (ST), the objective of this study was to determine the effect of Schroth exercises added to standard care compared to standard care alone in patients with AIS.

Methods

Patient with AIS were randomly allocated to two groups: Control (n=55) and Schroth (n=65). The control group received standard care (observation or bracing). The Schroth group received a six-month Schroth exercise treatment in addition to their standard care. Prescribed Schroth exercises are tailored for each of the four scoliosis curve types[3]. The ST analysis method consists of capturing a full 3D model of the patient's torso which is then reflected along the plane of symmetry to create a reflected torso model (Figure 1). The reflected torso was then aligned with the original torso by minimizing the distance between surfaces. Based on the distance between the original and reflected torso models, a deviation color map (DCM) was created[4]. The individual patches are defined as the areas affected by the scoliosis deformity. The absolute threshold value for a normal deviation was 3 mm. However, a greater absolute threshold of 9.33 mm was also applied for cases when the maximum deviation is greater than 9.33 mm to get a clearer separation of patches[5]. Asymmetry patches from the DCM were isolated, and measurement of the maximum deviation (MaxDev) and root mean square (RMS) were calculated for the largest patch by area. Intention to treat analysis was carried out to account for missing data. The ST asymmetry analysis avoided bias by ensuring blinding of the evaluator to the group allocation.

Results

Over the six-month period, RMS measurement in the Schroth group decreased by 7.5% (-0.9 mm, 95% CI -0.3 to -1.5 mm), while RMS increased by 0.8% (0.1 mm, 95% CI -0.7 to 0.8 mm) in the control group (Figure 2a). The repeated measures ANOVA detected significance for the time by group interaction (p=0.037). Additionally, MaxDev measurement in the Schroth group decreased by 8.7% (-1.5 mm, 95% CI -0.5 to -2.5 mm), while MaxDev increased by 0.6% (0.1 mm, 95% CI -0.9 to 1.1 mm) in the control group (Figure 2b). The time by group interaction was also found to be significant (p=0.028).

Conclusions

Schroth exercises added to standard care helped reduce torso posture asymmetry measurements compared to standard care alone for patients with AIS.

References

1. Negrini et al., Scoliosis, vol 3, p.3, 2012
2. Fusco et al., Physiotherapy Theory and Practice, vol 27, p.80-114, 2011
3. Watkins et al., Scoliosis, vol 7, p.22, 2012
4. Komeili et al., The Spine Journal, vol 7, p.973-983, 2014
5. Ghaneei et al., BMC Musculoskeletal Disorders, vol 19, p.385, 2018

Figures

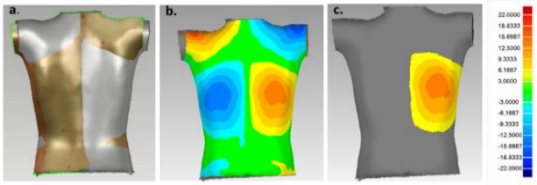

Figure 1: ST method showing a) alignment of original and reflected torso, b) DCM, and c) isolated largest patch

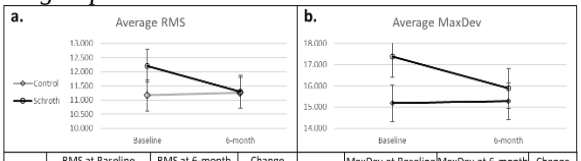

	RMS at Baseline (mm)	RMS at 6-month (mm)	Change (%)
Control	11.2 ± 0.6	11.3 ± 0.5	0.8
Schroth	12.2 ± 0.6	11.3 ± 0.6	-7.5

	MaxDev at Baseline (mm)	MaxDev at 6-month (mm)	Change (%)
Control	15.2 ± 0.9	15.3 ± 0.9	0.6
Schroth	17.4 ± 1	15.9 ± 0.9	-8.7

Figure 2: Average(mm) ± standard error of a) RMS and b) MaxDev of Schroth and Control groups over time.

Assessment of Bone Quality using HR-pQCT in Females with Celiac Disease, Inflammatory Bowel Disease and Systemic Lupus Erythematosus

Rachel Klassen[1,2], Lauren A Burt[2,3], Leigh Gabel[2,3], Danielle E Whittier[2,3], Steven K Boyd[2,3]
[1]Department of Anthropology, University of Calgary
[2]McCaig Institute for Bone and Joint Health, University of Calgary
[3]Department of Radiology, University of Calgary

Introduction

More than 585 thousand Canadians suffer from chronic autoimmune inflammatory diseases including celiac disease (CD), inflammatory bowel disease (IBD), or systemic lupus erythematosus (SLE) [1, 2, 3]. The extent to which these diseases affect bone is not understood [4]. The aim of this study was to identify differences in bone density, microarchitecture, and estimated bone strength in females with at least one of the selected autoimmune diseases compared with females without autoimmune disease.

Methods

High resolution peripheral quantitative computed tomography (HR-pQCT, 61µm resolution) was used to image the distal radius and tibia in females with CD, IBD or SLE (clinical group, n=25) and age-matched female healthy controls (n=50) [5]. Mann-Whitney Tests identified differences in total BMD, estimated bone strength using finite element analysis, and trabecular and cortical microarchitecture between the clinical and control groups.

Results

No significant differences in bone density, microarchitecture or strength were found between the clinical and control groups ($p>0.05$). In a sub-analysis between pre- and post-menopausal females within the clinical group, post-menopausal females had greater cortical porosity at the radius and tibia (0.25% vs. 0.87% and 0.97% vs. 3.21% respectively, $p=0.001$ for both), as well as 10.2% lower tibial cortical BMD ($p=0.007$) compared with pre-menopausal females. In a second sub-analysis, females in the clinical group taking drugs known to affect bone metabolism had 15.0% and 20.8% lower total and trabecular area at the radius ($p=0.01$, $p=0.04$), respectively, than clinical group females not taking bone altering medication. Visual examination of HR-pQCT images identified pathological bone typical of the clinical group (Figure 1).

Conclusions

These results suggest that within the clinical autoimmune disease group, post-menopausal females and females taking bone altering medication exhibit lower bone quality than matched controls. It is likely that disease activity/remission was a confounding factor. This study is limited by the small sample size of 25 participants and an unknown date of diagnosis. Future studies should examine individual autoimmune diseases and include detailed assessment of disease history.

References

[1] "Celiac Disease - The Gluten Connection" - Canada.ca.
[2] Kaplan et al (2019). J Can Assoc Gastroenterol. 2(1):6-16.
[3] Fatoye et al (2018). Rheumatol Int. 38(9):1721–1726.
[4] Valero et al (2019). Clin Rev Bone Miner Metab. 17(3):152–159.
[5] Whittier et al (2020). Osteoporosis Int. 31:1607-1627.

Figures

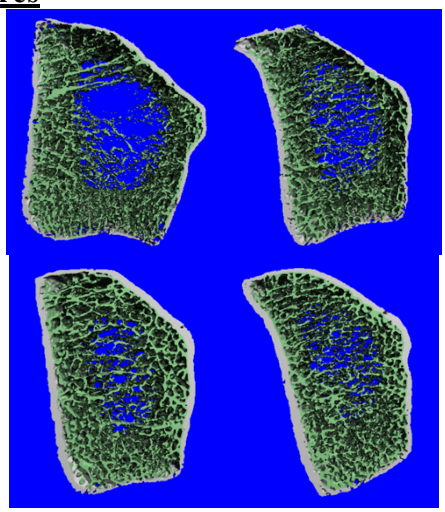

Figure 1. Pathological radii from the clinical group.

Validation of phantom-less calibration for CT muscle analysis

Ainsley C.J. Smith[1,2,3], Andrew S. Michalski[1,2,3], Steven K. Boyd[1,2,3], Sarah L. Manske[1,2,3]
[1]Biomedical Engineering Graduate Program; [2]Department of Radiology, Cumming School of Medicine; [3]McCaig Institute for Bone and Joint Health, University of Calgary, Alberta, Canada

Introduction

Muscle density loss is characterized by fat infiltration, which can lead to muscle weakness, fractures, and reduced quality of life.[1,2] It is not clear how muscle density loss relates to many musculoskeletal disorders, but this may be explored using clinical computed tomography (CT) scans.

CT images provide information about muscle density in Hounsfield Units (HU), which are specific to CT scanners and scan protocols.[3] To compare densities between scanners and protocols, a density calibration phantom with known density values (kg/m^3) is typically used. Unfortunately, this is not often done in a clinical setting, which presents a challenge for using clinical data for research.

To solve this problem, Michalski et al. (2019) developed a phantom-less calibration technique based on internal reference regions within the scan that estimate the effective scan energy to derive the relationship between Hounsfield units (HU) and material density.[4] This technique has been validated for bone, but not for muscle.

The objective of our study is to validate the use of the phantom-less calibration technique for muscle density analysis in chest CT scans.

Methods

We used ITK-SNAP to segment muscle at a cross-sectional slice of the first lumbar vertebra on 11 CT scans. We then applied the phantom-less calibration technique by defining ROIs of tissues with known densities (bone, blood, air, fat, muscle).[4] We will compare the density values from the phantom-less and the phantom calibration method using a Bland-Altman analysis.

Results

Our results are preliminary. Our first participant had a mean muscle density of 39 HU. Using the phantom-less calibration technique, the linear relationship between material density (g/cm^3) and Hounsfield units was derived (see figure 1). The material density of the muscle of this participant 1 calculated to be 1.01 (g/cm^3). The next steps in data analysis include using the phantom calibration technique to determine the material density for this participant and others.

Conclusions

Clinical CT scans are a potential research tool to retrospectively study muscle density loss in patients at risk of frailty and sarcopenia. If validated, the phantom-less calibration technique could facilitate future research on muscle density using scans that were completed for clinical purposes. This takes advantage of the enormous amount of CT data in hospital databases.

References

1. Barreiro, (2018). Annals of Translational Medicine 6(2): 29–29.
2. Hamrick et al., (2016). Frontiers in Endocrinology 7: 1.
3. Groell et al., (2000). Computerized Medical Imaging and Graphics 24(2): 53–58.
4. Michalski et al., (2020) Medical Engineering and Physics 78: 55–63.

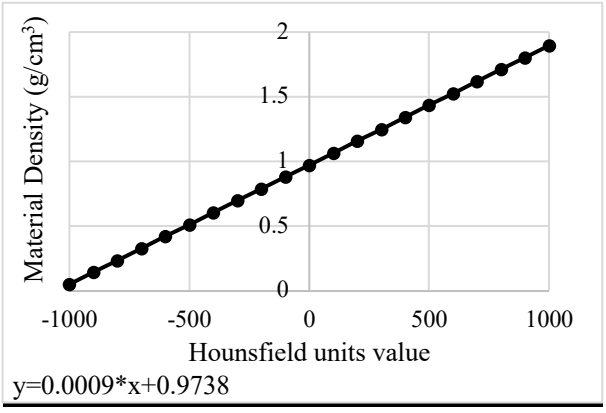

Figure 1: The relationship between HU and material density (g/cm^3) for participant 1 derived using the phantom-less calibration technique.

Automating Depth-Specific Density Analyses of the Patella

[1]Egeonu, IT; [1]Johnston, JD; [1]Kontulainen, SA; [1]Sacher, AE; [1]Franco, PB; [2]Neogi, T; [3]Lynch, JA
[1]University of Saskatchewan, Saskatoon; [2]Boston University, Boston; [3]University of California, San Francisco

Introduction

Osteoarthritis (OA) is a painful, debilitating joint disease marked by altered cartilage as well as altered subchondral bone. It is unclear where OA-related pain arises from, but it is thought to be related to bone, which is highly innervated when compared alongside cartilage, which is aneural [1].

Prior research of the patella indicates that altered bone mineral density (BMD) may be involved in pain pathogenesis [2]. Specifically, low depth-specific patellar BMD measured in relation to depth from the subchondral bone surface was associated with pain at rest [2]. This prior research was completed on a relatively small sample (n=42) and there is need to investigate links between BMD and pain with a larger sample. One such sample is the Multicenter Osteoarthritis Study (MOST), an imaging study of 2000 individuals with different degrees of knee pain and OA progression.

Unfortunately, large-scale imaging studies are challenging as many analyses require user-input (e.g., manual segmentation with manual correction, landmark selection for alignment purposes). In order to perform large-scale analyses of patellar BMD, there is a need to automate these processes.

The objectives of this research are:

1. Develop an automatic method for segmenting the patella
2. Develop an automatic method for assessing depth-specific BMD of the patella
3. Apply the developed method with the MOST cohort to study links between clinical measures of pain and patella BMD

Methods

Objective 1: Automatic segmentation will be accomplished using a combination of filtering, morphologic operators and region growing. Agreement between the automated and manual segmentation approaches will be evaluated using two dice scores, one for the total bone and the other for the bone surface (+/- 1 layer).

Objective 2: We will automate the depth-specific image processing method previously used to assess patellar density [1]. A critical step involved with this method is placing the patella in a neutral orientation before performing regional analyses. Here, manually selected landmark points are used to define the neural orientation. This step needs to be omitted or automated. Here we will investigate different approaches (e.g., statistically predicting point locations based upon prior datasets, atlas development, principal component analyses) to automate the neural orientation step.

Objective 3: Both knees of MOST participants (n=+2000) were previously imaged using Quantitative CT (QCT). As well, pain was scored using the Western Ontario McMasters Osteoarthritis Index (WOMAC) [2]. We will use our automated tool to determine depth-specific patellar BMD of all participants (+4000 knees). BMD measures will then be related to clinical measures of pain using multivariate analysis of covariance (MANCOVA) [2].

Anticipated Conclusions

This research will help in further understanding the role of subchondral bone in OA progression as well as pain pathogenesis. As pain is a determining factor in patients seeking medical care, it is important to understand the contributing factors to OA related pain as this will help guide clinicians in facilitating better preventative and corrective measures for patients.

References

[1] Burnett et al., 2013; [2] Burnett et al., 2016; [3] Johnston et al., 2010

Figures

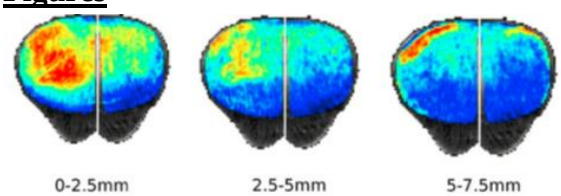

Fig 1. Depth specific analysis of average patellar BMD in participant with OA by Burnett et al. [1]

Do hip fracture patients experience asymmetrical bone loss after fracture?

Rachel M. DiMaio[1], Danielle E. Whittier[1], Steven K. Boyd[1]
[1]McCaig Institute for Bone & Joint Health, Cumming School of Medicine, University of Calgary, Calgary, AB

Introduction

An ongoing study conducted at the Bone Imaging Lab is investigating the use of a novel imaging technology, high-resolution peripheral quantitative computed tomography (HR-pQCT), for predicting the risk of hip fracture. HR-pQCT has the potential to be a more effective clinical tool for predicting fracture risk because it is able to capture compartmental density and bone microarchitecture parameters that the current standard, dual x-ray absorptiometry, cannot[1]. The study, however, is retrospective and scans are acquired 3-6 months following hip fracture. This presents possible complications because reduced mobility and uneven loading between the fractured and non-fractured side following fracture could adversely impact bone at the scan site (the distal tibia) and lead to deficits post-fracture. The aim of this project is to determine the extent to which reduced mobility leads to bone loss after hip fracture, and if there is a relationship between the magnitude of bilateral differences and magnitude change in the patient's mobility after fracture.

Methods

A subset of hip fracture patients with both tibias scanned using HR-pQCT (N=34 out of 73) were used in this study. Eleven HR-pQCT parameters capturing bone density, microarchitecture, and biomechanical properties were considered in the analysis. To reduce the impact of multiple comparisons, covariates were identified and removed. A paired sample t-test, or Wilcoxon test if non-normally distributed, was used to compare the fractured and non-fractured side parameters. The Benjamani-Hochberg method was used to adjust the p-values for multiple comparisons with a significance level of $p<0.05$[2]. Patient mobility before and after the fracture was captured as a score on a scale from 1 to 10 using a previously reported mobility scoring system. Then Spearman and Pearson correlation coefficients were used to measure the relationship between bilateral bone differences and the patient's change in self-reported mobility score.

Results

After adjustment for multiple comparisons, only cortical bone mineral density was significantly lower on the fractured side compared to the non-fractured side. None of the correlation coefficients between the bilateral differences and the change in mobility were large or significant ($R<0.35$).

Conclusions

Reduced mobility did not lead to large bilateral differences in bone deficits following hip fracture, and no correlation was found between the self-reported change in mobility and magnitude of bilateral differences in bone properties. This suggests that retrospective data can be used to determine risk factors for fracture.

References

[1] Nishiyama K and Shane E (2013) *Curr Osteoporos Rep.* 11(2):147-155.
[2] Whittier DE et al (2020) *Osteoporos Int.* 31:1607-27

Figure

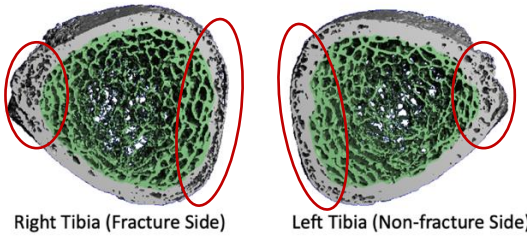

Figure: HR-pQCT scans of the right and left tibia of the hip fracture patient that had the largest bilateral difference in cortical bone mineral density, visible as a greater amount of porosity. Cortical bone is shown in grey and trabecular bone in green.

Design and Construction of a Passive Motion Device for Dynamic CT Scans of the Trapeziometacarpal Joint

Kendra Wang[1,2], Michael T. Kuczynski[1,3], Sarah L. Manske[1,3,4]

[1]McCaig Institute for Bone and Joint Health, Cumming School of Medicine, University of Calgary, Canada
[2]Biomedical Engineering Undergraduate Program, Faculty of Engineering, University of Waterloo, Canada
[3]Biomedical Engineering Graduate Program, Schulich School of Engineering, University of Calgary, Canada
[4]Department of Radiology, Cumming School of Medicine, University of Calgary, Canada

Introduction

Dynamic CT is a relatively new imaging technique that incorporates four dimensions (three spatial dimensions and time) and can be used to produce dynamic visualizations of bones and joints. [1] Dynamic CT can be used to study joint biomechanics. However, image acquisition and analysis protocols have not been validated. Thus, the purpose of this project was to design a passive motion device to facilitate motion of cadaveric trapeziometacarpal (TMC) joints to establish a dynamic CT imaging protocol and validate analysis tools.

Methods

Functional design requirements included: steady and natural movement of the thumb, control of the thumb's angular speed and joint angle, non-invasive methods to secure the hand, omitting radiopaque components (especially metal) from the scanning field of view. The passive motion device was designed using Fusion360 and consisted of 3D printed parts. (Fig. 1) To electrically power and control the device, a servo motor (Adafruit TowerPro MG995R), and an Arduino Uno microcontroller were used. The servo motor powered a two-member linkage joined by smooth pin joints to move the thumb in a radial abduction-adduction movement. Software to control the servo motor was developed in the Arduino language (C/C++) and a user interface was designed using Processing to control servo speed and angle.

Results

The device was tested *in-vivo*, and it proved to effectively move the thumb in a radial abduction-adduction movement. The design successfully met all of the previously defined requirements and constraints. The device was able to move the thumb within the its full range of motion comfortably and at a steady speed. The device was used to scan 10 cadaveric hands, develop an optimal dynamic CT scanning protocol, and is currently being used to assess reproducibility of methods to quantify TMC joint biomechanics from dynamic CT.

Conclusions

A passive motion device was effectively designed and constructed to move the thumb in an abduction-adduction movement. The device was used for the development of a dynamic CT scanning protocol of the TMC joint with cadaveric hands. In the future, the passive motion device and imaging protocol can be used for *in-vivo* testing and imaging, and for studies about osteoarthritis in the TMC joint.

References

[1] K. Zhao, et al., J. Biomech. Eng. 137(7). 2015.

Figures

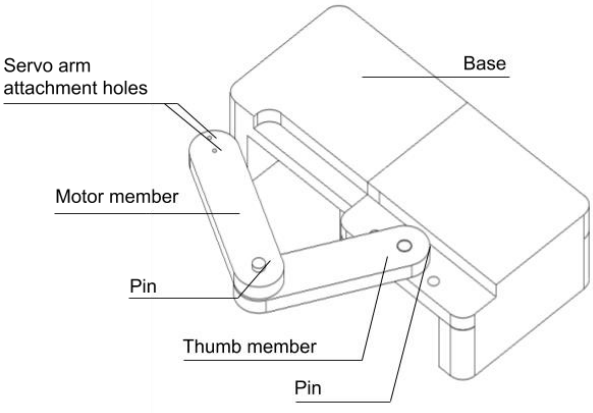

Figure 1. Diagram of the 3D-printed part assembly

4DCT Shows Improved Syndesmotic Motion after Flexible Fixation Compared to Rigid Fixation

Murray Wong, Charmaine Wiens, Kim Rondeau, Richard Buckley, Paul Duffy, Robert Korley, C. Ryan Martin, W. Brent Edwards, Prism Schneider
University of Calgary, Calgary, Alberta

Introduction

The syndesmosis is an important ligament complex which stabilizes the distal tibiofibular joint while allowing for small, physiologic motion. Syndesmotic injuries occur in up to one-quarter of all ankle fractures. When injured, malreduction of the syndesmosis is the most important factor contributing to inferior functional outcomes. Despite increasing awareness and mitigating efforts, malreduction of the syndesmosis remains common after both rigid screw fixation of the syndesmosis and flexible fixation, which uses a heavy suture to span the tibiofibular joint.

Conventional assessments of syndesmotic reduction do not account for normal syndesmotic motion with ankle range-of-motion (ROM). Four-dimensional computed tomography (4DCT) technology can image joints in real time and assess syndesmotic motion. The purpose of this study was to compare syndesmotic motion after rigid and flexible fixation.

Methods

Patients after rigid or flexible fixation underwent bilateral ankle 4DCT while moving between ankle dorsiflexion and plantarflexion. Measures of syndesmotic width including anterior (ASD), middle (MSD), and posterior (PSD) syndesmosis distances, as well as tibiofibular clear space (TFCS) and tibiofibular overlap (TFO), were automatically extracted from each 4DCT timepoint. Sagittal translation and fibular rotation were also recorded. Linear mixed effects models determined syndesmotic motion, defined as the change in syndesmotic measures with ankle ROM.

Results

Thirteen patients (seven rigid, six flexible) underwent 4DCT scans 12 months postoperatively. Uninjured ankles demonstrated significant decreases in ASD, MSD, PSD, TFCS, and syndesmotic area, as well as increased TFO, as ankles moved from dorsiflexion to plantarflexion ($p < 0.01$ for all measures). Rigid fixation demonstrated reduced motion compared to uninjured ankles in MSD, PSD, TFCS, and TFO ($p < 0.01$) (Figure 1). There were no differences in syndesmotic position or motion between flexible fixation and uninjured ankles.

Conclusions

Ankle plantarflexion leads to decreased syndesmotic width. Flexible fixation better restores normal syndesmotic motion compared to rigid fixation and maintains syndesmotic reduction. Applying these findings to clinical practice can reduce the rate of syndesmotic malreduction and improve patient outcomes after injury.

References

1. Weening & Bhandari. J Orthop Trauma 2005.
2. Naqvi et al. Am J Sports Med. 2012.
3. Laflamme et al. J Orthop Trauma. 2015.

Figures

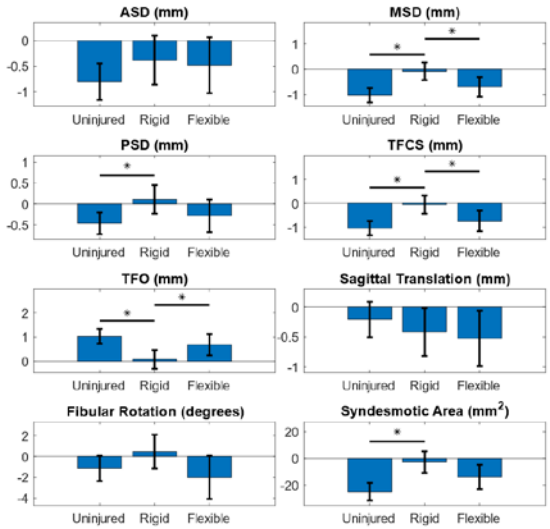

Figure 1: Syndesmotic motion by fixation type with 95% confidence intervals. *p<0.05

Modeling Participant-Specific Bone Atrophy During Spaceflight

Tannis D. Kemp[1,2], Bryce A. Besler[2], Leigh Gabel[2,3], Steven K. Boyd[1,2,3]

[1]Mechanical Engineering Graduate Program, University of Calgary
[2]McCaig Institute for Bone and Joint Health, University of Calgary
[3]Department of Radiology, University of Calgary

Introduction

Bone loss is ~10 times as fast during spaceflight as during menopause[1,2], presenting an accelerated method of studying bone loss on Earth. Participant-specific computational models of spaceflight related bone loss are yet to be developed but could predict bone atrophy or determine mechanisms of bone remodeling.

In the present study, we demonstrate how mathematical modelling[3] and numerical optimization may be used with *in vivo* high resolution peripheral quantitative computed tomography (HR-pQCT) to model space-related bone loss per individual.

Methods

A subset of participants (N=8) from the Canadian TBone Study – an investigation of long duration (~6 months) spaceflight and bone quality in astronauts – are used. Distal tibia HR-pQCT scans were taken at baseline before launch (L) and immediately upon return from spaceflight (R+0).

Individual bone atrophy rates are determined using level-set methods[4], least squares and gradient descent[5] to optimize the difference between simulated and ground-truth trabecular bone volumes. Since the simulated and ground truth bone volumes are identical at baseline, the R+0 data are used to compare the two methods.

Dice coefficient evaluates the difference between simulated and ground-truth bone volume data, where values closer to 1 indicate good agreement. Root mean square error (RMSE) measures the error in trabecular bone volume fraction (Tb.BV/TV, %), bone formation rate (BFR, %/day) and bone resorption rate (BRR, %/day) between simulation and ground-truth.

Tb.BV/TV, BFR and BRR are compared between ground-truth and simulation using a paired T-test with $\alpha<0.05$.

Results

The average Dice coefficient between ground-truth and simulated bone volumes was 0.86±0.03, indicating large overlapping volumes. The two techniques produced statistically similar Tb.BV/TV values ($p=0.92$, RMSE=0.28), but different BFR ($p<0.001$, RMSE=0.064) and BRR ($p<0.001$, RMSE=0.054) (Figure 1). This indicates that changes in morphology are captured by the simulation, but bone remodeling is not.

Conclusions

The technique presented in this work shows promise for modelling participant-specific bone atrophy during long-duration spaceflight. In the future, we will implement a strain-adaptive model to investigate the effects of microgravity (i.e. un-loading) on bone remodeling.

References

[1] Stavnichuk *et al* (2020) NPJ Microgravity
[2] Hannan *et al* (2010) JBMR
[3] Besler *et al* (2018) MICCAI-MSKI
[4] Sethian (1999) Level set methods and fast marching methods
[5] Kingma & Ba (2015) ICLR

Figures

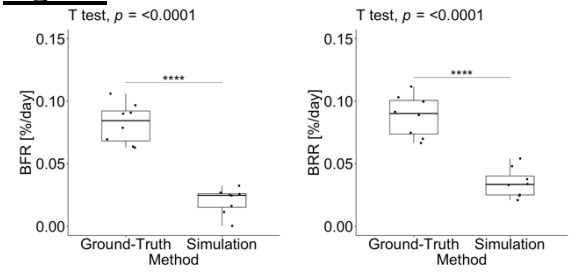

Figure 1. Bone Formation Rate (BFR, %/day) and Bone Resorption Rate (BRR, %/day) between L and R+0 determined from ground-truth HR-pQCT and simulated data. The simulation significantly underestimated both BFR and BRR.

Validating Periosteal and Endosteal Localization in the Femur of Clinical Computed Tomography Datasets

Aleena Abid[1], Bryce A. Besler[1], Nils D. Forkert[2], Steven K. Boyd[1]
[1]McCaig Institute for Bone and Joint Health; [2]Department of Radiology

Introduction

Osteoporosis is a disease where there is a gradual loss of bone density and microarchitecture, increasing the risk of fracture. To balance the loss of bone strength, the bone grows larger in diameter, thereby achieving a mechanical advantage by increasing the ability to withstand load, given the same amount of material. This happens at the periosteal surface (bone-soft tissue interface) and endosteal surface (cortical-cancellous interface) at the same time. Quantifying periosteal and endosteal expansion is critical for monitoring disease progression.

In this study, a periosteal and endosteal localization algorithm is validated. It is hypothesized that the periosteal and endosteal surface can be localized to within the nominal resolution of clinical computed tomography.

Methods

1 female cadaver, aged 72, was used for validation. The left proximal femur was previously imaged using high-resolution peripheral quantitative computed tomography (gold standard, HR-pQCT) and quantitative computed tomography (QCT). For HR-pQCT, the standard algorithm[1] was applied for periosteal and endosteal segmentation and manually corrected. For QCT, the proposed algorithm[2] was applied without manual correction. Following segmentation, the QCT data was aligned with the HR-pQCT data using intensity based image registration. Symmetric surface distances were computed for both the periosteal and endosteal surfaces at the HR-pQCT resolution. Average distance and percent of distances below the QCT nominal resolution are reported.

Results

The average surface error was 0.256 mm and 1.000 mm for the periosteal and endosteal surface, respectively. This is half and twice the size of a voxel in the QCT image. For the periosteal surface, 88.1% of errors were below the resolution (0.503 mm) of the QCT image. For the endosteal surface, 24.0% of errors were below the resolution (0.503 mm) of the QCT image.

Conclusions

The periosteal and endosteal surfaces can be accurately localized on the order of scanner resolution in clinical computed tomography. Localization of these surfaces allows new measurements of osteoporosis progression by explicitly tracking periosteal and endosteal expansion.

References

[1] Buie et al., Bone. 2007.
[2] Besler et al. Bone and Joint Enhancement Filtering. 2020 (In Print).

Figures

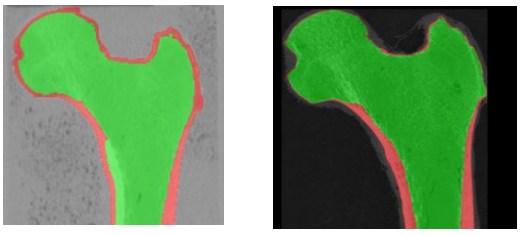

Figure 1: Combined endosteal (green) and periosteal (red) segmentation for QCT (right) and HR-pQCT (left) scans

Reproducibility of Trapeziometacarpal Joint Angle Measurements Using Dynamic Computed Tomography

Michael T. Kuczynski[1,2], Kendra Wang[2,3], Justin J. Tse[1,4], Sarah L. Manske[1,2,4]
[1]Biomedical Engineering Graduate Program, Schulich School of Engineering, University of Calgary, Canada
[2]McCaig Institute for Bone and Joint Health, Cumming School of Medicine, University of Calgary, Canada
[3]Biomedical Engineering Undergraduate Program, Faculty of Engineering, University of Waterloo, Canada
[4]Department of Radiology, Cumming School of Medicine, University of Calgary, Canada

Introduction

Osteoarthritis (OA) is a degenerative joint disease that commonly affects the joints of the hand, including the trapeziometacarpal (TMC) joint [1]. OA is considered a complex and multifactorial disease in which biomechanics plays a role [1]. Dynamic computed tomography (CT) can provide 3D representations of bone and joint motion over time. However, validation of several aspects of dynamic CT scanning of the TMC joint have not been well explored. Joint angles are often calculated using segment coordinate systems (SCS) manually defined from the joint anatomy. However, age and disease related joint degeneration may impact the reproducibility of this method and has not been validated for dynamic CT scans of the TMC joint. We present a reproducibility study to validate these manually defined TMC joint SCSs and their impact on resulting joint angle values.

Methods

Ten cadaveric hand specimens (50% female, age: 83.4±15.0) were obtained for scanning. Dynamic CT scanning was performed using 120kVp energy level, 100mA tube current, 4cm longitudinal coverage, 4vol/s gantry rotation, and 15s scan time. A custom passive motion device was used to move the thumb through a radial abduction-adduction movement. Due to limitations in dynamic CT image quality and coverage, static HR-pQCT scans were obtained from an XtremeCT2 scanner (Scanco Medical) to generate image masks and for SCS definition. Static CT images were segmented using a combination of global thresholds, binary morphological operations, and connected component labelling. Dynamic CT images were segmented using intensity-based sequential registration of static CT bone masks. Joint angles were measured using a joint coordinate system (JCS) representation [2]. SCS for each bone in the TMC joint were generated using anatomical features points [3] selected manually by three raters. Coefficient of variation and intraclass correlation coefficients were calculated to assess the accuracy of JCS position, orientation, and joint angle results.

Results

Preliminary results shows that JCS axes are almost perfectly orthogonal when using the current instruction set for anatomical landmark selection (RMSE = 0.00065).

Conclusions

Tools to quantify TMC joint biomechanics from dynamic CT scans must first be validated. This study provides the groundwork for future studies that will assess the relationship between joint structure and function in osteoarthritic TMC joints using dynamic CT.

References

[1] Marshall, M., *et al*. Nat. Rev. Rheumatol. 2018.
[2] Grood, E.S., Suntay, W.J. J. Biomech. Eng. 1983.
[3] Chèze, L., *et al*. CMBBE. 2009.

Figures

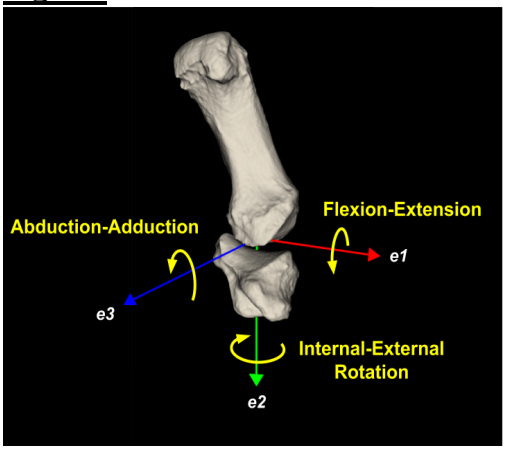

Figure: TMC JCS defined on a HR-pQCT image.

Ice-Skating Temporal Events Detection Using Inertial Sensors Data

Aminreza Khandan, Ramin Fathian, Jason Carey, Hossein Rouhani
Mechanical Engineering, University of Alberta, Edmonton, Canada

Introduction

Accurate assessment of an ice skater's motions during training sessions and matches helps coaches to monitor the player performance continuously [1]. The first step toward developing a technology assessing hockey player performance is to detect temporal skating events precisely. Our objective is to develop original methods to detect skating events using Inertial Measurement Units (IMU) data.

Methods

We recruited four participants (age: 28 ± 1 years, body height: 176±7 cm, body mass: 77±8 kg) able to skate on the synthetic ice comfortably. We placed four IMU sensors (Xsens Technologies, NL) on the two skates and the lower legs of the participants. They were asked to skate forward on the indoor synthetic ice rink five times while the IMUs and two pressure insoles recorded their motions and ground reaction forces respectively. The two pressure insoles (Pedar®, Novel, DE) were placed into their skates and were used as a gold standard for temporal event detection. To detect skate strike (SS) and blades-off (BO) in 20 trials (five trials of each participant), six original methods were developed and implemented (Table 1). We then validated the detected events against the same temporal events detected using the pressure insoles, with a 5 N threshold.

Results

The mean and standard deviation of the errors indicate that the best methods are Method II (0.06 ± 0.31 sec) and Method IV (-0.08 ± 0.16 sec) in detecting SS. In detecting BO, however, Method I (0.00 ± 0.15 sec) and Method V (0.01 ± 0.13 sec) are the most effective ones.

Conclusions

Our observation shows that inertial sensors enable us to detect skating temporal events with 0.01 sec error and with relatively high precision. Also, the errors imply that the most informative signal is skate acceleration and the signals obtained from shank and pelvis are not ideal for getting temporal events. This inference confirms the results of Mariani et al [2] completed on gait analysis event detection in ice skating applications. Finally, the early results imply that we achieved higher accuracy and precision to obtain BO compared to SS detection. The next step is to recruit more participants to get a more extensible conclusion.

References

[1] E. Papi, D. Osei-Kuffour, Y.-M. A. Chen, and A. H. McGregor, "Use of wearable technology for performance assessment: a validation study," *Med. Eng. Phys.*, vol. 37, no. 7, pp. 698–704, 2015.

[2] B. Mariani, H. Rouhani, X. Crevoisier, and K. Aminian, "Quantitative estimation of foot-flat and stance phase of gait using foot-worn inertial sensors," Gait Posture, vol. 37, no. 2, pp. 229–234, 2013.

Figures

Table 1. Description of the temporal event detection methods

	Signal used	Blades off (BO)	Skate Strike (SS)
Method I	Skate Vertical acceleration	Positive spikes in the graph	Minimum between two consecutive BOs
Method II	Skate horizontal acceleration	Large positive spikes	The maximum between two consecutive BOs
Method III	Skate Vertical velocity	Positive spikes	Local maximums
Method IV	Skate total acceleration	The minimum before the big positive spikes	The maximum between two consecutive BOs
Method V	Shank vertical angular velocity	Negative spikes	Minimum between two consecutive BOs
Method VI	Shank vertical angular velocity	The minimum before the big spike instants	Minimum between two consecutive BOs

Negative Pressure Ventilation in the Shortfall of COVID-19 Ventilators: A Review

S. Lu[1,2], V. Maslieieva[1], I. Ariza[2], M. Ungrin[1,2,3]
[1]Department of Comparative Biology and Experimental Medicine, Faculty of Veterinary Medicine, University of Calgary, Calgary, Alberta, Canada; [2]Biomedical Engineering Calgary, University of Calgary, Calgary, Alberta, Canada; [3]Alberta Children's Hospital Research Institute, University of Calgary, Calgary, Alberta, Canada

Introduction

Mechanical ventilation provides breathing support for patients with respiratory disorders. The COVID-19 pandemic has led to a substantial increase in the global need for ventilators. In the case of large-scale ventilator shortages, particularly in regions that may not have the economic resources for manufacturing conventional positive pressure ventilation (PPV) systems, negative pressure ventilation (NPV), exemplified by iron lungs of the polio era, offers the potential for a simple low-cost and mass-manufacturable alternative. While bulkier and less convenient, NPV systems do not directly contact the air breathed by the patient, therefore simplifying manufacturing and quality control requirements greatly.

Methods

We reviewed the applications, implications and mechanism of NPV in contrast with conventional PPV. We synthesized the available information on potential complications of NPV in order to provide a foundation for its safe and efficient implementation. A comprehensive electronic search of literature was conducted in various databases, and relevant studies reporting on NPV were extracted for full text review.

Results

Several studies evaluating the use of NPV in animal populations as well as patient populations have reported improved oxygenation and increased cardiac output[1-3], however, additional research is required. While NPV systems may be inherently less likely to induce barotrauma, they are not without risks and potential complications, including pulmonary edema, pneumothorax, and musculoskeletal pain[4]. A synthesis of these findings suggest that while NPV has significant potential, precautions need to be taken as to reduce the risk of possible complications.

Conclusions

While select studies suggest that NPV systems may have the potential to enhance oxygen delivery and hemodynamics in comparison to PPV systems under some circumstances, substitution of experimental NPV systems for conventional PPV medical devices would not be advised without further research. However, locally manufactured NPV systems may provide a last-resort option in situations of desperate need where no other alternatives are available. The initial testing of such an experimental NPV prototype has been underway, and preliminary results will be reported.

References

1. Grasso F, Engelberts D, Helm E, et al. Negative-pressure ventilation: better oxygenation and less lung injury. *Am J Respir Crit Care Med*. 2008;177(4):412–418.
2. Raymondos K, Molitoris U, Capewell M, et al. Negative- versus positive-pressure ventilation in intubated patients with acute respiratory distress syndrome. *Crit Care.* 2012;16(2):R37.
3. McBride WT, Ranaldi G, Dougherty MJ, et al. The hemodynamic and respiratory effects of cuirass ventilation in healthy volunteers: part 1. *J Cardiothorac Vasc Anesth.* 2012;26(5):868–872.
4. Gorini M, Ginanni R, Villella G, et al. Non-invasive negative and positive pressure ventilation in the treatment of acute on chronic respiratory failure. *Intensive Care Med*. 2004;30(5):875–881.

IMU based finger band remote controller

A preliminary method towards developing assistive data gloves for stroke rehabilitation

Alhamd Khan[1], Michael R. Smith[1, 2], Sean Dukelow[3]
[1]Electrical and Computer Engineering, [2]Radiology, [3]Clinical Neurosciences, University of Calgary

Introduction

In the long run, assistive tools that can be easily incorporated into practice for pursuing daily life activities would assist in reducing mobility difficulties experienced by patients. Virtual reality-based (VR) data gloves have embedded sensors that measure movement-related data which makes them encouraging tools for monitoring physical activity and providing assessment of patients suffering from disabilities associated with upper extremities post-stroke. [1] This preliminary investigation uncovered issues relevant to developing a VR-based data glove for stroke rehabilitation.

Methods

The wearable device makes use of a sensing devices worn over the user's index finger (Fig - MASTER SIDE). Each gesture or movement of the finger activates a specific functionality of the appliance (SLAVE SIDE): e.g. finger up and down corresponding to volume up, volume down. The teensy 3.2 microcontroller sends appropriate Wi-Fi control codes to the slave controller on encountering changes in the resistance values of a flex sensor; and estimates pitch and roll from the acceleration determined from the 3 axis IMU sensor.

Results

The wearable device incorporates the combination of flex sensor and IMU which provides an initial pathway towards the working of a data glove for stroke rehabilitation. The device was able to switch TV channels, control the volume and power on/off the TV by moving the index finger to specific angles**.** The project helped in the understanding of the signal processing necessary for the IMU and flex sensors undertaking vertical and horizontal motion.

Conclusions

We have made a gesture recognition empowered, wearable finger band remote controller for patients with mobility issues to help them in controlling infrared enabled appliances. The experiment showed the importance of improving the repeatability of gesture interpretation for patients with unsteady hands. The project will be extended to provide an improved glove capable of providing the data to assess changes in patient's mobility following the use of VR games designed to facilitate upper extremities rehabilitation post stroke.

References

[1] Thielbar, K et al., "Training finger individuation with a mechatronic-virtual reality system leads to improved fine motor control post-stroke", Journal of NeuroEngineering and Rehabilitation, vol. 11, no. 1, p. 171, 2014.

Figures

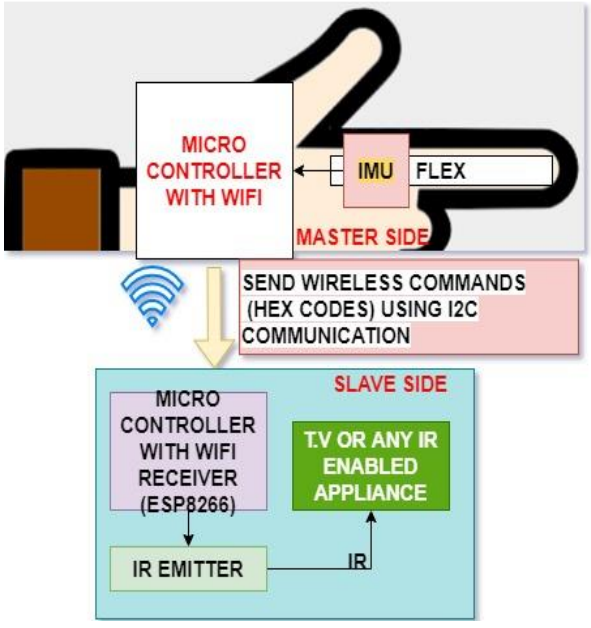

Device configuration - Master side (top) comprising of a teensy 3.2 microcontroller, a Bno055 9-DOF IMU, a flex sensor, and Slave side (bottom) comprising of an infrared emitter, and a Teensy 3.2 micro controller which manages the processing of the data received from the master side.

Development of a multifunctional electrical cuff for peripheral nerve monitoring and regeneration.

Alec Lamb[1], Isaac Adan Acosta Calvillo[2], Colin Dalton[1,2], Kartikeya Murari[1,2,3]
[1]Electrical and Computer Engineering Department, [2]BME Graduate Program, [3]Hotchkiss Brain Institute
Department of Electrical and Computer Engineering, ICT 402, 2500 University Drive NW, Calgary, AB T2N 1N4

Introduction

Peripheral nerve injury (PNI) affects more than 20 million people in the USA alone.[1] Recovery from such injury is often poor and incomplete, burdening healthcare systems and economies with costly and lengthy treatments. Electrical stimulation (ES) is a promising method in development for promoting nerve regeneration after PNI.[2] Despite the potential benefits of modern ES interventions, researchers studying such regeneration are often limited to evaluating outcomes at the end of treatment, when it may be too late to address any issues. This in turn prevents the optimization of the ES process, and thus prevents proactive management of nerve regeneration. To overcome these issues, the goal of this project is to develop an implantable cuff that encircles a PNI site and integrates electronics on a printed circuit board (PCB) capable of both providing ES, and concurrently monitoring nerve regeneration via impedance measurements.

Methods

Project methods involve initiation and optimization of the cuff's electrical design. This includes identifying key performance indicators in literature for testing and implementation, and subsequently directing the design of a circuit prototype. This design stage was defined by the goal of creating a PCB model of an embedded circuit modulated by a single microcontroller via the Altium Designer CAD software. This microcontroller is to modulate the delivery of ES to the nerve and support the collection of impedance data to track nerve recovery. To ensure high signal fidelity, low power operation for efficiency, and small size for future implantation objectives, specific selections of components and PCB design principles were required.

Results

Performance indicators obtained from literature review include important operational metrics for the maximization of circuit efficacy, accuracy, and safety; such as minimizing current amplitude and utilizing electrochemical electrode characterization. The final PCB model occupies a 12.55 mm by 5.85 mm area. It completes its intended function with a central PIC microcontroller interfacing directly with electrodes to deliver ES, while also utilizing differential voltage measurements alongside an operational amplifier (allowing the delivery of a sinusoidal current) for the purpose of collecting impedance data. Four separate electrode sites are available for selection through two analog switches.

Conclusions

These findings demonstrate a valid electrical-based approach to multifunctional electric cuffs, enabling further research and development on nerve regeneration and monitoring.

References

[1] Lundborg et al, J. Peripheral Nervous System, vol. 8, no. 4, pp. 209–226. [2] Wang et al, J. Neurotrauma, vol. 26, no. 4, pp. 641–649.

Figures

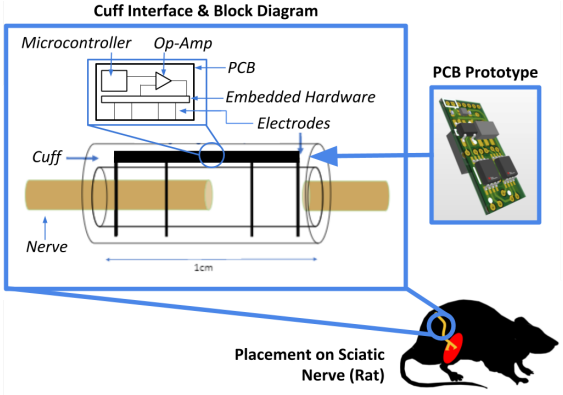

Fig. 1 Contextual overview of the electric cuff placement and design.

Selection of an IoT Data Analytics Platform for a Wireless Sensor Technology for Tele-Rehabilitation Assessments of Remote Wheelchair Users

Md Manirul Islam, Jason Jicheng Zhao, Martin Ferguson-Pell, Ph.D., and Greg Kawchuk, Ph.D.
Rehab Robotics Laboratory, Faculty of Rehabilitation Medicine, University of Alberta,
2-545 Edmonton Clinic Health Academy, Edmonton, AB T6G 1C9, Canada.

Introduction

About 18% of Alberta's populations live in rural areas. It is challenging for them to access rehabilitation assessments as there is a lack of available specialists. They have to travel long distances often in dangerous winter conditions. The Tele-Rehabilitation 2.0 platform developed by our lab connects a specialist clinician at an urban site and a generalist clinician at a rural clinic setting. Experts in wheelchair assessment are particularly scarce in rural Alberta. Our lab has developed a simple, low-cost device named Sagitta [1] that can be attached to wheelchair for measuring exertion data such as cadence, velocity, power, distance-travelled, acceleration, propulsion force, energy, and active time [2]. Sagitta transmits the real-time exertion data to a dashboard for the urban specialist's assessment while the remote patient propels their wheelchair. The urban specialist can activate and control data acquisition, and then review the generated dashboard's data in real-time for the assessment of remote wheelchair users.

Methods

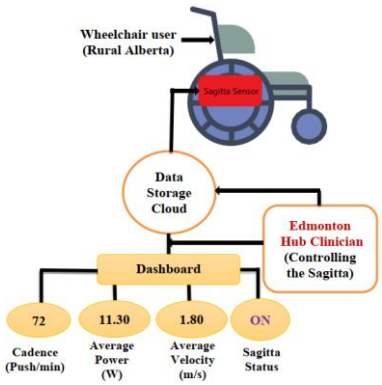

Figure 1: Schematic of wireless Sensor Technology for real-time assessments of remote wheelchair users.

We developed dashboards using 3 open-source IoT data analytics platforms: ThingSpeak, Adafruit, and the Blynk App. They enable uploading and storing data for interpretation by the specialist in real-time. Sagitta's firmware was developed to enable wireless communication with each dashboard and then a layout was designed to present the data from Sagitta and provide the necessary activation mechanism (Voice, Dashboard Switch).

Results

To evaluate the performance characteristics of these dashboards, a rubric was developed (Table 1). The Adafruit dashboard is most appropriate for this clinical application because of its excellent response time and ease of use in controlling the sensor.

Table 1: Performance comparison of 3 Dashboards

Performance Analyze	ThingSpeak	Adafruit	Blynk App
Data upload time	15 s	5 s	1s
Device control time	(10-15) s	1s	1s
Response	Less fast	Faster	Faster
Data Storage	Yes	Yes	No
Data Export	Yes	Yes	No
Stream data	No	Yes	No
Graphics	Yes	Yes	No
Channel	8	10	Limited

Conclusions

Based on our evaluation, the Adafruit dashboard with the sensor-technology provided the most effective combination of features required for our wheelchair application. A specialist clinician from anywhere can use this novel IoT based wireless sensor-technologies to assess remote wheelchair users accurately. This technology will reduce access barriers for patients in rural communities and seniors in long-term care facilities.

References

[1] John Christy Johnson and Martin Ferguson-Pell "Validation of a wheelchair Fitbit Wearable Redliner against Smartwheel", *20th Annual Biomedical Engineering Conference*, October Banff 2019.

[2] Liping Qi, Martin Ferguson-Pell, Zohreh Salimi, and Ailar Ramadi, "Wheelchair users' perceived exertion during typical mobility activities", *Spinal Cord* **53,** 687–691; doi:10.1038/sc.2015.30.

Comparing 2D and 3D AC Electrothermal Device Models

Graciela Moscoso[1,2], Stirling Cenaiko[2,3], Thomas Lijnse[4], Colin Dalton[4,5]
[1]Department of Mechanical and Manufacturing Engineering, University of Calgary [2]Centre for Bioengineering Research and Education, University of Calgary [3]Department of Chemical and Petroleum Engineering, University of Calgary [4]Biomedical Engineering Graduate Program, University of Calgary [5]Department of Electrical and Computer Engineering, University of Calgary

Introduction

Lab-on-a-chip (LOC) devices are capable of performing small scale laboratory functions, such as disease detection, in a very short amount of time. In medical settings, the time spent obtaining lab results, to provide patients with the correct treatment, can seriously impact the extent to which they are affected by their condition. Electrokinetic (EK) microdevices manipulate fluids through induced electric charges caused by an applied electric field. **[1]** Unlike other EK techniques, AC Electrothermal (ACET) devices can be used with high ionic strength fluids, such as biofluids, which makes these devices suitable for LOC applications. **[2]** The design of these devices still requires optimization through accurate and precise device modeling before ACET can be used in current microdevices. Previous limitations in computational capabilities made 3D models difficult to create, and previous studies, using a highly simplified model, have found the differences between 2D and 3D models to be negligible, **[3]** which has contributed to a lack of exploration of 3D ACET models. Improved computational resources now enable full 3D models to be simulated. In this work, 2D and 3D models are compared to determine if discrepancies arise from model differences. Changes to modelling techniques for future work are then suggested, to improve accuracy.

Methods

In this research a 3D model and a corresponding 2D model of an ACET device were created using a commercial multiphysics simulation package (COMSOL MA, USA). Both the 3D and 2D model included heat transfer, electrostatics, and laminar flow modules. The models also included no slip boundary conditions on channel walls and were built using the finer mesh setting. The average outlet flowrate and maximum fluid temperature of the 3D and 2D model were compared, as ACET systems are directly linked to the magnitude of the thermal gradient.

Results

It was found that for a channel with a length and height of 310μm and 250μm respectively, 2D and 3D models yield flow rate differences of 12.6% (observed at a channel width of 6000μm), or greater. This is likely due to no slip boundary conditions on the front and back channel walls, which only exist in the 3D model.

Conclusions

Producing accurate models is vital to optimizing the design of ACET devices for LOC purposes. Using modern computational resources, we can model microdevices more accurately prior to fabrication and testing, facilitating advancement in the design of these devices, improving our understanding of key design parameters.

References

[1] Lijnse, T. et al., SN Applied Sciences 2020. **[2]** Salari, A. et al., Micromachines 2019. **[3]** Yuan, Q. et al., Springer 2013.

Figures

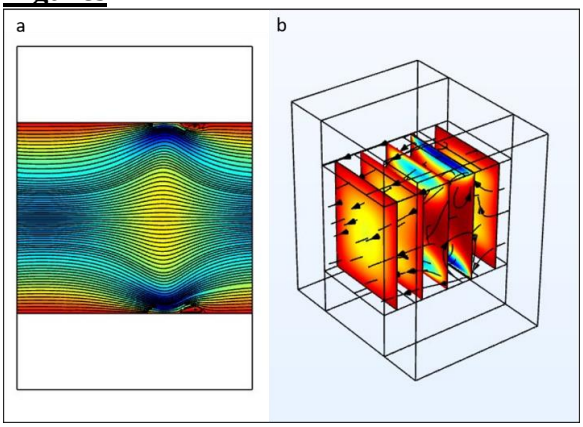

Figure/Table: a Fluid flow profile of a 2D planer electrode ACET model in the x-y plane. **b** Fluid flow profile of a 3D planar electrode ACET model with 4 channel walls.

Computer Algorithm for Automated Detection of Ventilatory Thresholds from Cardiopulmonary Exercise Testing Data

James W. Gardner[1], Jordan B. Swanson[2], Karen D. Kendall[2] and Marc J. Poulin[2]
[1] Dept of Science, University of British Columbia, Vancouver British Columbia
[2] Dept of Physiology & Pharmacology, and Clinical & Translational Exercise Physiology Laboratory, Cumming School of Medicine, University of Calgary, Calgary Alberta

Introduction

Ventilatory thresholds are common metrics used in exercise physiology that convey information about physiological mechanisms underlying the cardiorespiratory response to exercise. They are used as indicators of the boundaries between light, medium, and heavy exercise, as well as measurements of relative exercise intensity. Traditionally, these thresholds are selected by trained examiners using visual inspection of breath-by-breath data from maximal exercise tests. The goal of this project is to develop a computer program to automate this process in order to reduce bias, increase replicability, and reduce burden on researchers.

Methods

Previous research shows that computerized methods can perform the gold-standard V-slope method of determining thresholds, and that these methods are reasonably accurate. We sought to automate and modify these methods by implementing a segmented linear regression, similar to those described by Beaver et al. (1986) and Orr et al. (1982), in conjunction with the Local Outlier Factor method of anomaly detection, to select thresholds. For some panels, a polynomial regression scheme similar to a method detailed by Fukuba et al. (1988) was be used to determine thresholds. In the current early development stage, breath-by-breath data from *Brain in Motion Study* participants (n=8) are being used to optimize the program to produce results closely matching thresholds selected by two trained examiners from respiratory breath-by-breath data of six cardiorespiratory exercise tests. The long-term goal is to test this program against a larger set of participant data, comparing automated results to examiner picked values.

Results

The Python program is currently in the development stage, but currently is able to take output csv files from cardiopulmonary exercise tests and performs appropriate analysis for each of the six panels. A large-scale comparison to examiner picked thresholds has yet to be completed. However, initial comparisons show good agreement between the algorithms and examiners. We expect that our program will eventually be able to reliably pick accurate threshold values.

Conclusions

This computerized method should aid researchers by reducing workload and in creating more objective, replicable measurements that maintain agreement with previous scientific literature. The next step in this project is to perform a larger scale comparison between program-picked values and examiner-picked values. Hopefully, this will confirm the validity of the program.

References

Beaver, W. L., Wasserman, K., & Whipp, B. J. (1986). A new method for detecting anaerobic threshold by gas exchange. *J. Appl. Physiol. 60:* 2020-27.

Orr, G. W., Green, H. J., Hughson, R. L., & Bennett, G. W. (1982). A computer linear regression model to determine ventilatory anaerobic threshold. *J. Appl. Physiol. 52:*1349.

Fukuba, Y., Munaka, M., Usui, S., & Sasahara, H. (1988). Comparison of objective methods for determining ventilatory threshold. *Jap. J. Physiol. 38:*133-144.

Acknowledgements: NSERC Brain Create Program.

Benefits of Cyclist Green Waves using Wearables

Tyler Yip[1], Andrew J. Pohl[2], Elizabeth Stulen[2], Reed Ferber[2,3,4,5]
[1]Schulich School of Engineering, University of Calgary, Calgary, Alberta, Canada
[2]Faculty of Kinesiology, University of Calgary, Calgary, Alberta, Canada
[3]Cumming School of Medicine, University of Calgary, Calgary, Alberta, Canada
[4]Faculty of Nursing, University of Calgary, Calgary, Alberta, Canada
[5]Running Injury Clinic, Calgary, Alberta, Canada

Introduction

A barrier to the adoption of cycling as a commuting option is the inconvenience of frequent stopping at intersections. Green wave systems address this issue by synchronizing traffic lights to give users consecutive green lights, eliminating stopping while maintaining rider safety provided riders maintain a specific speed[1]. Green waves are common in motorist traffic systems; however, few studies have considered their use for cyclists. This study examines the benefits of implementing a green wave system in Calgary, Alberta.

Methods

Speed and global positioning data recorded by Garmin wearables were retrieved from 2,260 rides submitted voluntarily from 52 participants to the We-TRAC Citizen Science program. An average of 1,417 samples were recorded per ride. Using a geofence, rides were filtered to those within the 5th St SW and 12th Ave SW corridors because these routes feature commuter-friendly bike lanes. Intersection center points along each route were identified manually before applying rectangular bounding boxes to each intersection. Intersection movement status was defined as stopped when a participant's speed measured below average walking speed[2] (1.4 ms^{-1}) within the bounding boxes. Intersection delay was calculated by computing the elapsed stop time and mapped to identify the most disruptive intersections. Green wave speed (GWS) was simulated by computing the average speed after eliminating sections where a participant was stopped at each intersection.

Results

In 68.8% of rides, participants were not required to stop despite the absence of a green wave system. Of the 31.2% of rides where participants experienced a delay, there was a mean 9.56% increase on average speed attributed to the presence of a green wave system (GWS: 4.24 ms^{-1}, ±1.18; non-GWS: 3.87 ms^{-1}, ±1.12). 5th St SW and 12th Ave SW had an average intersection delay of 15.2 s and 14.6 s respectively.

Conclusions

This study explores an inexpensive optimization of existing infrastructure to promote sustainable transportation in downtown Calgary. Future research should investigate the experimental performance of cyclist green waves at reducing delays and improving rider experience.

References

[1] Apostola, T. (2014). A traffic signal optimization method for balancing the interests of cyclists and motorized traffic. *Master's thesis, Delft University of Technology*., 1-23.

[2] Browning, R. C., et Al. (2006). Effects of obesity and sex on the energetic cost and preferred speed of walking. *J. Appl. Physiol., 100*(2), 390-398.

Figure

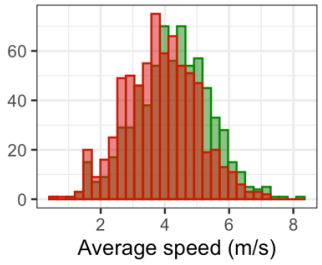

Figure 1: Distribution of average speed with (green) and without (red) a simulated green wave system for cyclists that were required to stop at an intersection.

Effect of Axillary Crutch Length on Latissimus Dorsi Activation During Swing-Through Gait

Monica Russell[1], Gregor Kuntze[1,2], Janet Lenore Ronsky[2,3], Ranita Harpreet Kaur Manocha[2,4]
1. Faculty of Kinesiology, University of Calgary
2. McCaig Institute of Bone and Joint Health, University of Calgary
3. Department of Mechanical and Manufacturing Engineering, University of Calgary
4. Department of Clinical Neurosciences University of Calgary

Introduction

Crutch-assisted gait results in repetitive upper extremity (UE) weight-bearing, which may result in pain or injury. If UE injury occurs, it may worsen a crutch user's functional impairment. Proper crutch fitting may be important to mitigate this risk. There have been no studies assessing the impact of axillary crutch length on UE muscle activation patterns. The objective of this study was to analyze latissimus dorsi activation patterns and intensities during axillary crutch-assisted gait when crutches are fit appropriately and inappropriately.

Methods

Fifteen able-bodied adult males (mean±SD age: 24±5.79, BMI: 24.9±2.40) were fit with crutches using standard guidelines, crutches 5 cm longer, and crutches 5 cm shorter. Participants performed 15 gait cycles with each crutch length. Bipolar electromyography (EMG) electrodes were applied to the skin directly above the latissimus dorsi muscle. Wavelet analysis[1] was used to analyze the EMG data. Statistical parametric mapping (SPM) analyses were performed to identify regional differences in EMG patterns. A one-way repeated measures ANOVA test was conducted for the EMG peak intensity values and their locations. Alpha was set at 0.05. Post-hoc power was also calculated.

Results

No regional differences in latissimus dorsi activation pattern were observed between crutch lengths in the SPM analysis ($p>0.05$). No differences between crutch lengths were observed in latissimus dorsi peak activation intensity ($p>0.05$) or peak intensity location ($p>0.05$). Contour maps for a single subject are shown in Figure 1.

Conclusions

The latissimus dorsi is most active during crutch stance phase, likely due to its action as an accessory shoulder extensor in order to support a crutch user's body weight during the body swing phase. Crutch length did not affect the activation of this muscle during assisted gait.

References

1.Von Tscharner, V. Intensity analysis in time-frequency space of surface myoelectric signals by wavelets of specified resolution. In: *Journal of Electromyography and Kinesiology*. 2000. 433–45. doi:10.1016/S1050-6411(00)00030-4

Figure

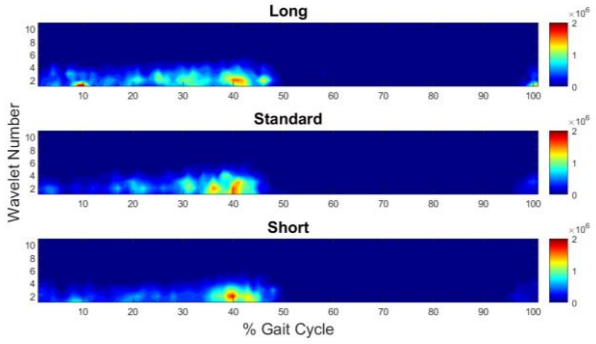

Fig. 1: Contour maps of the left latissimus dorsi muscle for one subject, where 0% of gait cycle represents initial crutch contact and 100% represents the next ipsilateral crutch contact. Areas of high muscle activation are shown in red and low activation in blue.

Stroke Patient Body Position Analysis Using Pressure Sensor Array Data

Aakash Bhatt, Ayesha Farooq, Thomas Truong, Svetlana Yanushkevich
Biometric Technologies Laboratory, ECE Department, University of Calgary, Canada

Introduction

A stroke can occur when there is a sudden interruption in the blood flow going to the brain causing cell death. Thus, it is crucial that stroke be detected with minimal delay to mitigate chances for severe post-stroke conditions. One symptom of stroke is hemiparalysis: paralysis in one side of the body. In our study we hypothesize that asymmetry in movement can be detected by analyzing pressure data recovered from a pressure mattress in the form of time series. Irregularities in movement may be represented in the pressure sensor readings which can be then used in machine learning techniques to classify patient position as either lateral or supine. The results obtained can then be used in an analysis to detect the type of stroke.

Methods

Data was collected from 20 post stroke surgery patients by the Ward of 21st century at the Foothills hospital. An XSENSOR pressure mattress was used with 48X118 sensors at a sampling rate of 1 per minute. 39,609 pressure frames were manually classified into three classes: supine, lateral, and no patient. The data was separated into a training set, validation set and a testing set, which were kept constant for all experiments. Support vector machine (SVM) and convolutional neural networks were used as the classification algorithms. To address the imbalance in the data set, over-sampling and under-sampling methods were used. For the final evaluation four different metrics were calculated: accuracy, precision, recall and F1 score.

Results

Both SVM and CNN classification were effective in classifying supine and lateral positions with high accuracy (68% and 66% respectively). SVM with random over sampling performed better in all metrics as compared to the CNN model. However, both algorithms had a high degree of misclassification between the supine and lateral positions which may be due to the over-representation of the supine class and low number of samples. More data collection is underway to improve the accuracy.

Conclusion

SVM with ROS provided the best results with low variance as compared to the CNN model. Further developments can be implemented to improve the results as there is still misclassification of the supine position as lateral. This builds a groundwork for stroke detection, where asymmetry in the left and right side of the body needs to be analyzed. A system that can effectively separate when a patient is in supine position can be used to preprocess data in long term patient recordings.

References

[1] V. Davoodnia, S. Ghorbani, and A. Etemad, "In-bed Pressure-based Pose Estimation Using Image Space Representation Learning," 2019.[Online]. Available: http://arxiv.org/abs/1908.08919

Figures

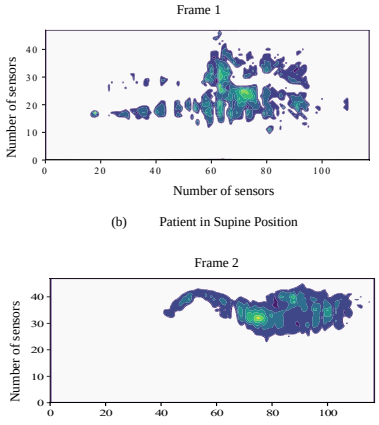

(b) Patient in Supine Position

Figure 1: Example of colour maps used in classification. The sensors are located 2.54 mm apart in both the X and Y direction.

Adjustable Balance Board for Rehabilitation

Sacha Potvin, Mechanical Engineering Student at the University of Alberta

Introduction

The Glenrose Rehabilitation Research, Innovation, and Technology team (GRITT) [1] at the Glenrose Rehabilitation Hospital (GRH) improves the rehabilitation experience for both staff and patients through the development of new devices and technologies.

Physical therapists (PTs) at the Glenrose approached GRRIT to describe clinical challenges related to the balance boards at the hospital. The Glenrose uses many different styles of balance boards to accommodate for the individual needs of patients. This array of choices increases the time it takes to tailor rehabilitation schedules, poses storage challenges at the hospital, and makes home care visits more difficult as multiple boards must be transported.

A NAIT capstone team began the balance board design featuring adjustable tilt angles (5°-40°) and axes. Prototypes developed by the NAIT team showed promise, which led to the project being adopted by GRRIT's engineering co-op students, namely myself and Allison Probst, whose placement finished in August.

Methods

GRRIT's co-op students improved the adjustable tilt-axis mechanism designed by the NAIT team and designed a resistance mechanism to control how easily the board tilts. This involved modelling stronger and more reliable parts, modifying the materials used, testing design iterations with PTs, and ensuring compliance with Infection Prevention and Control (IPC) standards.

Engineering challenges included design for manufacturing (3D printing & casting), finite element analyses to improve part strength and design, reducing the height of the board, selecting and sourcing materials, ensuring IPC compliance, and designing an effective resistance system.

In October 2020, a final prototype will be fabricated. This prototype will be trialed by PTs for several weeks and final feedback will be provided. Karma Medical Products will then begin work on a commercial version of the board that will become available to the GRH and other sites within Alberta Health Services.

Results

Therapist feedback regarding the current prototypes of the adjustable balance board has been extremely positive. PTs have expressed willingness to use the adjustable board with patients and are satisfied with the level of adjustability available to them. The project has generated enthusiasm among staff to see how it might reduce storage requirements and its potential for gradually increasing difficulty during patient sessions.

Conclusions

The Adjustable Balance Board for Rehabilitation has proven to be a successful undergraduate student project that has demonstrated both clinical and commercial potential. Once implemented, the adjustable board will have the ability to improve the therapist and patient experience at the Glenrose while mitigating the storage challenges currently seen at the site.

References

[1] Alberta Health Services, *Glenrose Rehabilitation Research, Innovation & Technology (GRITT) Hub.* https://www.albertahealthservices.ca/grh/Page14207.aspx

Figures

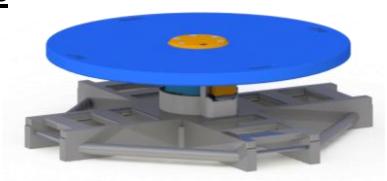

Figure 1: Proposed Balance Board Prototype

Assessing Microelectrode Simulation Techniques

Lisa van de Panne[1], Kazim Haider[2], Thomas Lijnse[3], Colin Dalton[1,3]
Department of Electrical and Computer Engineering, University of Calgary[1]
Mechanical and Manufacturing Engineering, University of Calgary[2]
Biomedical Engineering Graduate Program, University of Calgary[3]

Introduction

Neurological diseases are the leading cause of disability, and the second leading cause of death worldwide [1]. There are many issues with pharmacological solutions, namely severe side effects, high cost, and limited efficacy. Closed- loop therapies that combine the electrical recording and stimulation of neurons have shown promising initial results for neurological diseases such as epilepsy and Parkinson's. Macroelectrodes are traditionally used, yet have limited benefit to patients due to their inability to target specific neuronal ensembles. Microelectrodes are being investigated as a high-potential solution to this issue due to their greater spatial resolution. However, they have the disadvantage of high impedance, which results in poor recording quality and undesirable stimulation parameters. Conductive coatings such as titanium nitride, PEDOT:PSS and iridium oxide prevent this issue, yet are rarely modelled with software due to their varying and complex current mechanisms. Some materials conduct current through electrochemical reactions (Faradaic current), while others through double layer capacitance (capacitive current), both of which are individually difficult to simulate. This work models the relationship between key microelectrode parameters which can be used to improve devices for use in neuromodulation techniques.

Methods

This work uses finite element analysis software (COMSOL, MA, USA) to compare simulations with and without Faradaic and capacitive current. Various conductive coating thicknesses and materials are simulated. Using the electrochemistry modules, the charge species concentration in and around the electrode are analyzed.

Results

The results identify discrepancies between coated microelectrode models with and without commonly used simplifications to electrochemical processes. This work shows the relationship between coating materials, coating thicknesses, and the distribution and magnitude of electrochemical species during stimulation, as seen in Figure 1. Outcomes compare typical simplified models to our adapted models for testing coatings.

Conclusions

The outcomes present a method accurately modelling and evaluating the performance of conductive coatings on microelectrodes. Simulation results more accurately reflect real devices, aiding in optimizing design choices for coated microelectrodes and increasing the safety and efficacy of neuromodulation therapies for improved patient outcomes.

References

[1] Carroll W. M. (2019). The Lancet. https://doi.org/10.1016/S1474-4422(19)30029-8'

Figures

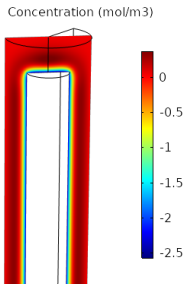

Figure 1: Redox species concentrations (mol/m3) around 3D microelectrodes during Faradaic stimulation of coated microelectrodes